

# Tsunami Coastal Hazard Along the Us East Coast From Coseismic Sources in the açores Convergence Zone and the Caribbean Arc Areas

Stephan Toni Grilli (✉ [grilli@egr.uri.edu](mailto:grilli@egr.uri.edu))

University of Rhode Island <https://orcid.org/0000-0001-8615-4585>

Maryam Mohammadpour

University of Rhode Island

Lauren Schambach

University of Rhode Island

Annette Grilli

University of Rhode Island

---

## Research Article

**Keywords:** Tsunami hazard assessment, Tsunami propagation, earthquakes, Boussinesq wave models

**Posted Date:** April 13th, 2021

**DOI:** <https://doi.org/10.21203/rs.3.rs-404526/v1>

**License:**  This work is licensed under a Creative Commons Attribution 4.0 International License.

[Read Full License](#)

---

**Version of Record:** A version of this preprint was published at Natural Hazards on November 15th, 2021.  
See the published version at <https://doi.org/10.1007/s11069-021-05103-y>.

1 **Tsunami coastal hazard along the US East Coast from**  
2 **coseismic sources in the Açores Convergence Zone and the**  
3 **Caribbean Arc areas**

4 **Stéphan T. Grilli · Maryam Mohammadpour ·**  
5 **Lauren Schambach · Annette R. Grilli**

6  
7 April 2, 2021

8 **Abstract** We model the coastal hazard caused by tsunamis along the US East Coast (USEC)  
9 for far-field coseismic sources originated in the Açores Convergence Zone (ACZ), and the  
10 Puerto Rico Trench (PRT)/Caribbean Arc area. In earlier work, similar modeling was per-  
11 formed for probable maximum tsunamis (PMTs) resulting from coseismic, submarine mass  
12 failure and volcanic collapse sources in the Atlantic Ocean basin, based on which tsunami  
13 inundation maps were developed in high hazard areas of the USEC. Here, in preparation  
14 for a future Probabilistic Tsunami Hazard Analysis (PTHA), we model a collection of 18  
15 coseismic sources with magnitude ranging from M8 to M9 and return periods estimated in  
16 the 100-2,000 year range. Most sources are hypothetical, based on the seismo-tectonic data  
17 known for the considered areas. However, the largest sources from the ACZ, which includes  
18 the region of the Madeira Tore Rise, are parameterized as repeats of the 1755 M8.6-9 (Lis-  
19 bon) earthquake and tsunami using information from many studies published on this event,  
20 which is believed to have occurred east of the MTR. Many other large events have been doc-

---

S.T. Grilli

Department of Ocean Engineering, University of Rhode Island, Narragansett, RI, USA  
E-mail: grilli@uri.edu

M. Mohammadpour

Department of Ocean Engineering, University of Rhode Island, Narragansett, RI, USA  
E-mail: mmohammadpour@uri.edu

L. Schambach

Department of Ocean Engineering, University of Rhode Island, Narragansett, RI, USA  
E-mail: lschambach@uri.edu

A.R. Grilli

Department of Ocean Engineering, University of Rhode Island, Narragansett, RI, USA  
E-mail: annette\_grilli@uri.edu

21 umented to have occurred in this area in the past 2,000 years. There have also been many  
22 large historical coseismic tsunamis in and near the Puerto Rico Trench (PRT) area, triggered  
23 by earthquakes with the largest in the past 225 years having an estimated M8.1 magnitude.  
24 In this area, coseismic sources are parameterized based on information from a 2019 USGS  
25 Powell Center expert, attended by the first author, and a collection of SIFT subfaults for the  
26 area (Gica et al., 2008).

27 For each source, regional tsunami hazard assessment is performed along the USEC at a  
28 coarse 450 m resolution by simulating tsunami propagation to the USEC with FUNWAVE-  
29 TVD (a nonlinear and dispersive (2D) Boussinesq model), in nested grids. Tsunami coastal  
30 hazard is represented by four metrics, computed along the 5 m isobath, which quantify inun-  
31 dation, navigation, structural, and evacuation hazards: (1) maximum surface elevation; (2)  
32 maximum current velocity; (3) maximum momentum force; and (4) tsunami arrival time.  
33 Overall, the first three factors are larger, the larger the source magnitude, and their along-  
34 shore variation shows similar patterns of higher and lower values, due to bathymetric control  
35 from the wide USEC shelf, causing similar wave refraction patterns of focusing/defocusing  
36 for each tsunami. The fourth factor differs mostly between sources from each area (ACZ  
37 and PRT), but less so among sources from the same area; its inverse is used as a measure  
38 of increased hazard associated with short warning/evacuation times. Finally, a new tsunami  
39 intensity index (TII) is computed, that attaches a score to each metric within 5 hazard inten-  
40 sity classes selected for each factor, reflecting low, medium low, medium, high and highest  
41 hazard, and is computed as a weighted average of these scores (weights can be selected to  
42 reinforce the effect of certain metrics). For each source, the TII provides an overall tsunami  
43 hazard intensity along the USEC coast that allows both a comparison among sources and  
44 a quantification of tsunami hazard as a function of the source return period. At the most  
45 impacted areas of the USEC (0.1 percentile), we find that tsunami hazard in the 100-500  
46 year return period range is commensurate with that posed by category 3-5 tropical cyclones,  
47 taking into account the larger current velocities and forces caused by tsunami waves.

48 Based on results of this work, high-resolution inundation PTHA maps will be developed  
49 in the future, similar to the PMT maps, in areas identified to have higher tsunami hazard,  
50 using more levels of nested grids, to achieve a 10-30 m resolution along the coast.

51 **Keywords** Tsunami hazard assessment · Tsunami propagation · earthquakes · Boussinesq  
52 wave models

## 53 1 Introduction

54 Since 2010, under the auspice of the US National Tsunami Hazard Mitigation Program  
 55 (NTHMP; <http://nthmp.tsunami.gov/index.html>), the authors and colleagues  
 56 have performed tsunami modeling work to develop high-resolution tsunami inundation maps  
 57 for the US east coast (USEC), starting with the most critical or vulnerable areas, but with the  
 58 goal to eventually to cover the entire coast. These so-called first generation maps were con-  
 59 structed as envelopes of maximum inundation caused by the most extreme near- and far-field  
 60 tsunami sources in the Atlantic Ocean basin, a.k.a., Probable Maximum Tsunamis (PMTs),  
 61 parameterized based on historical or hypothetical events [48]. In this first generation work,  
 62 no return periods were considered for each source and probabilistic tsunami hazard analyses  
 63 (PTHA) were left out for future work. Extreme tsunamigenic sources causing PMTs that  
 64 can impact the USEC have been identified and modeled in past work [2,3,34,4,32,55,17,  
 65 36,8,13,23,1,19,20,24,25,21,27,57,54,49,37,45]. These sources were divided into three  
 66 groups: 1) coseismic, 2) submarine mass failure (SMF), and 3) volcanic flank collapse. An  
 67 overview of the global coastal hazard resulting from these sources, at the coarse regional  
 68 scale, can be found in Schambach et al. [48].

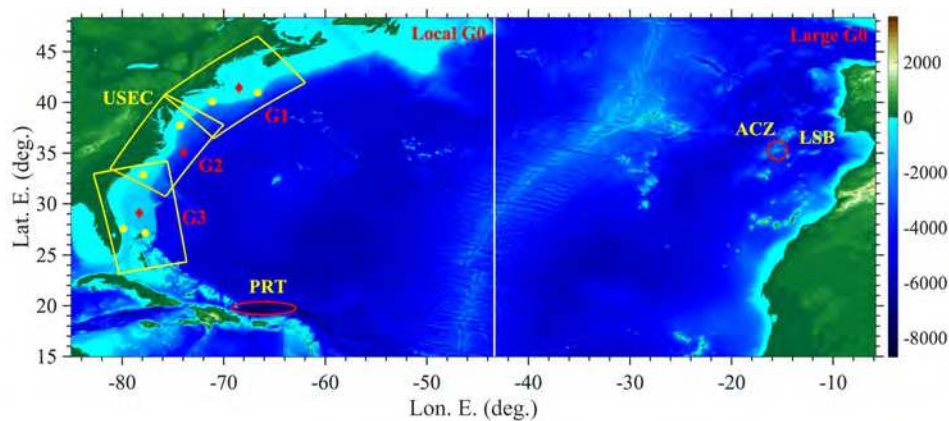


**Fig. 1** Footprint and ETOPO1 bathymetry/topography (color scale in meter shows  $\langle \rangle$  0) of FUNWAVE's 1 arc-min resolution grids in North Atlantic Ocean basin (Local/Large G0), with footprints of 3 regional 450 m nested shore-parallel Cartesian grids (G1, G2, G3; Table 4). Location are marked for the two areas of historical/hypothetical tsunami coseismic sources (red oval) considered, near the Açores Convergence Zone (ACZ), including Lisbon 1755 (LSB), and near and around the Puerto Rico Trench (PRT). The Madeira Torre Rise (MTR) is the shallower ridge located on the north of the ACZ circled area and the Horseshoe Plain is to the East of the ACZ and MTR. Yellow/red symbols within the regional grids mark locations of numerical wave gauge stations where time series of surface elevation are calculated in simulations for validating the one-way grid coupling (Table 2).

69 The present work is part of the initial preparatory steps necessary to perform a complete  
70 PTHA for the USEC and create the next generation of probabilistic NTHMP inundation  
71 maps. PTHA, instead of only considering PMTs, requires combining simulation results for  
72 a collection of tsunami sources of different magnitudes and, hence, return periods for each  
73 type of sources. Here, we only consider far-field coseismic sources in the North Atlantic  
74 Ocean Basin (NAOB), which are the only seismic sources that can be sufficiently tsunami-  
75 genic to cause a significant tsunami hazard along the USEC, where near-field seismicity is  
76 quite moderate [55,57]. Additionally, coseismic sources, as a group, are believed to have  
77 lower return periods than the SMF and volcanic collapse sources in the NAOB [55,57].  
78 Hence, in its lower impact range, this work also provides a first comprehensive assess-  
79 ment of regional scale tsunami hazard for the entire USEC, for a range of return periods  
80 commensurate with those considered in risk analyses for coastal and ocean structures and  
81 infrastructures, for other natural hazard events such as tropical cyclones (e.g., 100 to 500  
82 years).

83 We consider and model coseismic tsunamis generated by a collection of seismic sources  
84 located near and around (Fig. 1): (i) the Açores Convergence Zone (ACZ; Fig. 1 and see Fig.  
85 18 in [57]), including the estimated location of the 1755 Lisbon (LSM) earthquake source,  
86 and (ii) the Puerto Rico Trench (PRT) and Caribbean arc area [33,56,28,21]. Several large  
87 tsunamigenic earthquakes have occurred in these areas. In the ACZ/LSB area, which is lo-  
88 cated along the western segment of the Eurasia-Nubia Plate Boundary, between the Azores  
89 archipelago and the Strait of Gibraltar [7], some of these historical earthquakes have caused  
90 large transoceanic tsunamis, but the Lisbon 1755 earthquake, of estimated magnitude M8.6-  
91 9 [41,8], triggered the largest known historical tsunami. With 5-15 m high waves impacting  
92 the coast, this event caused extensive destruction and tens of thousands of fatalities, in the  
93 near-field in Lisbon and its area (in combination with seismicity and fires), while also reach-  
94 ing the coasts of Morocco, England, Newfoundland, Brazil, and the Antilles. In particular,  
95 after transoceanic propagation, the LSB 1755 tsunami still caused a few meters of inunda-  
96 tion in the eastern Lesser Antilles [2,3,62,4,8,5,57,7]. Large coseismic tsunamis have also  
97 occurred in the PRT and Caribbean arc area [33,55,23,40], which a highly seismic area  
98 running parallel to the north shore of Hispaniola, Puerto Rico, and the north-eastern lesser  
99 Antilles [11,62,55,56,23,28,57] (see Fig. 1 for the observed distribution of earthquakes,  
100 in magnitude and depth). The PRT is the only subduction zone in the NAOB, in which the  
101 North America Plate subducts under the Caribbean Plate with a nearly E-W relative plate  
102 motion (i.e., largely left lateral strike slip; see large black arrows in Fig. 1) and only a small  
103 component of perpendicular convergence (3-6 mm/yr) [11,9]. Nevertheless, in: (i) 1842, a  
104 M8 earthquake in the western segments of the Septentrional fault (SF), which runs nearshore  
105 parallel to the north shore of Hispaniola, triggered a large tsunami that impacted in Haiti [12,

106 16,21]; (ii) 1787, a M8.1 in the PRT triggered a moderate tsunami; and (iii) 1918, a M7.3  
107 earthquakes in the Mona Passage, 15 km off the northwest coast of Puerto Rico, generated a  
108 tsunami that caused 116 fatalities and up to 6 m runup [40,35]. Since the Indian Ocean M9.2  
109 earthquake and tsunami [22,30], we know that highly oblique subduction zones can generate  
110 devastating tsunamis if the earthquake rupture has a large thrust component. Although this is  
111 still controversial, some work has shown that a tsunamigenic M8.7-9 earthquake in the PRT  
112 would cause a devastating tsunami in the near-field and a significantly damaging event in  
113 the far-field, particularly along the upper USEC [32,23]. A recent meeting of experts at the  
114 USGS Powell Center (May 2019) reached the conclusion that such large PRT events were  
115 possible, however, the upper bound magnitude would likely require that fault segments in  
116 part of Hispaniola on the West and the Caribbean arc (up to Guadeloupe) on the East be also  
117 involved (this is further detailed later).

118 In this work, we parameterize and simulate tsunamis generated by coseismic sources  
119 sited in the two selected areas, ranging from magnitude M8 to M9. For the ACZ/LSB area,  
120 we will define sources sited at two different locations and having 2 different orientations  
121 (strike) of 15 and 345 deg. from North, besides different magnitude (M8-M9) and corre-  
122 sponding fault plate areas; this yields ten (10) different coseismic tsunami sources, four of  
123 these being the M9 PMT sources already considered in earlier NTHMP inundation mapping  
124 work [19,48]. Due the large uncertainty of sources in this area, each source is only repre-  
125 sented by a single fault plane. As in earlier work considering PMTs [19], the two selected  
126 orientations are aimed at maximizing tsunami impact on the upper and lower USEC, respec-  
127 tively. Since the LSB/ACZ sources are quite distant from the USEC, tsunami propagation  
128 and refraction over the entire ocean width make details of the sources relatively less impor-  
129 tant [54], hence our earlier work that also considered additional orientations for the sources  
130 showed that these two selected strike angles were sufficient to reflect tsunami hazard along  
131 the USEC. We shall see that a repeat of the LSB M9 1755 event, particularly if it occurred  
132 in the ACZ, West of the Madeira Torre Rise (Fig. 1), a submarine ridge that somewhat di-  
133 verted the transoceanic propagation of the historical event towards the USEC, would have  
134 the potential for causing high tsunami hazard along the entire USEC. In the PRT area, we  
135 only model hypothetical events, following the recommendations on fault plane segmenta-  
136 tion made during the 2019 Powell Center meeting of expert, and consider eight (8) M8-M9  
137 sources that combine 10 to 26 SIFT (Short-term Inundation Forecast for Tsunamis) sub-  
138 faults [17], with for comparison one of these being the M9 PMT source already considered  
139 in earlier NTHMP inundation mapping work [23,20,48].

140 Tsunami simulations are performed for the 18 selected coseismic sources using the fully  
141 nonlinear and dispersive Boussinesq model FUNWAVE-TVD [61,50,31], by one-way cou-  
142 pling in a series of nested spherical or Cartesian coordinate grids. FUNWAVE has been

143 validated for a collection of tsunami benchmarks [53,29], and used in the simulation of  
144 many historical [60,22,30,51,24,31,52,21,26,46,47] and hypothetical [23,1,25,54,49,27,  
145 45] tsunami case studies. As we only aim at assessing the global coastal tsunami hazard  
146 caused by the selected sources along the USEC, we only use two levels of nested grids  
147 (Fig. 1): (i) two large scale spherical grids over the North Atlantic Ocean (or half of it),  
148 with a 1 arc-min resolution, and (ii) 3 smaller regional shore-parallel Cartesian grids over-  
149 lapping along the USEC with a 450 m resolution. For each source, because of the coarse  
150 resolution of the coastal grids, we will assess tsunami hazard using several metrics, com-  
151 puted at a short distance from shore, along the 5 m isobath and will leave inundation and  
152 runup simulations out for future work using higher-resolution grids. Based on similar re-  
153 sults obtained for a collection of PMTs selected in the North Atlantic Ocean [48], as part  
154 of NTHMP work, high-resolution inundation maps were computed for the envelope of all  
155 the PMT results in USEC areas that were deemed at higher hazard or being critical (see  
156 project webpage: <https://www1.udel.edu/kirby/nthmp.html>). To do so, ad-  
157 ditional levels of nested grids were used to achieve a 10-30 m resolution at the coast (see,  
158 for instance, [25]). Note, however, although complex coastal morphologies and highly devel-  
159 oped areas will be under-resolved at a 450 m resolution, from Florida to Massachusetts, the  
160 USEC is essentially made of a series of sandy barrier beach and barrier-island whose coastal  
161 bathymetry is quite simple, and hence coarse grid results should be accurate up to a short  
162 distance from shore and reflection off the coast also be sufficiently accurately represented  
163 in the model. In their simulations of the impact of the 2004 Indian Ocean tsunami along the  
164 coasts of Thailand, using FUNWAVE in a 450 m resolution nested grid, Ioualalen et al. [30]  
165 showed a good agreement between the predicted and observed runups at 58 locations.

166 Based on results of the present work, obtained for eighteen coseismic sources of various  
167 magnitude (and hence return period), and similar results for other types of sources to be  
168 obtained in future work (i.e., for submarine landslides, volcanic flank collapse, and meteo-  
169 tsunamis), PTHA analyses will be conducted and probabilistic inundation maps, similar  
170 to the current first generation NTHMP maps based on PMTs, will be developed in future  
171 work in areas identified to have higher tsunami hazard. To more easily identify these areas,  
172 the coastal tsunami hazard simulated for each source considered here will be quantified  
173 by computing 4 hazard metrics along the 5 m isobath: (1) maximum surface elevation; (2)  
174 maximum current velocity; (3) maximum momentum force; and (4) tsunami arrival time.  
175 Overall, the first three factors are larger, the larger the source magnitude, and the fourth  
176 factor is expected to differ mostly between sources from each area (ACZ and PRT), but less  
177 among sources from the same area.

178 Finally, a tsunami hazard intensity index (TII) will be computed for each source, and  
179 overall, that attaches a score to selected classes of hazard metrics (here 5 classes for each

180 metric), and provides an overall tsunami hazard intensity (or score) at a large number of  
 181 save points along the 5 m isobath. Similar indices have been proposed in earlier work and  
 182 shown to be usefulness in coastal tsunami hazard assessment, to discriminate between low,  
 183 medium and high hazard coastal areas [42, 10].

184 In the following, we first detail recent studies of seismic sources in the NOAB and our  
 185 source selection in the two selected areas (ACZ and PRT). We then present the modeling  
 186 methodology and results in terms of the various tsunami hazard metrics computed along the  
 187 USEC and, based on these, we compute and discuss the TII values for each source.

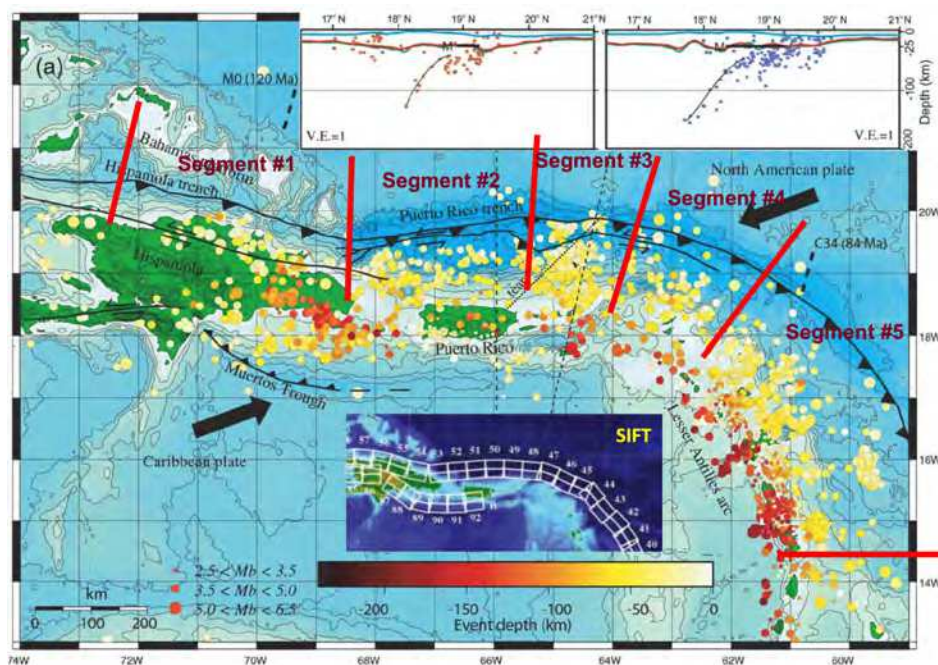


**Fig. 2** Likeliest segmentation in 5 segments of the PRT/Caribbean arc, from west of Hispaniola to Guadeloupe in the eastern part, established at the May 2019 workshop of experts at the USGS Powell Center (see Fig. 1 for location). Insert shows footprints of SIFT subfaults [17] in the considered area (see Table 2 for parameter values). Large black arrows show the nearly E-W relative plate motion of the North America Plate subducting under the Caribbean Plate.

## 2 Recent studies and selection of coseismic sources in the ACZ and PRT areas

### 2.1 ACZ/LSB area

By analyzing the historical sources with information about the occurrence of earthquakes and tsunamis in the region of Cape Saint Vincent-Gulf of Cádiz, Udias [59] reviewed large tsunamigenic earthquakes that occurred SW of Iberia before the 1755 Lisbon earthquake. Separating events that occurred before and after 500 A.D, the author concluded that the 1755 earthquake and tsunami was not an isolated event in SW Iberia and other similarly large events have occurred before the great Lisbon event (e.g., in 241/216 B.C., 881, 1356 and 1531), which is merely the most recent observed event in this category in the ACZ area (Fig. 1). Hence, there is a high likelihood for similarly large events to occur in the future in the ACZ/LSB area.

The exact location and parameters of the 1755 Lisbon earthquake, however, are still unknown and subject to debate. Various studies have placed its magnitude in the M8.6 to 9 range and its most likely location in the Horseshoe Fault to the East of the ACZ and Madeira Torre Rise (MTR; Fig. 1) [41,8]. MTR is an underwater ridge that likely caused westward propagating tsunami waves to be somewhat diverted from aiming at the USEC and, hence, offered some level of protection to the coast. Specifically, Baptista et al. [2,3] performed backward ray tracing and located the 1755 Lisbon source in the area between the Gorringe Bank and the southwestern end of the Portuguese coast. Based on field surveys and tsunami observations, Baptista et al. [4] later proposed a composite source in the Marquês de Pombal and Guadalquivir faults for the event. Barkan et al. [8] identified three potential coseismic tsunami sources for the historical Lisbon event located along three respective major faults, including: (i) the Gorringe Bank Fault (GBF); (ii) The Marques de Pombal Fault (MPF); (iii) The Gulf of Cadiz Fault (GCF). Based on a set of 16 potential tsunami source simulations performed around the areas of these three major faults, Barkan et al. inferred that the most likely source of the 1755 earthquake would have been located in the Horseshoe Plain thrust fault area (NW/SE strike). However, this fault may just be a paleo plate boundary [7]. Omira et al. [44] showed that a source in the Gorringe Bank would have radiated most of its energy towards the NE and Morocco, with a minor impact along the Gulf of Cadiz, and proposed two more potential locations for the source of the 1755 event, the: (iv) Horseshoe Fault and (v) Portimao Bank. They simulated tsunamis from the 5 potential areas and concluded that the most likely location was in Horseshoe Fault.

There have been a few recent tsunamigenic events in the ACZ area, which, although they did not generate large tsunamis, confirmed that large future earthquakes could potentially occur on both sides of the ASZ/MTR area. Hence, in comprehensive tsunami hazard

223 assessment studies, both of these locations must be considered for siting such future events.  
224 Specifically, in 1941 a M8.3 strike-slip earthquake occurred in the Gloria fault, northwest  
225 of the ACZ. A small tsunami was registered at the tide stations of Cascais, Lagos, Portu-  
226 gal, Morocco, Madeira, Azores (and in the UK), with a maximum observed height of 0.45  
227 m (peak to peak) at Casablanca in Morocco. In 1969, a M7.9 earthquake occurred in the  
228 Horseshoe Plain, directly east of the ACZ, which created a small tsunami with a maximum  
229 height of 0.06 m observed on the Portuguese coast in Lagos. And, in 1975, a M7.9 earth-  
230 quake occurred south of the Gloria Fault, within the ACZ and southeast of the MTR [6, 7]  
231 (Fig. 1), which generated a tsunami recorded at a set of coastal tide gauges, with a measured  
232 amplitude of up to 0.3 m in Lagos.

233 As part of earlier NTHMP work, Grilli and Grilli [19] designed extreme M9 PMTs origi-  
234 nated in the ACZ area, as repeats of the Lisbon 1755 event, based on the conclusions of  
235 Barkan et al.'s [8] study. To cover the range of uncertainty on source location and parame-  
236 ters, they modeled twelve sources of M9 magnitude sited at various locations in the ACZ,  
237 with parameters selected based on earlier published work. The strike angle, in particular,  
238 which strongly affects the tsunami directionality, was varied to cause maximum impact on  
239 various sections of the USEC. Among those sources, as expected, they found that maximum  
240 impact on the USEC, with a 1-2 m flow depth at the coast, was created by sources sited  
241 in the MTR, which is the westernmost potential site for the historical earthquake; arrival  
242 time on the USEC was between 8 and 12 h, depending on the location. However, should a  
243 large coseismic source occur west of the MTR, it would cause an even larger impact on the  
244 USEC. Hence for extreme tsunami hazard assessment, such source locations should also be  
245 considered for future events.

Accordingly, in our recent work modeling coastal hazard caused by PMTs along the  
USEC as part of NTHMP [48], we considered four (4) so-called Lisbon (LSB) M9 PMTs,  
sited at locations both west of the MTR (M9.0-MTR1 and M9.0-MTR2) and east of the  
MTR (M9.0-HSP1 and M9.0-HSP2) in the Horseshoe Plain, and with strike angles of 15 or  
345 deg. In combination, these sources should maximize the tsunami impact from extreme  
PMTs originating in this area along the entire USEC. In the absence of more detailed data,  
each source was made of a single fault plane, with parameters based on Barkan et al. [8]  
and Grilli and Grilli [19] listed in Table 1. Here, in addition to these extreme sources, to  
prepare for future PTHA work along the USEC, we design and parameterize 6 additional  
tsunamigenic coseismic sources with 3 smaller magnitudes, M8, 8.3, and 8.7, and for each  
the 2 strike angles, whose parameters are also listed in Table 1. All 10 sources are assumed  
to be similarly shallow to maximize tsunami generation, with a depth below seafloor  $d = 5$   
km at their highest point, and sited at the same location west of the MTR to maximize their  
impact on the USEC, except for M9-HSP1 and M9-HSP2, which are sited in the horseshoe

plain at the likeliest location for the 1755 event. While the M9 sources have a fault plane of length  $L = 317$  km by width  $W = 126$  km [8], the smaller magnitude sources have reduced dimensions derived based on the various references listed before. For each coseismic source, magnitudes  $M$  and fault slip  $S$  are related by the formulas,

$$M_o = \mu LWS \quad (1)$$

where  $M_o$  is the moment magnitude,  $\mu = 40$  GPa the material constant (i.e., Coulomb/shear modulus), and the magnitude is defined as,

$$M = \frac{2}{3} \log M_o - 6 \quad (2)$$

246 For each source, using the fault plane parameters and location listed in Table 1, Okada's  
247 method [43] will be used to compute the initial surface elevation used to initialize the  
248 tsunami propagation model (see details later).

249 Although historical data is limited to accurately attach a return period to each of these  
250 selected ACZ/LSB events, the average recurrence of large LSB 1755 type events appears to  
251 be on the order of 500 years [59] (4-5 medium-large events in 2,000 years). Hence, based  
252 on the corresponding slip and fault area, one could infer that M8, M8.3, and M8.7 events  
253 would have a return periods of 70, 140, and 250 years with a large uncertainty. These return  
254 periods are listed in Table 1 for information, as probabilistic considerations will be addressed  
255 in future PTHA work.

## 256 2.2 PRT and Caribbean Arc area

257 While there have been many studies regarding the seismo-tectonic context and past near-  
258 field tsunamis that have affected the PRT and Caribbean arc area [11,33,62,55,28,57,40]  
259 (see Fig. 1), until the 2019 Powell Center meeting of experts, no comprehensive study had  
260 considered the largest tsunamigenic coseismic sources that could affect the USEC, except  
261 perhaps work performed for the US nuclear regulatory commission [55,56].

262 Hence, when tsunami hazard assessment studies were initialed for the USEC, in the  
263 absence of specific guidance, Knight [32] first proposed a M9.1 PRT source as an extreme  
264 PMT, which encompassed the 600 km long deepest part of the PRT that runs parallels to the  
265 Puerto Rico North shore; this source was parameterized by a single fault plane. Using this  
266 and another similar source with a smaller M8.7 magnitude, Grilli et al. [23] modeled both  
267 the near-field tsunami impact on Puerto Rico and the far-field impact on the USEC. Based  
268 on earlier work [15,40,62], they assumed a predominantly (lateral) strike-slip motion of the  
269 Caribbean plate at 20 mm per year with respect to the North American Plate, in the ENE  
270 direction, at a 10-20 degree angle with respect to the PRT axis. Analyzing the historical

Source (ACZ)	Lat. N. (deg.)	Lon. E. (deg.)	Strike $\theta$ (deg.)	Length $L$ (km)	Width $W$ (km)	Slip $S$ (m)	M	$\sim T_r$ (year)
M8.0-MTR1	36.748	-15.929	15	150	60	2.87	8.0	70
M8.0-MTR2	36.748	-15.929	345	150	60	2.87	8.0	70
M8.3-MTR1	36.748	-15.929	15	175	70	5.95	8.3	140
M8.3-MTR2	36.748	-15.929	345	175	70	5.95	8.3	140
M8.7-MTR1	36.748	-15.929	15	200	80	18.14	8.7	250
M8.7-MTR2	36.748	-15.929	345	200	80	18.14	8.7	250
M9.0-MTR1	36.748	-15.929	15	317	126	20	9.0	500
M9.0-MTR2	36.748	-15.929	345	317	126	20	9.0	500
M9.0-HSP1	36.042	-10.753	15	317	126	20	9.0	500
M9.0-HSP2	36.042	-10.753	345	317	126	20	9.0	500

**Table 1** Parameters of coseismic sources modeled as a single fault plane in the ASZ area (Fig. 1), to be used in Okada's method [43] to define a tsunami source. All sources are shallow, with a depth  $d = 5$  km at the mid-fault highest point, and all fault planes are dipping at  $\delta = 40$  deg., with the rake being  $\gamma = 90$  deg. Estimates of return period  $T_r$  for each events are provided for information only and have a large uncertainty. The M9 sources are Lisbon 1755 proxy sources based on Barkan et al. [8] and Grilli and Grilli [19], while the M8, 8.3 and 8.7 are smaller magnitude sources modeled to prepare for future PTHA along the USEC. Except for M9-HSP1 and M9-HSP2, which are sited in the horseshoe plain at the likeliest location for the 1755 event, all sources are centered at the same location west of the MTR (Fig. 1), to maximize impact on the USEC. Magnitudes and slip are based on a Coulomb modulus  $\mu = 40$  GPa. Fig. 4 shows the initial elevation computed for the 4 largest sources; other sources have similar patterns of elevations and depression, but smaller amplitude initial surface elevations.

271 earthquakes and the tsunamigenic events among those, they noted that 12 earthquakes of  
 272 at least a M7 magnitude had occurred in and near the PRT area in the past 500 years [14].  
 273 Among those, two had a M8.1 magnitude, and three generated a tsunami with a 5-7 m on  
 274 Puerto Rico. Combining these observations with the plate convergence rates, they estimated  
 275 that a M7.5-8.1 event in the PRT would have an 80 year return period, a M8.7 event at least  
 276 a 200 year return period, and a M9 event at least a 600 year return period. In view of more  
 277 recent work on the segmentation and fault locking in the area (see below), it is likely that  
 278 these return periods were under-estimated.

279 Simulating Knight's extreme M9 event, Grilli et al. [23] showed that the generated  
 280 tsunami could cause up to 2-3 m runup along the USEC and arrival times would be be-  
 281 tween 2.5 and 6 h, depending on the location. In our initial NTHMP work, in light of new  
 282 data provided on subfault parameters in the PRT/Caribbean arc area as part of NOAA's SIFT  
 283 dataset [17], Grilli et al. [20] designed and modeled a different M9 PMT source, which ap-  
 284 proximately covered the same area of the PRT as Knight's [32] source, i.e., 600 km long  
 285 by 150 km wide, but was parameterized as 6 by 2 (i.e., 12) individual SIFT subfaults, each  
 286 100 long by 50 km wide (in the oblique fault plane), which better represented the convex

287 geometry of the PRT. Although this was an extreme scenario, particularly for Puerto Rico,  
288 their work on the 2004 Indian Ocean M9.2 earthquake [22,30] and devastating tsunami had  
289 convinced these authors, as others [55,56], that a large megathrust event could occur in the  
290 PRT because of the similarity between the geometry (both trenches are arched) and plate  
291 dynamics of the Puerto Rico and Sumatra-Andaman trenches. This was also supported by  
292 their work on the Tohoku 2011 M9 earthquake and tsunami, that occurred in the similar size  
293 Japan trench [24,52]. Most recently, simulations of tsunami hazard caused by PMTs on the  
294 USEC were performed at higher resolution using as one of the sources that of Grilli et al.  
295 [20], which confirmed the range of runup and arrival time predicted earlier [48].

296 In the present work, we needed to design and model a collection of hypothetical, but re-  
297 alistic, coseismic tsunami sources of various magnitude (and return periods) in the complex  
298 PRT/Caribbean arc area, that would significantly impact the USEC. As indicated before, a  
299 meeting of experts was organized in May 2019 at the USGS Powell Center, attended by the  
300 lead author, whose agenda was devoted in large part to establishing a so-called logic tree  
301 for coseismic sources in the PRT and Caribbean arc area that could cause tsunamis affect-  
302 ing the USEC. Such a tree visualizes the various sources and their parameter range, while  
303 attaching a probability to each branch off the tree. The workshop approach was based on the  
304 Delphi method, which is a process used to arrive at a group opinion by surveying the experts  
305 attending the venue. Through several rounds of questionnaires, the responses provided by  
306 the experts on various source parameters were transformed into tables of probabilities for  
307 classes of parameter values.

308 The consensus of the experts at the meeting was that a first step was, by considering  
309 existing seismo-tectonic knowledge in the area, to establish a segmentation of the entire  
310 Caribbean arc into realistic segments, most likely to fail either separately or together in clus-  
311 ters, and to estimate their parameters. Sources of various magnitude could then be designed  
312 by combining those segments. Additionally, in the PRT and on both sides of it, there was  
313 large uncertainty on the level of locking and the magnitude of the fault-normal convergence  
314 rate that would most contribute to causing large tsunamigenic earthquakes [9], whose range  
315 needed to be estimated. Figure 2 shows the likeliest segmentation established during the  
316 meeting, which is composed of 5 segments, of the faults encompassing subduction zones in  
317 the Hispaniola trench on the west (Segment #1), the PRT in the middle (Segments #2,3), and  
318 in the northern Lesser Antilles arc (Segments #4,5). Each of these segments approximately  
319 overlaps with subfaults defined in the SIFT dataset [17] (see insert in Fig. 2). For each SIFT  
320 subfault, of dimension  $L = 100$  by  $W = 50$  km in the trench-parallel and trench-normal  
321 directions, respectively, the dataset provides the strike and dip angles, with the rake angle  
322 assumed as  $\gamma = 90$  deg. in all cases (to maximize the seafloor deformation), and the lat-lon  
323 coordinates of the fault centroid and depth  $d$  of the fault highest point. Table 2 provides

Segment #	SIFT subfault	Lon. E. (deg.)	Lat. N. (deg.)	Depth $d$ (km)	Strike $\theta$ (deg.)	Dip $\delta$ (deg.)
1	atsza57	-72.3535	19.4838	22.10	94.20	20.00
1	atszb57	-72.3206	19.9047	5.00	94.20	20.00
1	atsza56	-71.5368	19.3853	22.10	102.64	20.00
1	atszb56	-71.4386	19.7971	5.00	102.64	20.00
1	atsza55	-70.7045	19.1376	22.10	108.19	20.00
1	atszb55	-70.5647	19.5386	5.00	108.19	20.00
1	atsza54	-69.6740	18.8841	22.10	101.54	20.00
1	atszb54	-69.5846	19.2976	5.00	101.54	20.00
2	atsza53	-68.4547	18.7853	22.10	83.64	20.00
2	atszb53	-68.5042	19.2048	5.00	83.64	20.00
2	atsza52	-67.5412	18.8738	22.10	85.87	20.00
2	atszb52	-67.5734	19.2948	5.00	85.87	20.00
2	atsza51	-66.5742	18.9484	22.10	84.98	20.00
2	atszb51	-66.6133	19.3688	5.00	84.98	20.00
2	atsza50	-65.6921	18.9848	22.10	89.59	20.00
2	atszb50	-65.6953	19.4069	5.00	89.59	20.00
3	atsza49	-64.8153	18.9650	22.10	94.34	20.00
3	atszb49	-64.7814	19.3859	5.00	94.34	20.00
3	atsza48	-63.8800	18.8870	22.10	95.37	20.00
3	atszb48	-63.8382	19.3072	5.00	95.37	20.00
4	atsza47	-63.1649	18.7844	22.10	110.46	20.00
4	atszb47	-63.0087	19.1798	5.00	110.46	20.00
4	atsza46	-62.4217	18.4149	17.94	117.86	15.00
4	atszb46	-62.2075	18.7985	5.00	117.86	15.00
4	atsza45	-61.5491	18.0566	17.94	112.84	15.00
4	atszb45	-61.3716	18.4564	5.00	112.84	15.00
5	atsza44	-61.1559	17.8560	17.94	141.07	15.00
5	atszb44	-60.8008	18.1286	5.00	141.07	15.00
5	atsza43	-60.5996	17.0903	17.94	138.71	15.00
5	atszb43	-60.2580	17.3766	5.00	138.71	15.00
5	atsza42	-59.9029	16.4535	17.94	136.99	15.00
5	atszb42	-59.5716	16.7494	5.00	136.99	15.00

**Table 2** SIFT subfault and their parameters from Gica et al. [17], for each segment selected for defining coseismic tsunami sources in the PRT/Caribbean arc area (Figs. 1 and 1) using the Okada [43] method. In addition, each subfault has a (horizontal) length  $L = 100$  km, width  $W = 50$  km, and rake  $\gamma = 90$  deg. The material constant (shear modulus) used is  $\mu = 40$  GPa, as recommended in [17].

324 these parameters for all the SIFT subfaults overlapping with Segments #1 to 5 from Fig. 2,  
325 with the subfault locations defined in the figure inset.

326 The second step considered by the experts was defining the likeliest grouping of indi-  
327 vidual segments that would fail together in a single event, thus creating sources of larger

328 magnitude, as well as the associated magnitude for each such event and their likelihood  
329 (i.e., probability). Although the final proceedings of the workshop are still pending, based  
330 on draft material from the workshop, Table 2.2 lists 7 new sources in the PRT/Caribbean  
331 arc area, with magnitudes M8.3, M8.7, and M9.0, that regroup 2 to 4 segments from Fig. 2;  
332 an additional eighth source M9.0-PRT3 is the extreme PMT source used in earlier work to  
333 date [20,48]. Based on the SIFT subfault dimensions and their number used for each source  
334 listed in Table 3, an associated average slip  $S$  was computed for using Eqs. 1 and 2, assum-  
335 ing  $\mu = 40$  GPa as in the SIFT study. For each source, using the fault plane parameters and  
336 location listed in Table 3, Okada's method [43] will be used to compute the initial surface  
337 elevation used to initialize the tsunami propagation model (see details later).

338 If the maximum convergence rate of  $\sim 20$  mm/y (i.e., 1 m of slip in 50 years) in the area  
339 contributed to the listed slip values, the return period for each source would be  $\sim 75$ , 185,  
340 and 355 years, respectively. However, the relative subduction between the Caribbean and  
341 North-American plates is highly oblique (10-20 deg.) on the western side of the considered  
342 area and less so in the lesser Antilles (Fig. 2). Accumulated fault slip must be multiplied by  
343 the sine of the convergence angle; hence, assuming an average of 20 deg. for the entire area  
344 yields a factor of one-third or so and approximate return periods on the order of 250, 550,  
345 and 1,000 years for each source magnitude, respectively, which is consistent with estimates  
346 made during the Powell workshop; applying the same considerations to the M9.0-PRT3  
347 source, we find an approximate return period of years of 2,000 years (i.e., about 3 times  
348 the earlier estimate that did not consider the oblique subduction [23]). The estimated return  
349 periods are listed for each source in Table 2.2, however, detailed probabilistic considerations  
350 will be left out for future PTHA work.

### 351 **3 Methodology**

#### 352 **3.1 Tsunami propagation model**

353 For each of the selected coseismic sources, tsunami propagation to the USEC is modeled us-  
354 ing the nonlinear and dispersive two-dimensional (2D) Boussinesq long wave model (BM)  
355 FUNWAVE [61], in a series of nested grids of increasing resolution, by a one-way coupling  
356 method. We use FUNWAVE-TVD V.3, the newer implementation of FUNWAVE, which is  
357 fully nonlinear in Cartesian grids [50] and weakly nonlinear in spherical grids [31]. The  
358 model was efficiently parallelized for use on a shared memory cluster, which allows us-  
359 ing large grids. FUNWAVE and then FUNWAVE-TVD are open source codes that have  
360 been widely used to simulate tsunami case studies [22,30,51,23,1,52,24,31,54,25,21,27,  
361 26,46,47]. As discussed in the introduction, since 2010 as part of the NTHMP work (see,

Source (PRT)	Segments number	Nb. SIFT	Slip $S$ (m)	M	$\sim T_r$ (year)
M8.3-PRT1	#2 - 3	12	1.3	8.3	250
M8.3-PRT2	#3 - 4	10	1.6	8.3	250
M8.3-PRT3	#4 - 5	12	1.3	8.3	250
M8.7-PRT1	#2 - 4	18	3.5	8.7	550
M8.7-PRT2	#3 - 5	16	3.9	8.7	550
M9.0-PRT1	#1 - 4	26	6.8	9.0	1,000
M9.0-PRT2	#2 - 5	24	7.4	9.0	1,000
M9.0-PRT3	#2 - 3	12	14.8	9.0	2,000

**Table 3** Definition in terms of segmentation established at the USGS 2019 Powell Center workshop, of coseismic sources modeled as multiple SIFT subfault planes in the PRT/Caribbean arc area (Fig. 1), to be used in Okada's method [43] to define a tsunami source (Fig. 1). Magnitude and slip (based on a Coulomb modulus  $\mu = 40$  GPa) are given in the table and other parameters of SIFT sources used in each segment are given in Table 2. Estimates of return period  $T_r$  for each events are provided for information only and have a large uncertainty. The collection of sources is modeled to prepare for future PTHA along the USEC. Fig. 5 shows the initial surface elevations computed for these sources. Note that source M9.0-PRT3 is the extreme PMT source used in earlier work [23,20,48].

362 <http://chinacat.coastal.udel.edu/nthmp.html>; e.g., [1, 19, 20, 25, 27, 54, 45]), the authors have  
 363 used FUNWAVE and related methodology to simulate PMTs and compute tsunami inun-  
 364 dation maps along the USEC. The same model and approach were also used to perform  
 365 several other tsunami hazard assessment studies of coastal nuclear power plants in the U.S.  
 366 Both spherical and Cartesian versions of FUNWAVE-TVD were validated through bench-  
 367 marking and approved for NTHMP work [53, 29, 38].

368 As they include frequency dispersion effects, BMs simulate more complete physics than  
 369 models based on Nonlinear Shallow Water Equations (NSWE), which until recently were  
 370 traditionally used to simulate coseismic tsunami propagation. Dispersive models are neces-  
 371 sary to accurately simulate landslide tsunamis [18, 45], which are typically made of shorter  
 372 and hence more dispersive waves than coseismic tsunamis [60]. However, dispersion is also  
 373 important for modeling the propagation of coseismic tsunamis over long distances [31], and  
 374 their coastal impact when using high resolution grids, since undular bores can be gener-  
 375 ated nearshore near the crest of incident long waves [39, 45]. The importance of dispersion  
 376 for modeling tsunami propagation was confirmed by running FUNWAVE in both BM and  
 377 NSWE modes, e.g., for the 1998 Papua New Guinea landslide tsunami [51], for the 2004  
 378 Indian Ocean [30] and for the 2011 Tohoku coseismic tsunamis [31], and for the 2018 Palu  
 379 tsunami [47].

380 Along the shore, FUNWAVE has an accurate moving shoreline algorithm that identifies  
 381 wet and dry grid cells, allowing to dynamically compute tsunami inundation and runup. Bot-

Grid/ Type	Lat. N. (SW/CT) (deg.)	Lon. E. (SW/CT) (deg.)	Lat. N. (NE) (deg.)	Lon. E. (NE) (deg.)	Res.	$N_x$	$N_y$	Angle (clock.) (deg.)
Large G0/S	15	-85	48.32	-5.85	1 min	4,750	2,000	0
Local G0/S	15	-85	48.32	-43.35	1 min	2,500	2,000	0
G1/C	41.500	-69.00 )			450 m	2,200	1,416	39.66
G2/C	35.750	-75.75			450 m	2,100	1,332	57.90
G3/C	28.705	-78.05			450 m	2,472	1,536	101.2

**Table 4** Parameters of model grids used in FUNWAVE to compute the propagation of far-field coseismic sources from the ACZ/LSB and PRT areas (Figs. 1, 3). “Res.” refers to the resolution of Spherical (S) or Cartesian (C) type grids and  $N_x$  and  $N_y$  indicate the number of grid cells in each direction. Letters in parenthesis indicate whether coordinates are for: (SW) Southwest corner, (NW) corner, or (CT) center of grid.

Save Point	Lat. N. (deg.)	Lon. E. (deg.)
P-G1	41.430	-68.480
P-G2	35.050	-73.950
P-G3	29.070	-78.300
P1	40.954	-66.632
P2	40.084	-71.143
P3	37.709	-74.309
P4	32.842	-77.910
P5	27.579	-79.888
P6	27.183	-77.711

**Table 5** Nested grid save points P-G1 to G3 (red diamonds in Fig. 1) used to compare time series of surface elevation with those computed in grid G0. Numerical wave gauges P1 to P6 where additional time series are computed in grids G1, G2 and G3 (yellow dots symbols in Fig. 1); P1 to P5 are located along the 200 m isobath (from north to south) and P6 is in 1,000 m depth (southernmost point north of the Great Bahama Banks off of Florida).

382 tom friction is modeled by a quadratic law, with a constant friction coefficient; in the absence  
383 of more specific data, we used the standard value  $C_d = 0.0025$ , which corresponds to coarse  
384 sand and is conservative as far as tsunami runup and inundation. Earlier work indicates that  
385 tsunami propagation results are not very sensitive to the friction coefficient values in deeper  
386 water, but that they are affected in shallower water; in particular, the modeled wave height  
387 decay over a wide shallow shelf strongly depends on bottom friction [54]. Finally, dissipa-  
388 tion from breaking waves is modeled using a front tracking (TVD) algorithm and switching  
389 to NSWEs in grid cells where breaking is detected (based on a breaking criterion). Ear-  
390 lier work has shown that numerical dissipation in NSW models closely approximates the  
391 physical dissipation in breaking waves [50].

392 Simulations of tsunami propagation and coastal impact are performed in nested grids  
393 (Figs. 1, 3), by one-way coupling. In this method, time series of surface elevations and  
394 depth-averaged currents are computed at a large number of stations/numerical wave gages,  
395 defined in a coarser grid, along the boundary of the finer grid used in the next level of  
396 nesting. Computations are performed in the coarser grid and then are restarted in the finer  
397 grid, using the station time series as boundary conditions. As the latter include both incident  
398 and reflected waves computed in the coarser grid, this method closely approximates open  
399 boundary conditions. It was found that a nesting ratio with a factor 3-4 reduction in mesh  
400 size allowed achieving good accuracy in tsunami simulations. Finally, to prevent reflection  
401 in the first grid level, sponge layers are used along all the offshore boundaries (see, e.g., [52,  
402 45,46,47] for a few examples).

403 For each coseismic source, simulations are initiated in a 1 arc-min (about 1800 m) res-  
404 olution grid, in which the tsunami source elevation is specified as an initial condition, with  
405 a zero velocity as is standard in such simulations). For the ACZ/LSB sources, this is the  
406 ocean basin scale spherical grid “Large G0”, which covers the footprint of Fig. 1, and for  
407 the PRT/Caribbean arc sources, this is the smaller “Local G0” (Figs. 1; Table 4). In both  
408 grids, 200 km wide sponge layers are specified along the west, south and north offshore  
409 boundaries, and 400 km wide on the east boundary, to eliminate reflection. To compute the  
410 tsunami impact along the USEC, simulations are continued in 3 regional, angled, Cartesian  
411 nested grids of 450 m resolution, G1, G2, and G3 (Figs. 1, 3; Table 4).

412 For each grid level, bathymetry and topography are interpolated from the most accurate  
413 data available, of accuracy commensurate with the grid resolution. In deeper water, we use  
414 NOAA’s 1 arc-min ETOPO-1 data (Fig. 1); in shallower water and on continental shelves,  
415 we use NOAA’s NGDC 3” (about 90 m) Coastal Relief Model data (Fig. 3). Save points  
416 are defined in each grid (P-G1, P-G2, and P-G3 in Table 3.1; Fig. 1), where time series of  
417 surface elevations and currents are computed in order to verify that results in nested grids  
418 (G1, G2, G3) are consistent with those in the coarser parent grid (G0). Additional numerical  
419 wave gauges (P1 to P6 in Table 3.1; Fig. 1) are also specified to visualize details of incident  
420 tsunami wave trains (i.e., number of waves, wave amplitudes and periods), with P1 to P5  
421 being located along the 200 m isobath, at the continental shelf edge, and P6 is in 1,000 m  
422 depth (southernmost point north of the Great Bahama Banks off of Florida).

423 Note that transformations from (Lon.-Lat.) to Cartesian  $(x, y)$  coordinates and back are  
424 performed using Matlab’s mapping toolbox, using a transverse Mercator projection (UTM),  
425 with an origin at each grid’s centroid.

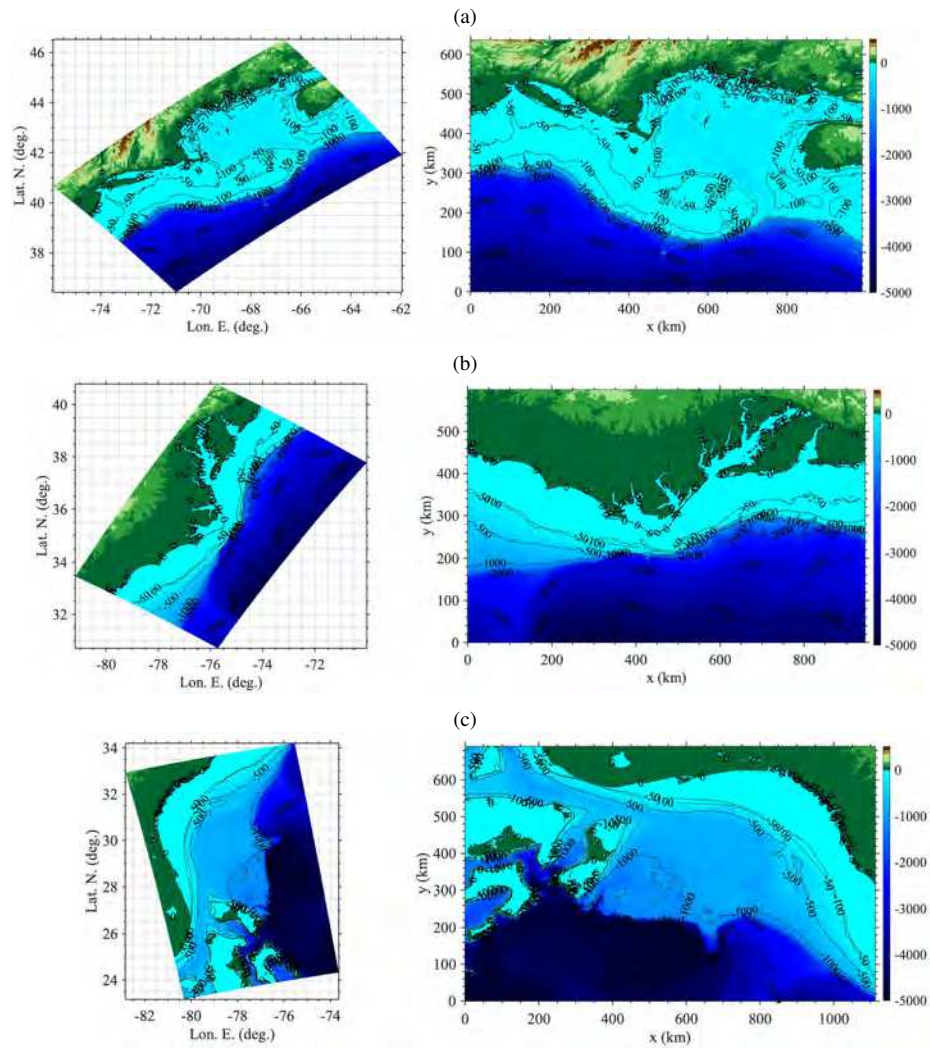


**Fig. 3** Footprints of 450 m resolution grids used in FUNWAVE, in spherical (left) and Cartesian (right) coordinates (Table 4, Fig. 1): (a) G1, (b) G2, (c) G3; color scales and contours are bathymetry/topography in meter.

### 426 3.2 Coseismic tsunami source parameters and generation

427 Following the standard approach for large coseismic tsunamis, the initial tsunami surface el-  
 428 evation (with zero velocity) of each source is assumed to be equal to the maximum seafloor  
 429 deformation caused by the earthquake; this is acceptable since water is nearly incompress-  
 430 ible and raise times are usually small. The seafloor deformation is computed using Okada's  
 431 [43] method, which solves linear three-dimensional (3D) elasticity problems in a series of

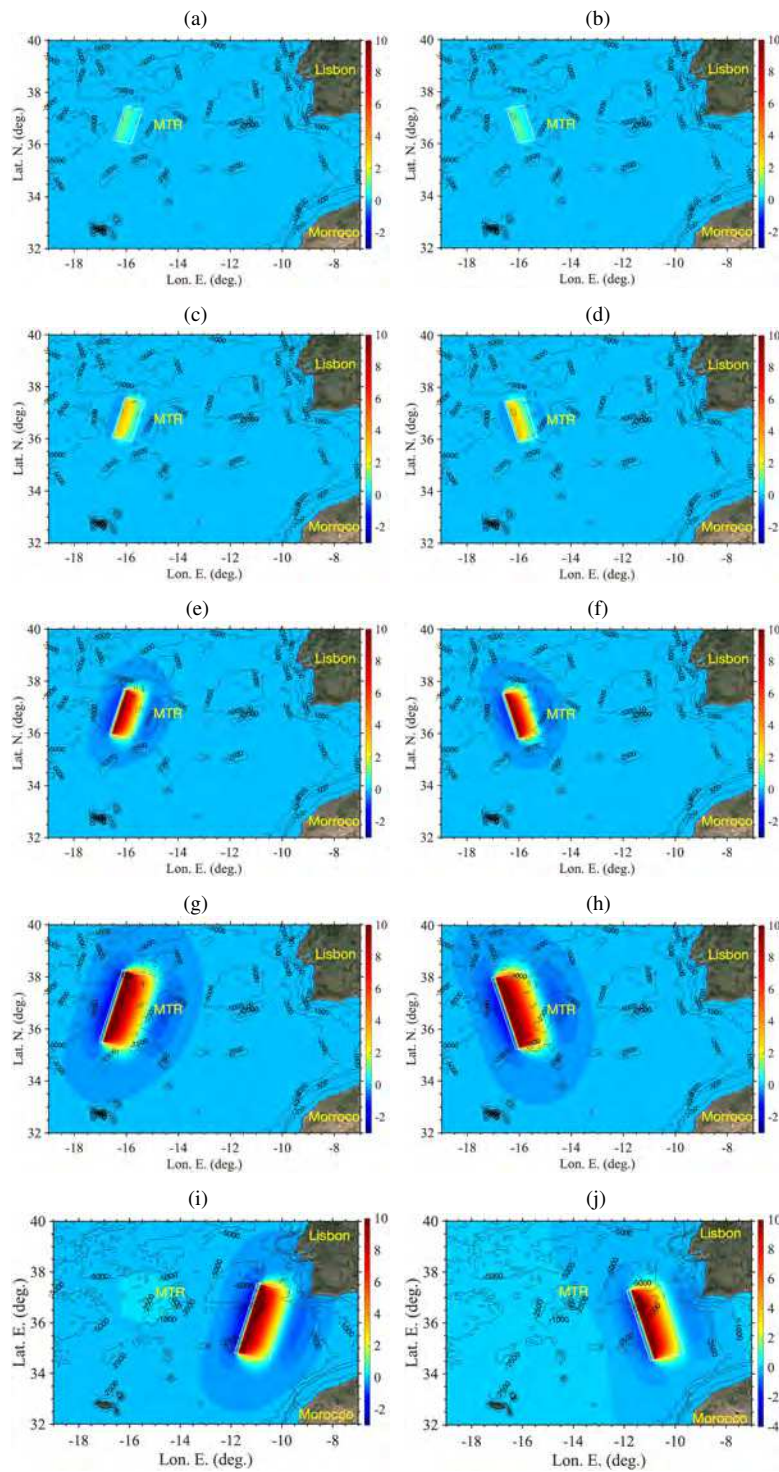


**Fig. 4** Initial surface elevations computed with Okada's [43] method (color scale in meter) for coseismic tsunami sources in the ACZ/LSB area (Fig. 1; Table 1): (a) M8.0-MTR1; (b) M8.0-MTR2; (c) M8.3-MTR1; (d) M8.3-MTR2; (e) M8.7-MTR1; (f) M8.7-MTR2; (g) M9.0-MTR1; (h) M9.0-MTR2; (i) M9.0-HSP1; (j) M9.0-HSP2. Each source has a single fault plane with footprint marked by white solid lines. Note, the M9.0 sources represent Lisbon 1755 proxies, located in either the ACZ, west of the MTR ("MTR"), or Horseshoe Plain ("HSP") areas (Fig. 1.)

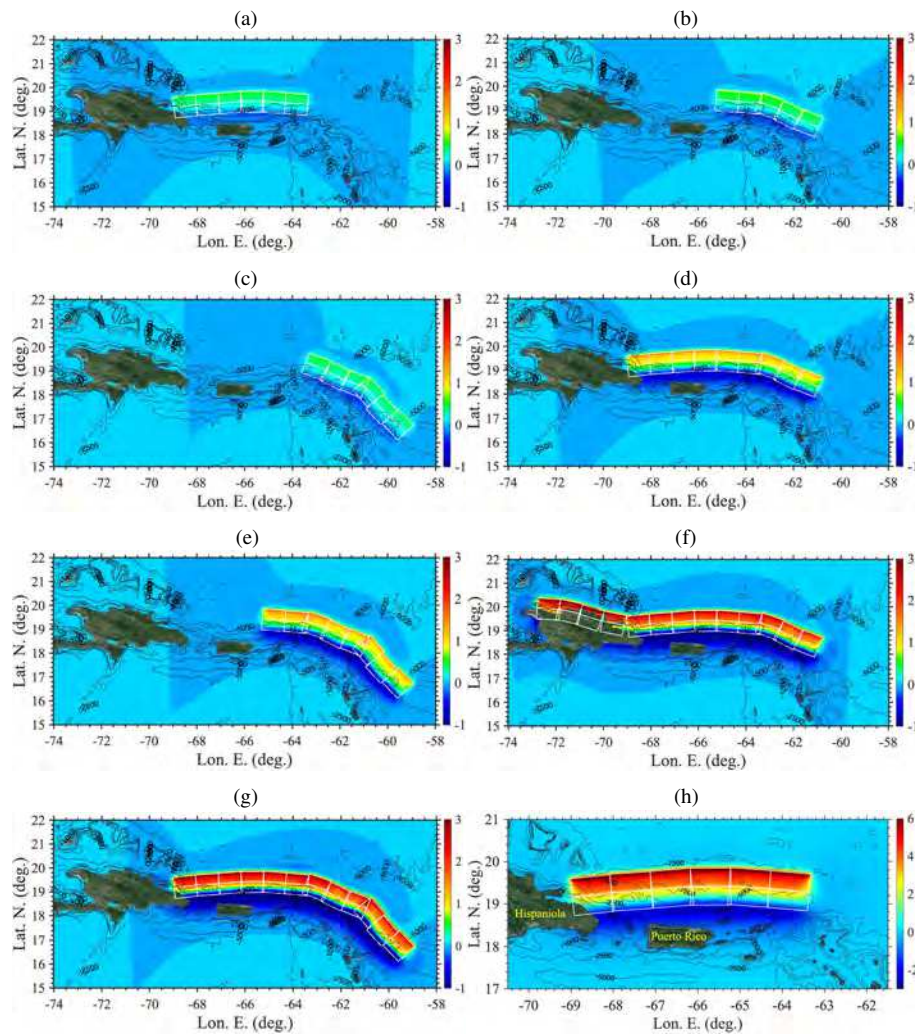


**Fig. 5** Initial surface elevations computed with Okada's [43] method for the modeled PRT/Caribbean arc tsunami sources (Fig. 1; Table 3): (a) M8.3-PRT1; (b) M8.3-PRT2; (c) M8.3-PRT3; (d) M8.7-PRT1; (e) M8.7-PRT2; (f) M8.7-PRT3; (g) M9.0-PRT2; and (h) M9.0-PRT3. All source parameters are given Tables 2 and 3. Color scale (in meter), with same scale is used in plots (b-h), for comparison.

432 homogeneous half-spaces, corresponding to the source subfaults, each with a dislocation  
 433 specified over an oblique plane. The problems are expressed as a set of Boundary Integral  
 434 Equations, which are solved over a specific Cartesian grid encompassing the subfaults (here  
 435 with a 1 km resolution); due to the linearity of the equations, the total seafloor deformation  
 436 is expressed as the sum of that caused by each subfault. The required geometric parameters  
 437 of each subfault are the fault plane horizontal area (width  $W$  and length  $L$ ), the depth  $d_o$  at

438 the source centroid, the centroid location  $(x_o, y_o)$  (Lon.-Lat.), and 3 angles orientating the  
439 fault plane (dip  $\delta$ , rake  $\gamma$ , strike  $\theta$ ); with these definitions,  $d_o = d + (W/2) \sin \delta$ , where  $d$   
440 is the highest point on the subfault plane. In addition the model needs the Coulomb modu-  
441 lus ( $\mu$ ) of the medium (10-60 GPa, for shallow ruptures in soft/poorly consolidated marine  
442 sediment to deep ruptures in basalt);  $\mu = 40$  GPa is used here in all cases [17].

443 Parameters of selected coseismic sources modeled in the ACZ/LSB and the PRT/Caribbean  
444 arc areas are given in Table 1, and 2-3, respectively. Fig. 4 shows the initial surface elevations  
445 computed for the ACZ/LSB sources (Table 1). The four largest M9 sources cause a nearly  
446 12 m maximum elevation and a 4 m maximum depression. The other, smaller magnitude,  
447 ASZ sources plotted in Figs. 4e-j have similar patterns of uplift and subsidence, but smaller  
448 surface elevations distributed over gradually smaller areas. Fig. 5 shows the initial surface  
449 elevations computed for the PRT/Caribbean arc sources (Tables Tables 2 and 3). The new  
450 M9 sources in Figs. 5f,g (PRT1 and PRT2) have an over 4 m maximum elevation and 2 m  
451 maximum depression, about half the maximum value of the earlier M9.0-PRT3 PMT source  
452 (Fig. 5h). The other, smaller magnitude, sources plotted in Figs. 5a-e have similar patterns of  
453 uplift and subsidence, but gradually smaller surface elevations as their magnitude decreases.

### 454 3.3 Tsunami propagation and coastal impact

455 For each coseismic source, tsunami propagation is first simulated with FUNWAVE in grids  
456 Large G0 or Local G0 for 24 h, respectively, depending on the source location. Simulations  
457 are then restarted in the three finer nested grids (G1, G2 and G3), also up to the full duration,  
458 but for more efficiency starting from the time of first arrival of the tsunami along each nested  
459 grid boundary.

460 Figure 6 shows an example of surface elevations computed for the Lisbon 1755 proxy  
461 source M9-HSP1 (Fig. 4i; Table 1) at times  $t = 1$  to 11h, with the figures at later times  
462 focusing on the impact computed in grid G3 off of Florida. The snapshots illustrate how  
463 waves radiate away from the source, diffracting around islands and refracting as a function of  
464 the bathymetry. In particular, Figs. 6e-h illustrate how the continental slope and shelf cause  
465 intense refraction of incident tsunami waves, which increasingly bend to become nearly  
466 parallel to the isobaths as they gradually slow down. This phenomenon affects all ACZ/LSB  
467 sources in the same manner and causes them to focus or defocus their energy on identical  
468 coastal areas depending on the shelf bathymetry. As a result of dispersion, nearshore tsunami  
469 waves are made of at least three major crests and troughs (Fig. 6h). Despite the 15 deg.  
470 strike angle, the largest tsunami waves originated from this source are aimed at Florida.  
471 This is confirmed in Fig. 7, which shows the envelopes of maximum surface elevations  
472 computed for the M9-HSP1 and M9-HSP2 sources. While both sources direct their major

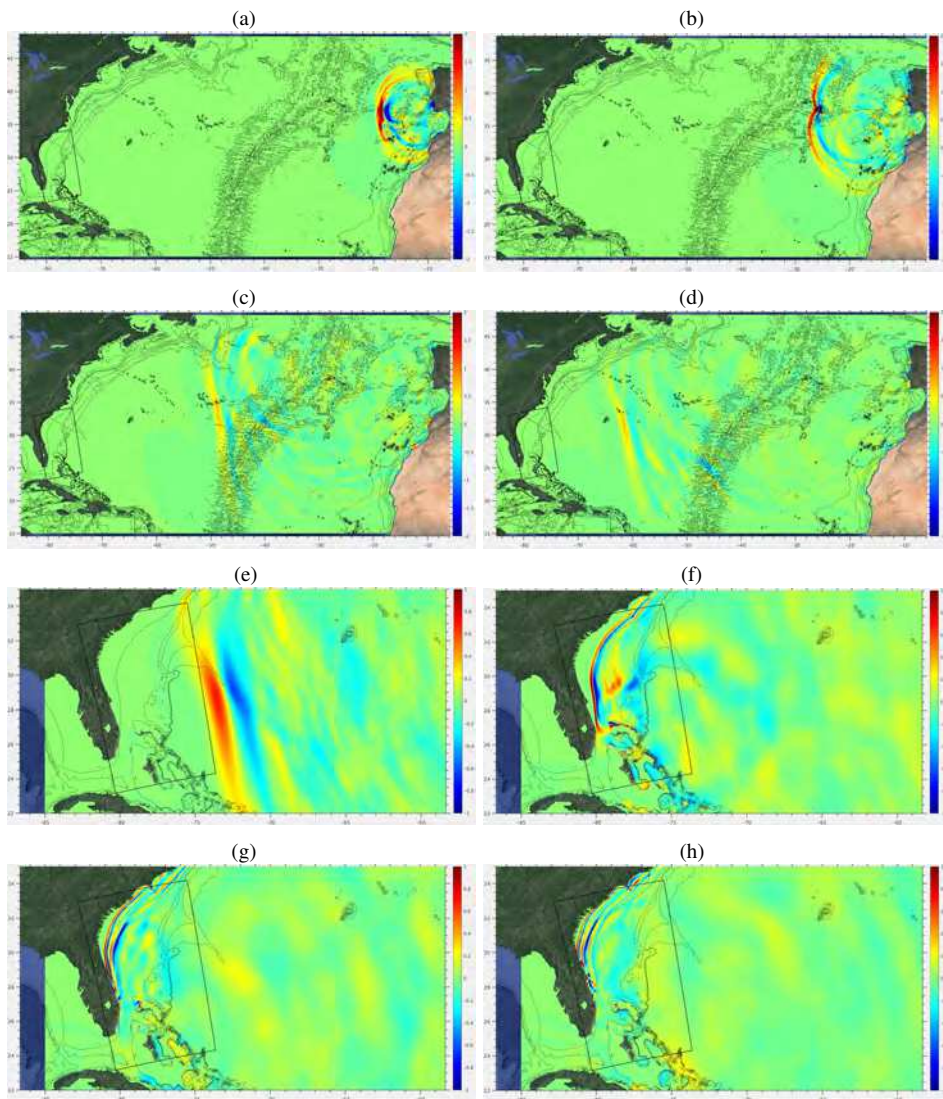


**Fig. 6** Snapshots of surface elevations (color scale in meter) computed for the Lisbon 1755 proxy source M9-HSP1 (Fig. 4i; Table 1), at  $t =$  (a) 1, (b) 2, (c) 5, (d) 6.5, (e) 8, (f) 9.5, (g) 10.5, and (h) 11 h. Some isobaths are plotted for reference, but without labels to simplify the figures. Higher resolutions results are used wherever available.

473 wave energy southwestward, as expected from their orientation, the first source, with a 15  
 474 deg. strike angle, causes a relatively larger tsunami impact along the upper USEC than the  
 475 second source, with a 345 deg. strike angle, which causes a larger impact along the lower  
 476 USEC and the Caribbean Islands. This will be further detailed later. A movies showing

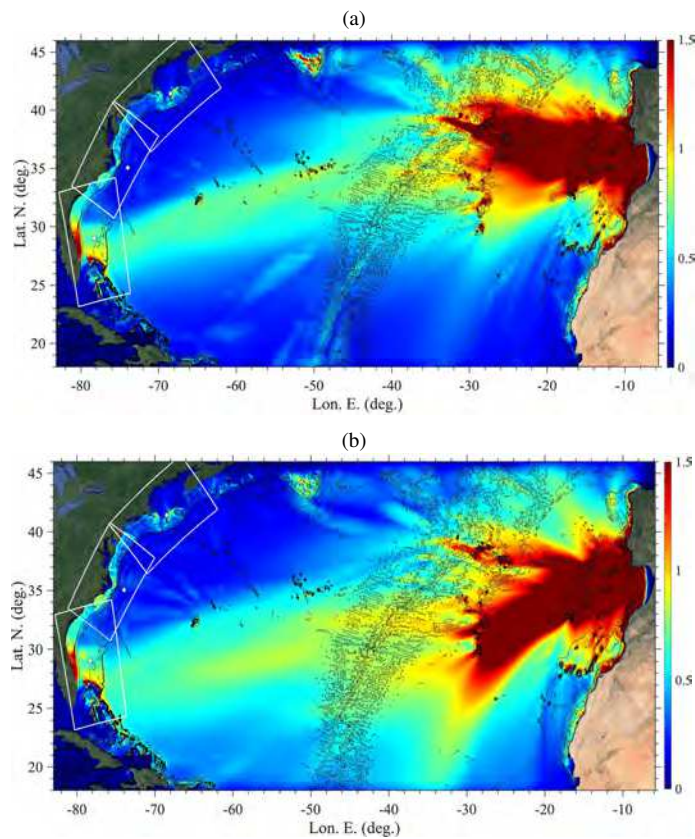


**Fig. 7** Envelope of maximum surface elevation computed with FUNWAVE during 24h of simulations in grid Large G0 (Table 4; Fig. 1) for the: (a) M9-HSP1, and (b) M9-HSP2, historical Lisbon 1755 coseismic sources (with parameters listed in Table 1 and initial surface elevations in Figs. 4i,j). Color scales are surface elevation in meter.

477 animated results of the M9-HSP1 source simulation is provided as supplementary material  
478 (HSP1.mp4).

479 Similarly, Fig. 8 shows snapshots of surface elevations for the M9.0-PRT3 source (Fig.  
480 5h; Table 3), at  $t = 0.5$  to 5 h, with the figures at later times focusing on grid G1, off of  
481 the upper USEC (centered in New England) where, due to the northward directionality of  
482 tsunami energy for this source, the most impacted areas are located. This is further confirmed  
483 in the maximum envelope of surface elevation shown in Fig. 9 for the similar M9-PRT2  
484 source. A movies showing animated results of the M9-PRT3 source simulation is provided  
485 as supplementary material (PRT3.mp4).

486 As for the ACZ/LSB sources, Figs. 8c-e show that an intense refraction of incident  
487 tsunami waves occurs at the shelf break and over the continental shelf, which makes wave  
488 crests increasingly parallel to the local isobaths. Comparing these results to Figs. 6f-h, we

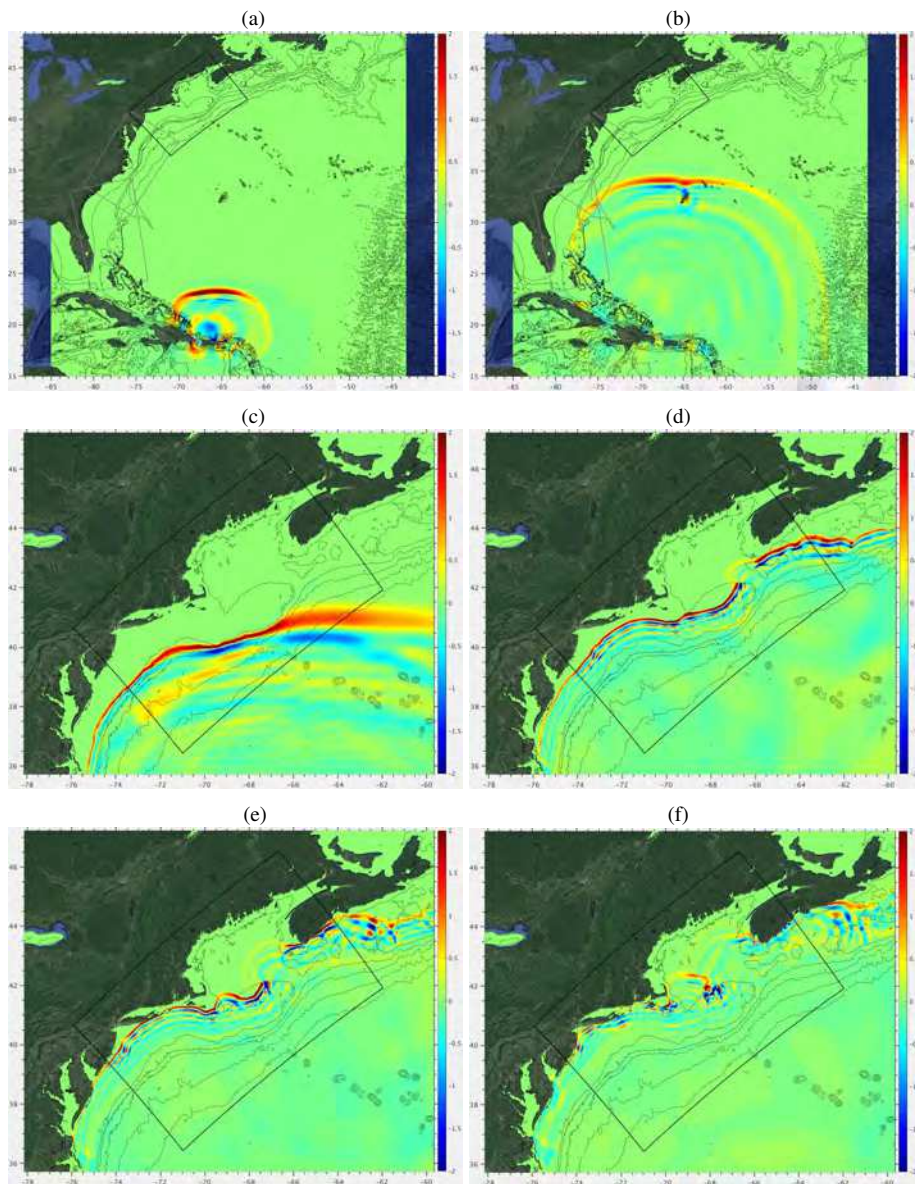


**Fig. 8** Snapshots of surface elevations (color scale in meter) for the PRT/Caribbean arc source M9-PRT3 (Table 3; Fig. 5h), at  $t =$  (a) 0.5, (b) 2, (c) 3, (d) 4, (e) 4.5, and (f) 5 h. Some isobaths are plotted for reference, but without labels to simplify the figures. Higher resolutions results are used wherever available.

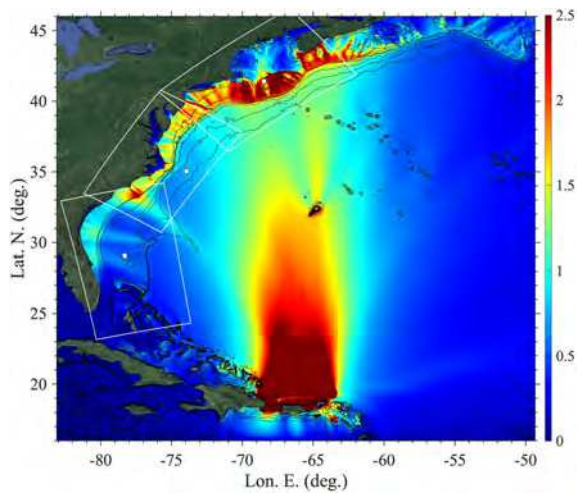


**Fig. 9** Envelope of maximum surface elevation computed with FUNWAVE during 24h of simulations in grid Local G0 (Table 4; Fig. 1) for the M9-PRT3 coseismic source (with parameters listed in Table 3 and initial surface elevations in Figs. 5h). Color scales are surface elevation in meter.

489 see that wave focusing-defocusing caused by refraction over the wide and shallow shelf,  
 490 particularly around ridges and canyons in the bottom bathymetry, yields a corresponding  
 491 modulation of tsunami coastal impact that is independent from the initial tsunami direction-  
 492 ality. Detailed results of coastal impact, discussed later, will confirm that these modulation  
 493 patterns are identical for the ACZ/LSB or PRT sources, which are originated eastward and  
 494 southward, respectively. This leads to the same areas of the coast always being subjected  
 495 to more or less tsunami hazard, whatever the tsunami source origin. This phenomenon was  
 496 already noted in earlier work, for other tsunami sources affecting the USEC [27,54,45].

497 Finally, for each source, the relevance of the one-way coupling method is verified by  
 498 comparing time series of surface elevations at the 9 save points (Table 3.1), in the coarser  
 499 grids Larger G0/Local G0 and the finer nested grids G1, G2 and G3. For instance, Figures  
 500 10 and 11 show time series of surface elevations computed for the M9-HSP1 and M9.0-  
 501 PRT1 sources. At most locations, there is a good agreement of the coarse and finer grid  
 502 simulations for the first few hours of tsunami impact. Once reflected waves from the coast  
 503 propagate back to the save points, however, differences become larger as reflection is more  
 504 accurately computed in the finer grids. Differences are largest at point P-G1, which is on  
 505 the shelf in shallower water and closer to shore, east of Cape Cod. Overall, the agreement  
 506 of time series computed in different grids confirms the relevance of the one-way coupling  
 507 methodology in nested grids used here. Time series of surface elevations at save points look  
 508 qualitatively similar for the other ACZ/LSB and PRT sources and will not be repeated here.

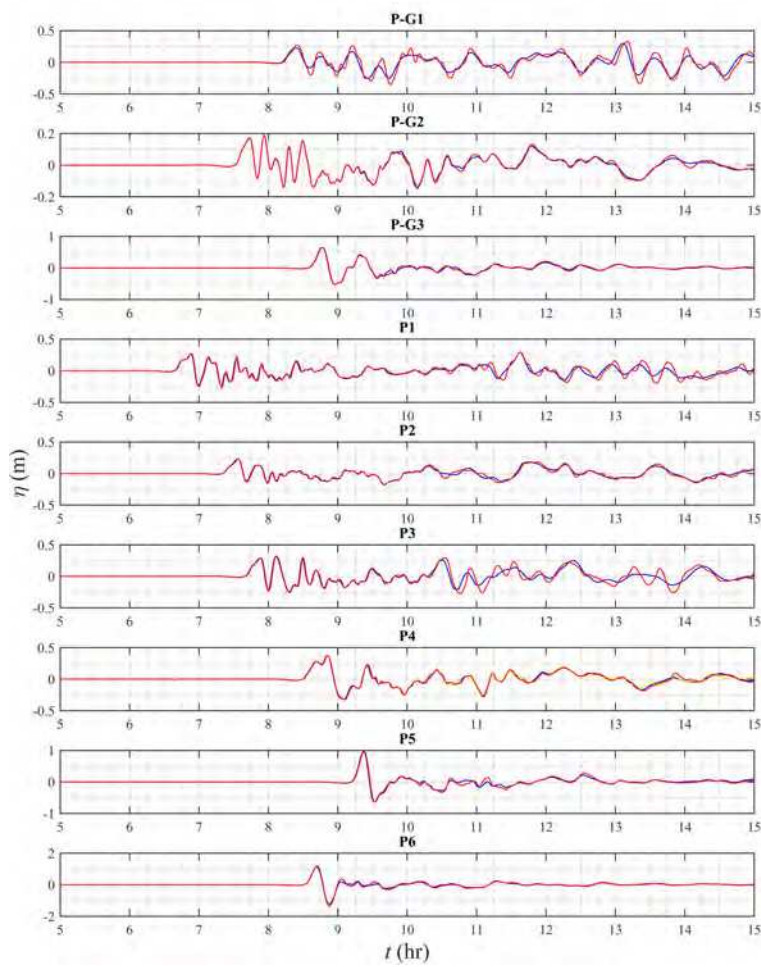


**Fig. 10** Time series of surface elevations computed for the M9-HSP1 source (Table 1), at the 9 save points defined in Table 5 (shown in Figs. 1): (blue lines) in grid Large G0; (red lines) in nested grids G1-G3. For point P4, yellow indicates surface elevation computed in G2, red indicates surface elevation computed in G3.

## 509 4 Results of tsunami coastal impact

### 510 4.1 Tsunami hazard metrics

#### 511 4.1.1 Definition of hazard metrics and classes

512 For each of the ten ACZ/LSB (Table 1; Fig. 4 and eight PRT/Caribbean arc coseismic  
 513 sources (Table 3; Fig. 5) simulated with FUNWAVE, coastal impact was computed in the  
 514 three nested grids (G1, G2, G3) along the 5 m isobath that parallels the USEC (considering  
 515 the coarse coastal grids used here). FUNWAVE results were interpolated at a large number

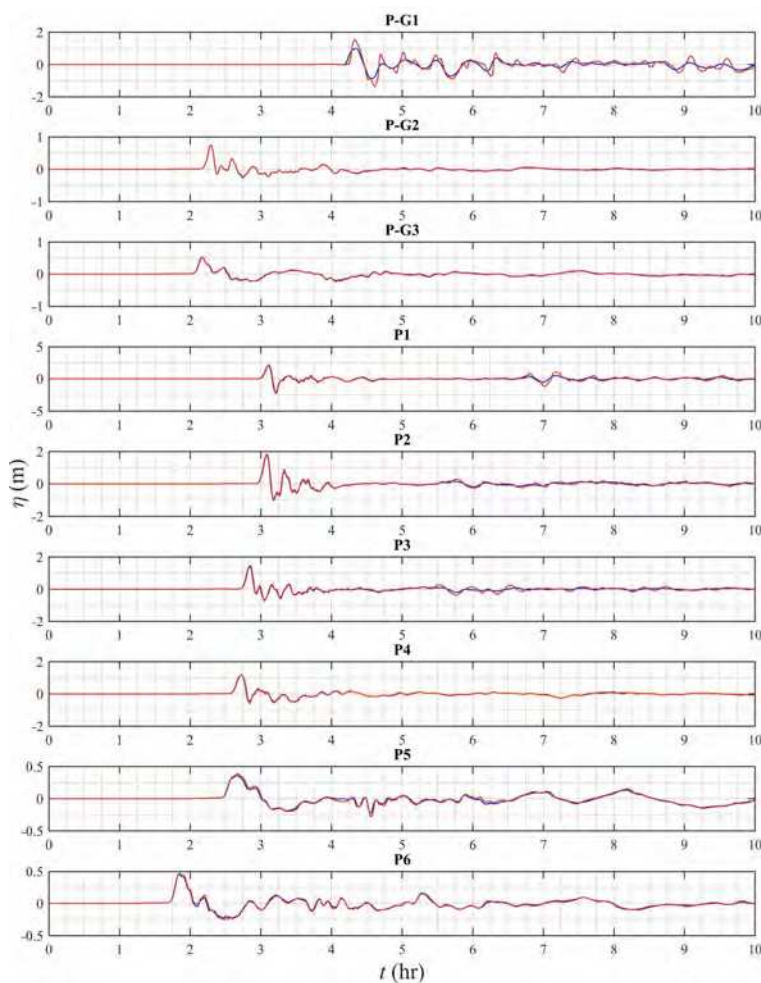


**Fig. 11** Time series of surface elevations computed for the M9-PRT3 source (Table 3), at the 9 save points defined in Table 5 (shown in Figs. 1): (blue lines) in grid Local G0; (red lines) in nested grids G1-G3. For point P4, black indicates surface elevation computed in G2, red indicates surface elevation computed in G3.

516 of coastal save points defined by their latitude-longitude coordinates along the isobath. For  
 517 clarity, in most of the results and figures,  $J = 18,201$  save points are used, which exclude  
 518 large bays (i.e., Chesapeake and Delaware bays, and Long Island Sound); when large bays  
 519 are considered, an additional 10,210 save points are specified within the bays ( $J = 28,411$ ).  
 520 Based on these results, values of four tsunami hazard metrics  $M_i$  ( $i = 1, \dots, 4$ ) were com-  
 521 puted for each source along the isobath: (1) maximum tsunami elevation  $M_1 = \eta_{max}$ , (2)  
 522 current  $M_2 = U_{max}$ , and (3) momentum force  $M_3 = F_{max}$ , as well as (4)  $M_4 = 1/t_a$ ,  
 523 function of arrival time  $t_a$  (here a large arrival time corresponds to a low hazard). These  
 524 metrics quantify inundation hazard, navigational hazard nearshore and in harbors, hazard

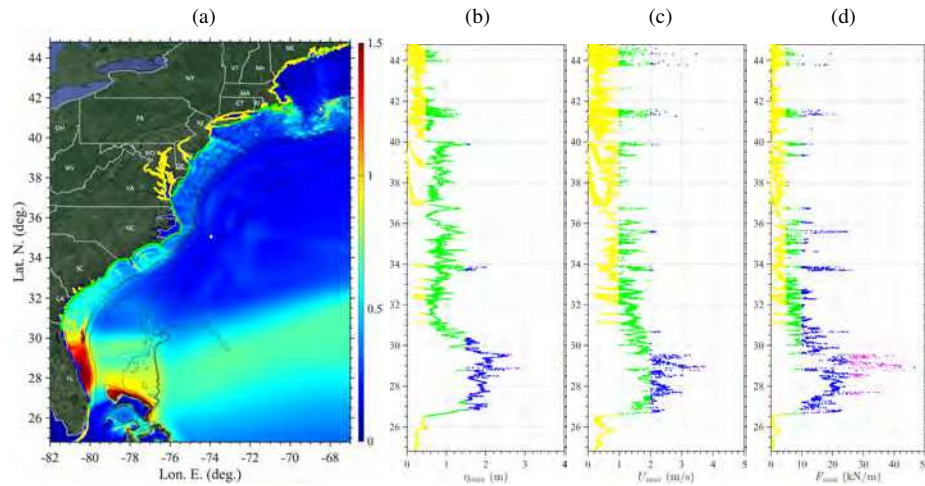


**Fig. 12** Hazard metrics along the USEC for the M9.0-HSP1 coseismic source (Table 1; Fig. 4i): (a) envelope of maximum surface elevations  $\eta_{max}$  over grids G1,G2,G3 (color scale in meter; colored dots along the coast correspond to hazard intensity  $C_k^1$  from (b)); (b,c,d) color coded hazard intensity classes  $C_k^i$  ( $k = 1, \dots, 5$ ; yellow, green, blue, magenta and red; Table 6) with corresponding values of: ( $i = 1$ )  $\eta_{max}$ , ( $i = 2$ )  $U_{max}$ , and ( $i = 3$ )  $F_{max}$ , respectively, in the same grids;  $J = 28,401$  save points are defined along the 5 m isobath, here including large bays.

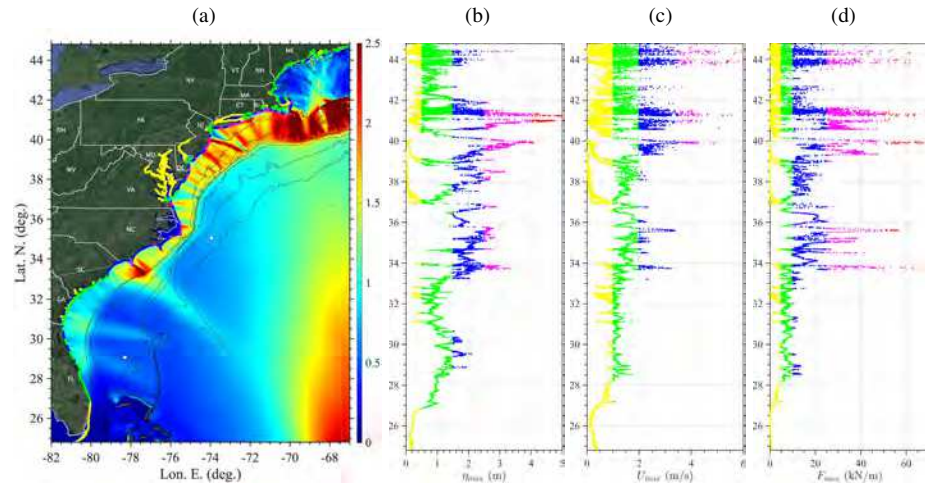


**Fig. 13** Same results as in Fig. 12, for the M9.0-PRT3 coseismic source (Table 3; Fig. 5h).

525 from tsunami impact forces on structures, and hazard resulting from low warning time, re-  
526 spectively.

527 FUNWAVE outputs directly provide  $\eta$  and horizontal current components ( $u, v$ ) (at  
528 0.531 times the local depth) at each grid point as a function of time, based on which  $\eta_{max}$ ,  
529  $U_{max} = \max\{\sqrt{u^2 + v^2}\}$ , and  $F_{max} = \max\{\rho(d + \eta)U^2\}$  are computed over the en-

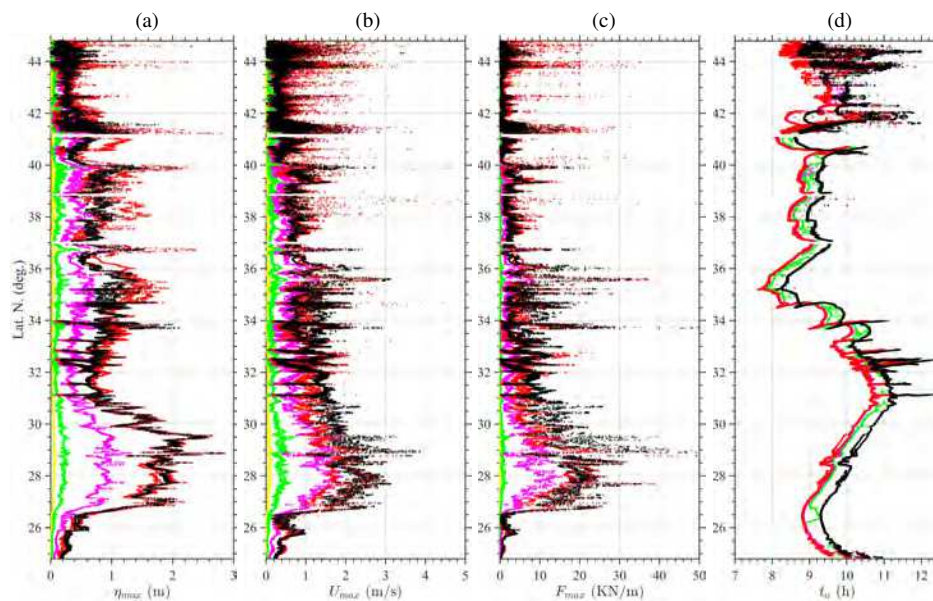


**Fig. 14** Envelope at the 5 m isobath ( $J = 18, 201$  save points excluding large bays) of maximum tsunami: (a) elevation; (b) current; (c) momentum force; and (d) arrival time, computed in grids G1,G2,G3, for the ten ACZ/LSB sources (Table 1; Fig. 4): (green) M8.0-MTR1, M8.0-MTR2; (yellow) M8.3-MTR1, M8.3-MTR2; (magenta) M8.7-MTR1, M8.7-MTR2; (red) M9.0-MTR1, M9.0-MTR2; and (black) M9.0-HSP1, M9.0-HSP2. Note, arrival times for the latter two sources, which are slightly longer, are not shown for clarity.

530 tire duration of simulations at all grid point. Figures 7 and 9, show examples of maximum  
 531 surface elevations computed over the entire computational domain for some of the tsunami  
 532 sources. These results are then interpolated at the save points along the 5 m isobath. Tsunami  
 533 arrival time is calculated along the same isobath, as the time when a positive or negative sur-  
 534 face elevation first occurs over a threshold, i.e.,  $t_a$  (in hours) is the minimum time such that  
 535  $|\eta(t_a, x_j, y_j)| \geq \Delta\eta$ ; where  $(x_j, y_j)$  ( $j = 1, \dots, J$ ) denotes the save points along the  
 536 isobath and here  $\Delta\eta = 0.01$  m. Since tsunamis are very small amplitude waves relative  
 537 to depth in most of their propagation, their celerity is well approximated as a function of  
 538 depth by the linear long wave celerity,  $c = \sqrt{gd}$ , which is not amplitude dependent; hence  
 539 different tsunamis originated from the same area propagate similarly along the same “wave  
 540 rays”. This similarity of propagation to shore is further reinforced by refraction that takes  
 541 place in large depth for long tsunami waves and causes each tsunami to propagate similarly  
 542 over the wide USEC shelf, whatever its origin. Consequently, tsunamis of different mag-  
 543 nitude originated from the same area, LSB/ACZ or PRT/Caribbean arc, should have very  
 544 similar arrival times along the USEC, which will be verified in results. One caveat is, for the  
 545 weakest LSB/ACZ M8 and M8.3 sources that approach areas of the USEC featuring bays  
 546 and more complex shoreline geometries, with a small amplitude, and hence only reach the

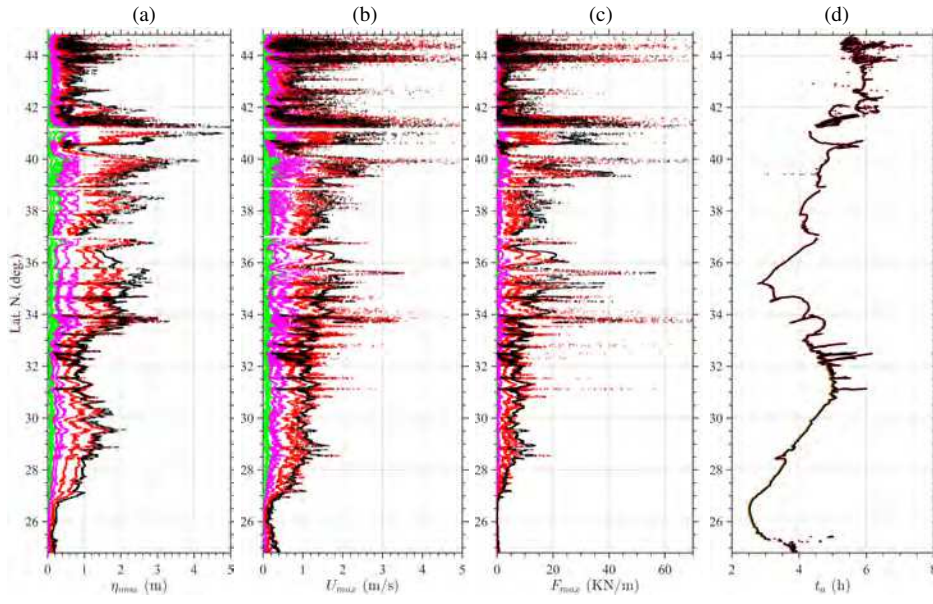


**Fig. 15** Envelope at the 5 m isobath ( $J = 18$ , 201 save points excluding large bays) of maximum tsunami: (a) elevation; (b) current; (c) momentum force; and (d) arrival time, computed in grids G1,G2,G3, for the eight PRT/Caribbean arc sources (Table 2.2; Fig. 5): (green) M8.3-PRT1, M8.3-PRT2, M8.3-PRT3; (magenta) M8.7-PRT1, M8.7-PRT2; (red) M9.0-PRT2, M9.0-PRT3; and (black) M9.0-PRT3. Note, arrival times for the latter source, which is similar, is not shown for clarity.

Hazard Metric	$C_1^i$	$C_2^i$	$C_3^i$	$C_4^i$	$C_5^i$
$M_1 = \eta_{max}$ (m)	[0-0.5[	[0.5-1.5[	[1.5-2.5[	[2.5-4[	> 4
$M_2 = U_{max}$ (m/s)	[0-1[	[1-2[	[2-3.5[	[3.5-5[	> 5
$M_3 = F_{max}$ (kN/m)	[0-5[	[5-10[	[10-25[	[25-50[	> 50
$M_4 = 1/t_a$ (1/h)	[0-0.1[	[0.1-0.17[	[0.17-0.25[	[0.25-0.50[	> 0.50

**Table 6** Class limits [ $C_{k,min}^i - C_{k,max}^i$ ], with ( $k = 1, \dots, 5$ ) of hazard intensity (low, low-medium, medium, high, to highest hazard), for four hazard metrics  $M_i$  ( $i = 1, \dots, 4$ ) used to compute the Tsunami Intensity Index (TII) with Eq. (3).

547  $\Delta\eta$  threshold later in their propagation, due to shoaling and reflection of the tsunami wave  
 548 trains. This tends to increase the arrival time for these sources in some areas. Details will be  
 549 shown later.

550 Once the four hazard metrics computed, to more easily identify areas facing lesser or  
 551 larger hazard, similar to classes defined by Boschetti et al. [10] for the first two metrics in  
 552 their tsunami intensity scale, we define five intensity classes, referred to as  $C_k^i$ ;  $k = 1, \dots, 5$   
 553 for each of the four metrics, with ranges of values [ $C_{k,min}^i - C_{k,max}^i$ ] from low to increasing  
 554 hazard severity (Table 6). These classes of hazard for each metric can also be referred to as:

555 low, low-medium, medium, high, and highest hazard. As discussed in Boschetti et al. [10],  
 556 who reviewed other relevant work to date, the selected values for maximum inundation  
 557  $\eta_{max}$  correspond, for adult pedestrians, to being up to knee-tight deep for class  $C_1^1$ , up  
 558 to chest/head deep for class  $C_2^1$ , up to head to overhead deep for  $C_3^1$  while loosing the  
 559 ability to feel the terrain, and then very deep; in classes  $C_3^1$  and higher, people would be  
 560 forced to swim or have to find high ground or vertically evacuate to be safe. Likewise, for  
 561 maximum currents  $U_{max}$  (see also Lynett et al. [38]), adult pedestrians would only be able  
 562 to fight the current in classes  $C_1^2$  and  $C_2^2$ , while navigation would start being gradually  
 563 and then severely impeded nearshore and in harbors for classes  $C_2^2$  and above. Maximum  
 564 momentum force  $F_{max}$  classes correspond to most structures resisting up to most structures  
 565 suffering significant damage or destruction, except for the strongest concrete or steel-built  
 566 (also elevated) structures. Finally, regarding arrival time, the classes reflect going from large  
 567 enough time (10 h) to evacuate most of the population from high hazard areas to not having  
 568 enough time (2 h) for warning and evacuating a meaningful fraction of the population at  
 569 risk. For each source considered here, and for their envelopes, values of the four metrics  
 570  $M_i$  were computed along the 5 m isobath and then sorted out by class. Plots of each metric  
 571 along the isobath were made, which were color coded as a function of the corresponding  
 572 class for the metric,  $C_k^i$ : yellow, green, blue, magenta, and red, for  $k = 1, 2, 3, 4, 5$ .

#### 573 4.1.2 Overall results of hazard metrics and classes

574 Figures 12 and 13 show examples of results of the first 3, physical, metrics computed  
 575 computed in grids G1,G2,G3, at  $J = 28, 401$  save points on the 5 m isobath, here in includ-  
 576 ing large bays, for the M9-HSP1 ACZ/LSB source (Table 1; Fig. 4i) and the M9.0-PRT3  
 577 PRT/Caribbean arc source (Table 3; Fig. 5h). In each figure, panel (a) shows the envelope of  
 578 maximum elevation, and panels (b,c,d) show the maximum elevation, current, and force, at  
 579 the 5 m isobath, color-coded with their hazard class intensity  $C_k^i$  value; the class intensity  
 580 value of surface elevation along is also marked in (a) along the coast.

581 As for the envelope in grids Local/Large G0 shown in Figs. 7 and 9, we first observe  
 582 an overall effect of the tsunami directionality on coastal impact, with the 15 deg. strike  
 583 ACZ/LSB source (M9.0-HSP1) affecting more the lower USEC and the Caribbean Islands,  
 584 and the PRT source (M9.0-PRT3) affecting more the upper USEC. Additionally, as before,  
 585 for both sources, there is a fine scale modulation of tsunami impact along the USEC, as a  
 586 function of the bathymetry (particularly on the shelf break and shelf) due to refraction caus-  
 587 ing wave focusing/defocusing on specific areas of the coast with convex/concave isobath  
 588 geometry, respectively. For both of these sources and for the three plotted metrics, there are  
 589 many locations in the 3rd and 4th hazard class and a few in the 5th, highest hazard class for

590 maximum elevation and current. This is expected and these are among the largest magni-  
 591 tude sources. Computed results look qualitatively similar for the other, smaller magnitude,  
 592 ACZ/LSB and PRT sources and will not be detailed here individually. However, their overall  
 593 impact on the USEC is compared with each other next.

594 Thus, Figs. 14 and 15 show a comparison of tsunami coastal impact at  $J = 18, 201$   
 595 save points along the 5 m isobath, here excluding large bays, for the four hazard metrics  
 596  $M_i$ , of the ten ACZ/LSB sources (Table 1) and eight PRT/Caribbean arc sources (Table 3),  
 597 respectively. Tables 7 and 8 provide statistics computed based on these results, for the: mean,  
 598 standard deviation, root-mean-square and average of the top 33, 10, 1 and 0.1 percentiles, of  
 599 the first three metrics. For the 3 physical hazard metrics, results in Tables 7 and 8 show the  
 600 expected trend of the statistics with the intensity of each metric statistics increasing with the  
 601 source magnitude, except for 0.1 percentile results which only average 18 individual results  
 602 and hence are more sensitive to a few noisy results. One exception is the two M9.0-HSP1  
 603 and -HSP2 sources in the ACZ area, which due to the effect of the MTR, cause a slightly  
 604 lower overall impact on the USEC than the two M9.0-MTR1 and -MTR2 sources which  
 605 are sited west of the MTR. Due to sources' directivity and refraction, the overall impact of  
 606 ACZ/LSB sources is larger on the southern USEC (south of 35 deg. N), whereas it is the  
 607 opposite for the PRT/Caribbean arc sources.

608 Regarding the arrival time metric, Figs. 14d show, as expected, that all the arrival times  
 609 are quite close to each other, ranging between 7.75 and 12.5 h, except for a few larger  
 610 spurious values for the weakest ACZ sources. Note that overall, the M9 sources located  
 611 further east in the HSP have an arrival time about 30 min larger than for the M9 sources  
 612 located in the MTR. The arrival times for the ACZ/LZB sources are mostly in hazard class  
 613 2, with a smaller fraction of values in hazard class 1. For the PRT sources, Fig. 15d shows  
 614 that arrival times are shorter than for ACZ sources (2.5-7.25 h), but follow a similar pattern  
 615 along the coast, due to the similar refraction over the wide shelf. The PRT arrival times are  
 616 nearly the same for all sources (within a few minutes from each other) and fall mostly within  
 617 the medium and high hazard classes (3 and 4).

#### 618 *4.1.3 Detailed results of hazard metrics and classes*

619 For ACZ sources, results of the 3 physical metrics in Figs. 14a-c and in Table 7 show that  
 620 the two M8.0 sources, which have 32 times less energy than the M9.0 sources (see Eq. 1),  
 621 only cause a  $\sim 0.03$  m average maximum elevation along the USEC, with a 0.03 or 0.013  
 622 m standard deviation, and the two M8.3 sources, which have 11 times less energy than the  
 623 M9.0 sources, a  $\sim 0.09$  m average maximum elevation with a 0.07 standard deviation.  
 624 Average maximum currents and forces are commensurate with these values and small for

$\eta$ (m)	$\mu_\eta$	$\sigma_\eta$	$\eta_{rms}$	$\eta_{1/3}$	$\eta_{1/10}$	$\eta_{1/100}$	$\eta_{1/1000}$
M8.0-MTR1	0.032	0.031	0.044	0.053	0.079	0.205	0.637
M8.0-MTR2	0.025	0.013	0.028	0.040	0.054	0.072	0.085
M8.3-MTR1	0.091	0.068	0.113	0.161	0.230	0.438	0.975
M8.3-MTR2	0.085	0.061	0.104	0.148	0.217	0.369	0.7234
M8.7-MTR1	0.319	0.218	0.386	0.566	0.807	1.102	1.374
M8.7-MTR2	0.297	0.222	0.371	0.546	0.799	1.101	1.375
M9.0-MTR1	0.652	0.488	0.814	1.226	1.694	2.299	2.700
M9.0-MTR2	0.601	0.490	0.775	1.163	1.713	2.292	2.680
M9.0-HSP1	0.598	0.435	0.740	0.897	1.397	2.179	2.639
M9.0-HSP2	0.606	0.436	0.747	0.907	1.426	2.107	2.517
$U$ (m/s)	$\mu_U$	$\sigma_U$	$U_{rms}$	$U_{1/3}$	$U_{1/10}$	$U_{1/100}$	$U_{1/1000}$
M8.0-MTR1	0.056	0.109	0.122	0.115	0.236	0.892	2.108
M8.0-MTR2	0.038	0.086	0.094	0.076	0.134	0.405	1.731
M8.3-MTR1	0.165	0.184	0.247	0.319	0.547	1.417	2.581
M8.3-MTR2	0.159	0.177	0.238	0.312	0.533	1.320	2.554
M8.7-MTR1	0.466	0.340	0.577	0.841	1.235	1.863	2.400
M8.7-MTR2	0.441	0.338	0.556	0.815	1.209	1.806	2.149
M9.0-MTR1	0.756	0.473	0.892	1.280	1.704	2.571	5.011
M9.0-MTR2	0.814	0.579	0.999	1.465	2.051	3.027	5.009
M9.0-HSP1	0.747	0.549	0.927	1.127	1.763	2.749	3.593
M9.0-HSP2	0.819	0.605	1.019	1.263	1.908	2.841	3.516
$F$ (kN/m)	$\mu_F$	$\sigma_F$	$F_{rms}$	$F_{1/3}$	$F_{1/10}$	$F_{1/100}$	$F_{1/1000}$
M8.0-MTR1	0.024	0.199	0.200	0.063	0.176	1.295	4.919
M8.0-MTR2	0.010	0.205	0.206	0.027	0.067	0.373	3.033
M8.3-MTR1	0.159	0.375	0.407	0.397	0.880	3.280	4.501
M8.3-MTR2	0.134	0.234	0.270	0.335	0.695	1.476	2.749
M8.7-MTR1	1.374	2.209	2.601	3.360	6.634	14.065	23.618
M8.7-MTR2	1.285	2.116	2.476	3.202	6.447	13.277	19.043
M9.0-MTR1	3.576	4.636	5.855	8.307	15.277	24.486	36.386
M9.0-MTR2	4.051	5.528	6.853	9.798	17.688	30.455	42.936
M9.0-HSP1	3.788	5.796	6.924	6.722	14.539	31.737	55.390
M9.0-HSP2	4.424	6.029	7.477	7.929	16.093	30.003	49.653

**Table 7** Statistics of simulation results computed at  $J = 18,201$  save points along the 5 m isobath (excluding large bays) for LSB/ASZ sources (Table 1; Fig. 14): mean, standard deviation, root-mean-square and average of the top 33, 10, 1 and 0.1 percentiles of maximum elevation  $\eta$  (m), flow velocity  $U$  (m/s), and momentum force  $F$  (kN/m).

$\eta$ (m)	$\mu_\eta$	$\sigma_\eta$	$\eta_{rms}$	$\eta_{1/3}$	$\eta_{1/10}$	$\eta_{1/100}$	$\eta_{1/1000}$
M8.3-PRT1	0.148	0.108	0.183	0.274	0.384	0.561	0.696
M8.3-PRT2	0.086	0.056	0.103	0.149	0.210	0.326	0.484
M8.3-PRT3	0.046	0.030	0.055	0.075	0.102	0.208	0.410
M8.7-PRT1	0.216	0.145	0.260	0.382	0.540	0.747	0.841
M8.7-PRT2	0.377	0.225	0.439	0.659	0.803	0.855	0.903
M9.0-PRT1	0.991	0.634	1.177	1.745	2.334	3.148	3.765
M9.0-PRT2	0.800	0.540	0.965	1.429	1.969	2.921	3.947
M9.0-PRT3	1.164	0.786	1.404	2.087	2.852	4.217	4.868
$U$ (m/s)	$\mu_U$	$\sigma_U$	$U_{rms}$	$U_{1/3}$	$U_{1/10}$	$U_{1/100}$	$U_{1/1000}$
M8.3-PRT1	0.208	0.176	0.272	0.381	0.605	1.226	1.956
M8.3-PRT2	0.128	0.117	0.174	0.229	0.374	0.901	1.807
M8.3-PRT3	0.061	0.054	0.082	0.104	0.167	0.440	0.763
M8.7-PRT1	0.305	0.226	0.379	0.534	0.8123	1.512	2.277
M8.7-PRT2	0.530	0.341	0.630	0.904	1.276	2.035	2.562
M9.0-PRT1	1.232	0.719	1.426	2.005	2.820	4.111	4.938
M9.0-PRT2	1.120	0.905	1.440	2.009	3.188	6.232	7.688
M9.0-PRT3	1.255	0.748	1.461	2.062	2.862	4.604	6.602
$F$ (kN/m)	$\mu_F$	$\sigma_F$	$F_{rms}$	$F_{1/3}$	$F_{1/10}$	$F_{1/100}$	$F_{1/1000}$
M8.3-PRT1	0.270	0.504	0.571	0.654	1.359	3.946	6.248
M8.3-PRT2	0.100	0.254	0.273	0.237	0.508	1.928	4.701
M8.3-PRT3	0.025	0.092	0.095	0.058	0.132	0.695	1.700
M8.7-PRT1	0.524	0.688	0.865	1.184	2.207	4.253	5.287
M8.7-PRT2	1.378	1.252	1.862	2.886	4.143	5.1682	5.776
M9.0-PRT1	9.060	10.937	14.202	19.289	34.444	76.255	107.810
M9.0-PRT2	6.995	10.026	12.225	16.012	30.981	65.731	92.363
M9.0-PRT3	9.914	10.950	14.771	21.291	35.827	63.969	108.922

**Table 8** Statistics of simulation results computed at  $J = 18$ , 201 save points along the 5 m isobath (excluding large bays) for PRT sources (Table 2.2; Fig. 15): mean, standard deviation, root-mean-square and average of the top 33, 10, 1 and 0.1 percentiles of maximum elevation  $\eta$  (m), flow velocity  $U$  (m/s), and momentum force  $F$  (kN/m).

625 the most part, with currents being less than 2 knots (1 m/s) at all but a few locations (in 0.1  
626 percentile). Note that larger current (and corresponding force) values can result here from  
627 the coarse grid resolution and insufficient energy dissipation by bottom friction nearshore.  
628 Overall, statistics show that the physical metrics for the M8 and M8.3 sources cause a low  
629 to medium-low hazard. For elevation, only 0.1% of elevation values are in a hazard class  
630 higher than 1; 0.1% of current values are in a hazard class higher than 2, and 99.9% of the  
631 force values are in hazard class 1. For the larger ACZ sources, results in Figs. 14a-c and  
632 in Table 7 show that, as expected, the largest hazard for the first three metrics is caused  
633 by the four M9.0 sources, with many values falling in the high/highest hazard classes 4/5

634 for each metric (Table 6). Among those, at many locations, slightly larger values of the  
635 three metrics are caused by the sources located west of the Madeira Torre Rise (MTR); but  
636 there are also locations where the sources located in the Horseshoe Plain (HSP) cause larger  
637 values. Looking at the detailed impact in the figures, South of 35.5 Lat. N. (approximately  
638 Cape Hatteras, NC), there are only small differences for the 3 metrics, between the sources  
639 located west of the MTR (M9-MTR1, M9-MTR2) and those east of it (M9-HSP1, M9-  
640 HSP2), with even some locations in the south where currents and forces are slightly larger  
641 for the latter two sources, indicating that here the Madeira Torre Rise (MTR) either does  
642 not affect tsunami propagation or reinforces it slightly. In contrast, north of 35 Lat. N. the  
643 tsunami hazard for the 3 metrics is larger for the M9 sources located west of the MTR  
644 than for the HSP sources, indicating that the shallow MTR ridge offers some protection  
645 from coseismic sources located in the area of the Lisbon 1755 event. Here, while maximum  
646 surface elevations reach similar maximum values as in the south, mostly in the high hazard  
647 category, currents and forces reach values in the highest hazard category at a larger number  
648 of locations.

649 Regarding the medium-high magnitude M8.7 LSB/ACZ sources, results in Figs. 14a-c  
650 and in Table 7 for the three metrics show that, overall, these sources, which are about 3  
651 times less energetic than the M9 sources (see Eq. 1), cause less impact at most locations  
652 than the M9 sources, while following the same pattern of highs and lows along the coast as  
653 for the M9 sources. However, at some isolated locations in the south, maximum elevation  
654 reaches up to 1.9 m for the M8.7 sources and in the north, particularly above 39 Lat. N  
655 (about Atlantic City, NJ), at a few locations currents and forces reach values nearly as large  
656 as those of the M9-HSP1 and M9-HSP2 sources. Clearly, this results from the complex  
657 tsunami propagation from the source, including wave interactions with the MTR near the  
658 source and with bathymetry and coastal features along the USEC shelf break and shelf.  
659 Resonances (seiching) can also be triggered nearshore due to different frequency content  
660 in the incident wave train, that may increase currents even if tsunami elevations are not  
661 significantly affected.

662 For PRT sources, Figs. 15a-c show that, as a result of refraction and an overall identical  
663 northward directivity of each PRT/Caribbean arc source, the impact of each source follows  
664 the same pattern of focusing/defocusing on the same coastal areas, with just a modulation of  
665 the intensity commensurate with the source magnitude. However, the overall intensity of the  
666 impact for the 3 physical metrics is 2-3 times smaller, south of 34 Lat. N. (approximately  
667 south of Cape Hatteras, NC), than north of it. So clearly the PRT/Caribbean arc sources  
668 mostly impact the areas less impacted by the ACZ/LSB sources.

669 Results of the 3 physical metrics for the PRT/Caribbean arc sources in Figs. 15a-c and  
670 in Table 8 show that the three M8.3 sources, which have about 21 times less energy than

671 the M9.0 sources (see Eq. 1), only cause a  $\sim 0.05 - 0.15$  m average maximum elevation,  
 672 with a 0.03-0.011 m standard deviation, and 0.4-0.7 m for the 0.1 percentile values. The two  
 673 M8.7 sources, which have 11 times less energy than the M9.0 sources, have a  $\sim 0.22 -$   
 674 0.38 m average maximum elevation with a 0.15-0.23 m standard deviation, and 0.8-0.9 m  
 675 for the 0.1 percentile values. Average maximum currents and forces for these sources are  
 676 commensurate with these inundation values and small for the most part, with currents being  
 677 less than 1.25 m/s (2.5 knots) at all but a few locations (in 0.1 percentile). Note that larger  
 678 current (and corresponding force) values can again result from the coarse grid resolution and  
 679 insufficient energy dissipation by bottom friction nearshore. Overall, statistics show that the  
 680 physical metrics for the M8.3 and M8.7 sources cause a low to medium-low hazard. Only  
 681 0.1% of maximum current values are in hazard class 3. Tsunami impact is more severe for  
 682 the three larger M9 PRT sources. Despite resulting from quite different fault areas, results  
 683 in Figs. 15a-c and in Table 8 show fairly similar overall impacts for the three M9 sources,  
 684 with moderate average values of the 3 metrics. However, there is large alongshore variation  
 685 of the metrics as confirmed by values in the two highest percentile (1 and 0.1 %), that all  
 686 fall in hazard classes 4/5, i.e., high to highest impact. Among the three sources M9.0-PRT3,  
 687 which was used as an extreme PMT source in earlier work, causes the maximum inundation  
 688 and forces, but M9.0-PRT2 causes slightly larger maximum currents for the 0, 1 and 0.1  
 689 percentile, all in the highest hazard category.

#### 690 4.2 tsunami Intensity Index (TII)

To provide an overall indicator of tsunami hazard intensity along the USEC, values of the  
 five hazard classes, computed for each source along the 5 m isobath for the four metrics,  
 were combined into a Tsunami Intensity Index (TII). The TII is defined as a weighed av-  
 erage of the class index values,  $k^i(x_j, y_j) = 0$  to 5 (from low hazard to highest hazard),  
 interpolated for the four metrics  $M_i$  ( $i = 1, \dots, 4$ ) (Table 6), at each save point location  
 $(x_j, y_j)$  ( $j = 1, \dots, J$ ), i.e.,

$$TII(x_j, y_j) = \sum_{i=1}^4 w_i k^i(x_j, y_j) \quad \text{with} \quad k^i(x_j, y_j) = \frac{M_i(x_j, y_j) - C_{k,min}}{C_{k,max} - C_{k,min}} \quad (3)$$

691 where  $w_i$  are weights associated with each metric, with  $\sum_i w_i = 1$ , and the  $k^i$ 's are com-  
 692 puted by first finding the hazard class within which each metric falls and then applying Eq.  
 693 (3). The TII hence is also on a scale of 0 to 5 and represents the overall tsunami hazard  
 694 intensity, from low to highest. If all metrics are given equal weight then we simply have  
 695  $w_i = 0.25$ ; however, as we shall see, the weights allow giving more importance to some  
 696 metrics than others.

697 In the following, we elected to give more weight to variables directly affecting the ability  
698 of the population to evacuate, i.e., maximum inundation height and current, and relatively  
699 less weight to forces on structures and arrival time; thus, we gave weights of  $w_i = [0.4, 0.3,$   
700  $0.15, 0.15]$  to each metric, respectively. The rationale for giving less weight to arrival time  
701 is that these are far-field coseismic tsunamis for which advanced warning would be imme-  
702 diately given upon the triggering of the event by an earthquake, hence somewhat mitigating  
703 this part of the hazard. However, any other combination of metric weights could be ap-  
704 plied and results easily generated. Figures 16 and 17 show the longshore distributions of TII  
705 values computed with these weights using Eq. (3), based on the four hazard metric results  
706 computed along the 5 m isobath for the LSB/ACZ (Fig. 14) and PRT/Caribbean arc (Fig. 15)  
707 sources, respectively. We see that the TII class values (which are color coded for different  
708 levels of hazard using the same color scheme as that of the hazard intensity classes) well  
709 summarize overall tsunami hazard and confirm the detailed observations made above on the  
710 individual hazard metrics results. The TII, however, provides a unique and simple indicator  
711 of the hazard intensity expected for each source at the many save points along the coast,  
712 that can be easily understood and used by emergency managers. Although these figures are  
713 plotted at large scale, all results produced can be easily zoomed into and/or imported into a  
714 GIS, to evaluate the hazard faced by any particular area or specific community.

#### 715 4.3 Estimating the effect of return period

716 Although the complete PTHA of tsunami hazard along the USEC will be addressed in future  
717 work, the approximate return periods provided in Tables 2 and 3 for each of the 18 coseismic  
718 sources whose impact was modeled along the USEC, allow drawing some preliminary con-  
719 clusions as of the expected intensity of tsunami hazard for different return periods. Specif-  
720 ically, the values of the TII and four associated hazard metrics, computed for each source  
721 along the coast, provide a measure of the intensity of the tsunami hazard as a function of the  
722 event return period.

723 Altogether, the sources simulated here cover an estimated range of return periods,  $T_r \in$   
724  $[70 - 2, 130]$  years, with the low end being the M8 ACZ sources and the high end the M9.0-  
725 PRT3 extreme source. While detailed results of each tsunami metric can be extracted for any  
726 save point along the coast, here, we only consider the overall statistics of the three physical  
727 tsunami metrics, maximum elevation, current and force given in Tables 7 and 8, to estimate  
728 ranges of expected values as a function of  $T_r$ . Based on these statistics, for instance, we see  
729 that the expected 0.1 percentile values up to return periods of  $\sim 100$  years are a maximum  
730 inundation  $\eta_{1/1000} \sim 0.7$  m, maximum current  $U_{1/1000} \sim 2$  m/s, and maximum force  
731  $F_{1/1000} \sim 5$  kN/m; up to  $\sim 250$  years, these values become 1.4 m, 2.4 m/s and 24 kN/m;

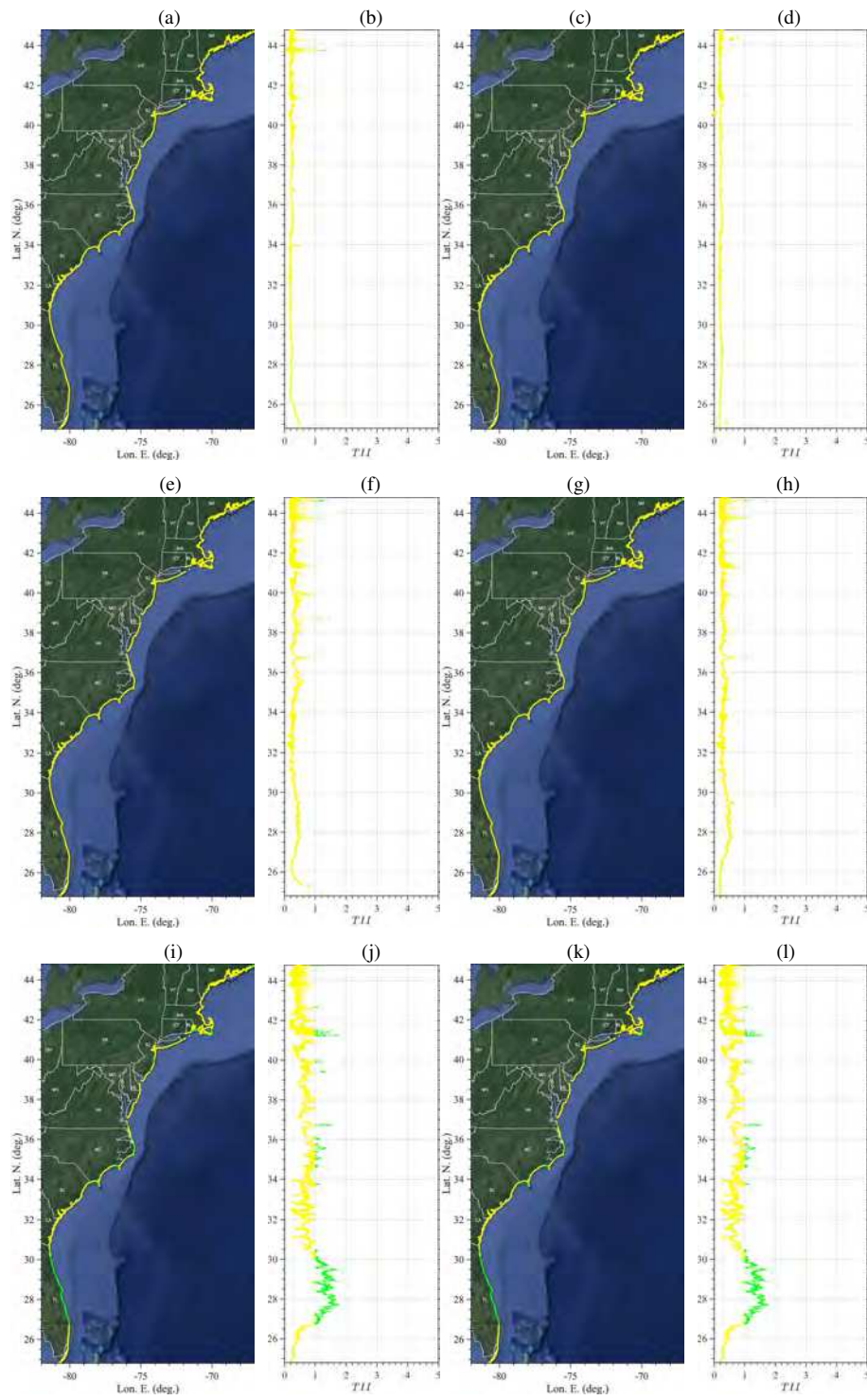
732 up to  $\sim 500$  years, they become 2.6 m, 5.0 m/s and 55 kN/m; and up to  $\sim 1,000$  years, they  
733 become 4 m, 7.7 m/s and 108 kN/m. Finally, up to  $\sim 2,000$  years, maximum inundation  
734 approaches 5 m, while the other metrics stay at the same level.

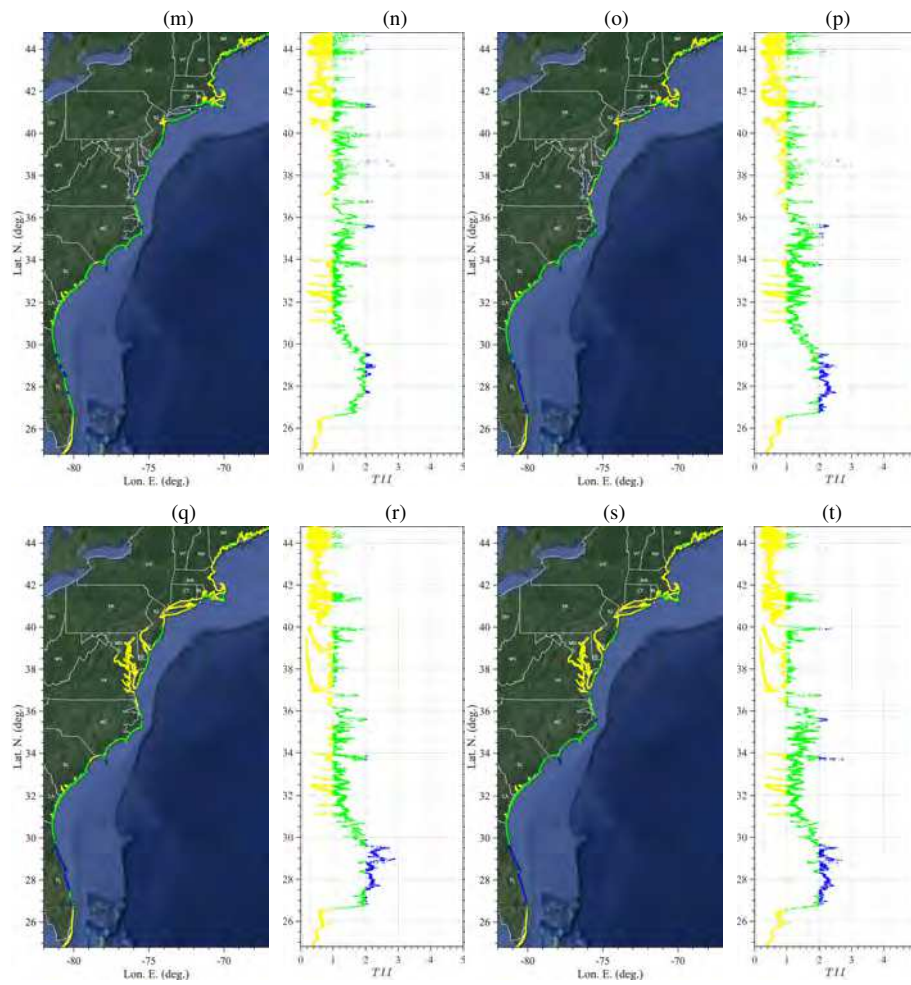
## 735 **5 Conclusions**

736 We presented the methodology for and overall results of model simulations conducted to  
737 simulate tsunami hazard along the USEC from a collection of 18 far-field coseismic sources  
738 ranging in magnitude from M8 to M9. These include 10 sources located in the ACZ area,  
739 ranging from M8 to M9 magnitude, with some representing Lisbon 1755 proxy (repeat)  
740 events and 8 sources in the PRT/Caribbean arc area from M8.3 to M9 magnitude. Results  
741 provide a comprehensive picture at the regional scale (i.e., at a coarse grid resolution) of  
742 the intensity of coastal tsunami hazard expected from each source in terms of 4 hazard  
743 metrics computed along the 5 meter isobath: (1) the maximum tsunami elevation, (2) current  
744 and (3) force, as well as tsunami arrival time. These metrics are combined into a single  
745 Tsunami Intensity Index (TII), whose value allows identifying areas and infrastructure at  
746 greater hazard from coseismic tsunamis.

747 The 18 sources have estimated return periods ranging approximately between 100 and  
748 2,000 years. For each source, the TII thus provides an overall tsunami hazard intensity  
749 along the USEC coast that allows both a comparison among sources and a quantification  
750 of tsunami hazard as a function of the source return period. The detailed values of each met-  
751 ric, both saved over the model grids and along the 5 m isobath, can help quantify tsunami  
752 hazard at any given coastal location in the 14 considered US coastal states, from Florida to  
753 Maine. These can also provide initial and boundary conditions to perform higher resolution  
754 inundation mapping simulations in areas identified as having a higher tsunami hazard.

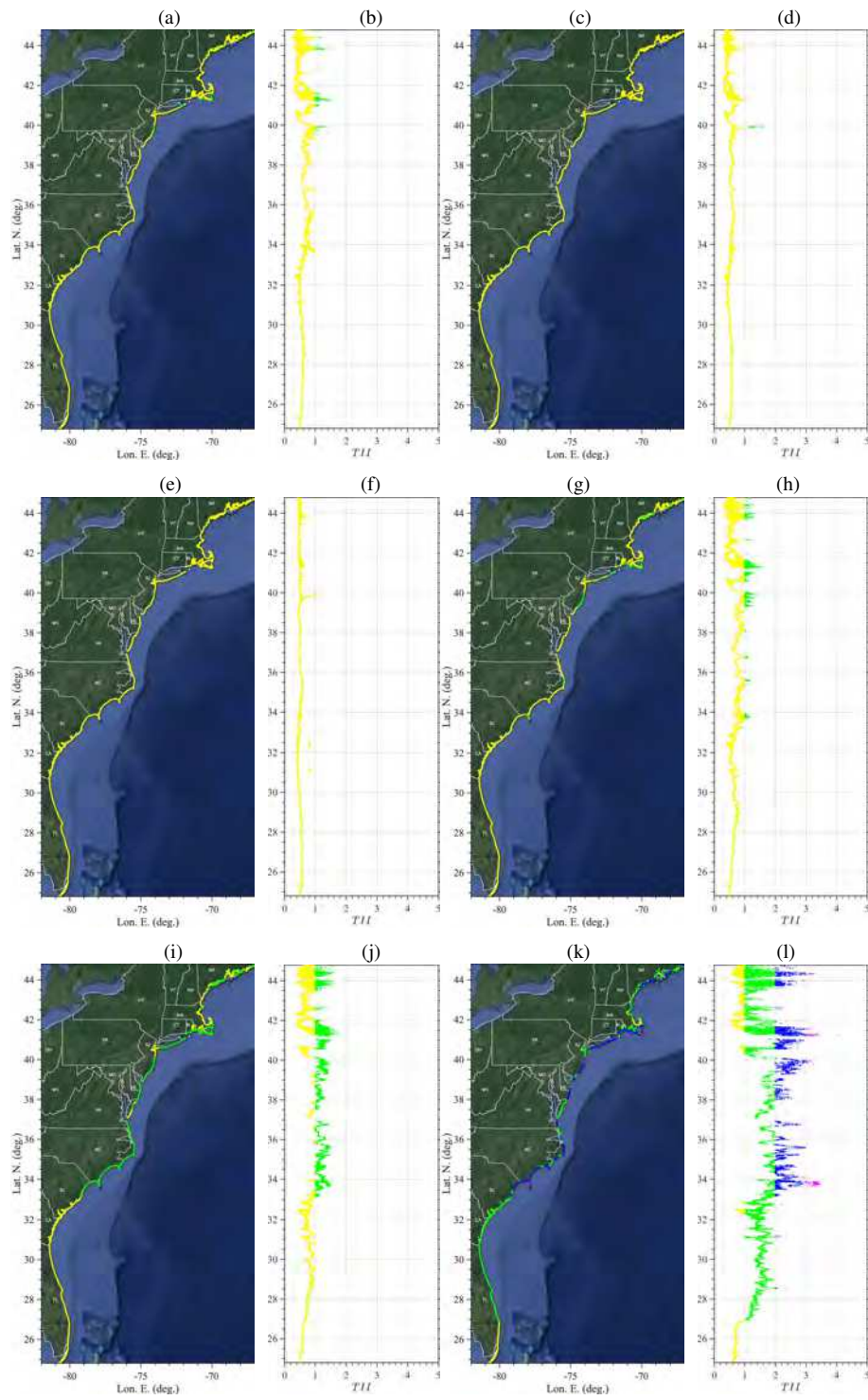
755 While earlier work only focused on the most extreme tsunami sources causing PMTs,  
756 whose return period was largely unknown, the present work covers a collection of sources  
757 to which approximate return periods are associated. Combined with other tsunami sources  
758 such as nearshore SMFs and far-field volcanic collapse into a logic tree, the 18 coseismic  
759 sources modeled here could thus contribute to future PTHA work along the USEC.





**Fig. 16** Tsunami intensity index computed for ten LSB/ACZ sources (Table 1; Fig. 4), based on results of the 4 hazard metrics in Fig. 14: (a,b) M8.0-MTR1; (c,d) M8.0-MTR2; (e,f) M8.3-MTR1; (g,h) M8.3-MTR2; (i,j) M8.7-MTR1; (k,l) M8.7-MTR2; (m,n) M9.0-MTR1; (o,p) M9.0-MTR2; (q,r) M9.0-HSP1; (s,t) M9.0-HSP2. TII metric weights are  $w_i = [0.40, 0.30, 0.15, 0.15]$ , and color coded hazard intensity classes are: (yellow) low; (green) medium low; (blue) medium (magenta) medium high, (red) heigh, and (black) extreme. Note, for the last 2 sources, the TII is also provided within the large bays.

760 However, pending such PTHA work, the overall estimates made here of tsunami hazard  
 761 intensity for several physical variables, as a function of the event return period, can help  
 762 put in perspective the tsunami hazard faced by the USEC with that resulting from other  
 763 more prominent natural disasters such as tropical cyclones. For the highest hazard areas  
 764 (0.1 percentile), we find that tsunami hazard in the 100-500 year return period range is  
 765 commensurate with that posed by category 3-5 tropical cyclones, taking into account the



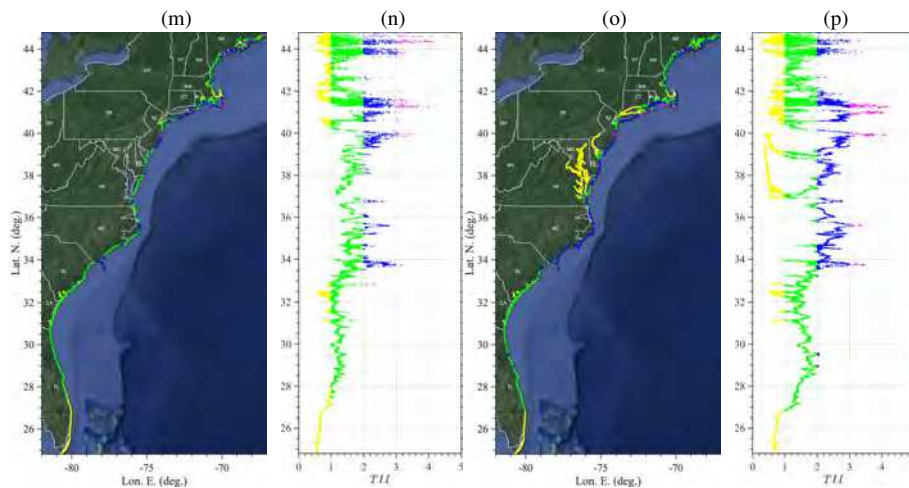


**Fig. 17** Tsunami intensity index computed for eight PRT/Caribbean arc sources (Table 3; Fig. 5), based on results of the 4 hazard metrics in Fig. 15: (a,b) M8.3-PRT1; (c,d) M8.3-PRT2; (e,f) M8.3-PRT3; (g,h) M8.7-PRT1; (i,j) M8.7-PRT2; (k,l) M9.0-PRT1; (m,n) M9.0-PRT2; (o,p) M9.0-PRT3. TII metric weights are  $w_i = [0.40, 0.30, 0.15, 0.15]$ , and color coded hazard intensity classes are: (yellow) low; (green) medium low; (blue) medium (magenta) medium high, (red) high, and (black) extreme. Note, for the last source, the TII is also provided within the large bays.

766 larger current velocities and forces caused by tsunami waves. Indeed, while the storm surge  
 767 caused by category 3-5 hurricanes can reach 4-6 m along the USEC [58], the resulting  
 768 coastal inundation is typically not associated with flow velocity and momentum forces as  
 769 large as those caused by the long tsunami waves which, hence, could be more damaging  
 770 even when associated with a smaller coastal inundation.

771 Results of our work are made available to USEC emergency managers, who will be  
 772 able to look at the most exposed areas to tsunami hazard and put the associated risk in  
 773 perspective with that resulting from other natural disasters and implement the necessary  
 774 mitigation measures.

## 775 6 Declarations

### 776 6.1 Funding

777 This work was supported in the United States by NOAA's National Weather Service (NWS),  
 778 through grants administered by the US National Tsunami Hazards Mitigation Program (NTHMP):  
 779 NA-13-NWS4670014, NA-14-NWS4670041, NA-15-NWS4670029, NA-16-NWS4670034,  
 780 NA-17-NWS4670010, NA-18-NWS4670073 and NA-19-NWS4670074. Numerical simula-  
 781 tions reported in this work used HPC resources, as part of the Extreme Science and Engi-

782 neering Discovery Environment (XSEDE) (project BCS-170015), which is supported by the  
783 National Science Foundation (NSF) grant number ACI-1548562.

#### 784 6.2 Conflicts of interest/Competing interests

785 None

#### 786 6.3 Availability of data and material (data transparency)

787 A Google Drive repository for all the raw data that was used to set up the tsunami models and  
788 model results has been created. This is in fact a requirement of the NTHMP program. The  
789 Google Drive will be finalized and made public once the paper is accepted for publication.  
790 Note that the raw data does not provide any useful information in itself regarding.

#### 791 6.4 Code availability

792 FUNWAVE-TVD, the tsunami model used in this work, is open source software available at  
793 <http://github.com/fengyanshi/FUNWAVE-TVD/>.

#### 794 6.5 Authors' contributions

795 SG: Led work, acquired funding, defined methodology, processed results and wrote most of  
796 the paper.

797 MM: Performed model simulations, did background literature work, post processed results,  
798 made some figures and proofread paper.

799 LS: Created model grids and performed model simulations for a few extreme sources, did  
800 background literature work, developed post-processing routines, and did some post process-  
801 ing of results.

802 AG: Co-led work, helps to acquire funding, defined some of the methodology, performed  
803 early tsunami simulations and developed initial post-processing routines, proofread paper.

#### 804 6.6 Ethics approval

805 Not applicable.

## 806 6.7 Consent to participate

807 Not applicable.

## 808 6.8 Consent for publication

809 Not applicable

810 **Acknowledgements** The authors gratefully acknowledge continuing support from NOAA's National Weather  
811 Service (NWS), through grants administered by the US National Tsunami Hazards Mitigation Program  
812 (NTHMP): NA-13-NWS4670014, NA-14-NWS4670041, NA-15-NWS4670029, NA-16-NWS4670034, NA-  
813 17-NWS4670010, NA-18-NWS4670073 and NA-19-NWS4670074. Numerical simulations reported in this  
814 work used HPC resources, as part of the Extreme Science and Engineering Discovery Environment (XSEDE)  
815 (project BCS-170015), which is supported by the National Science Foundation (NSF) grant number ACI-  
816 1548562. FUNWAVE-TVD is open source software available at [http://github.com/fengyanshi/FUNWAVE-](http://github.com/fengyanshi/FUNWAVE-TVD/)  
817 [TVD/](http://github.com/fengyanshi/FUNWAVE-TVD/).

818 **References**

- 819 1. Abadie S., Harris J.C., Grilli S.T. and R. Fabre, Numerical modeling of tsunami waves generated by the  
820 flank collapse of the Cumbre Vieja Volcano (La Palma, Canary Islands): tsunami source and near field  
821 effects, *Journal of Geophysical Research*, 117, C05030, doi:10.1029/2011JC007646 (2012)
- 822 2. Baptista, M. A., Heitor, S., Miranda, J.M., Miranda, P.M.A. and Mendes Victor, L., The 1755 Lisbon  
823 earthquake; evaluation of the tsunami parameters, *J. Geodynamics*, 25, 143-157 (1998a)
- 824 3. Baptista, M. A., Heitor, S., Miranda, J.M., Miranda, P.M.A. and Mendes Victor, L., Constraints on the  
825 source of the 1755 Lisbon tsunami inferred from numerical modeling of historical data on the source of the  
826 1755 Lisbon tsunami, *J. Geodynamics*, 25, 159-174 (1998b)
- 827 4. Baptista, M.A., Miranda, J. M., Chierici, F. and Zitellini, N., New study of the 1755 earthquake source  
828 based on multi-channel seismic survey data and tsunami modeling, *Nat. Haz. Earth Syst. Sc.*, 3, 333-340  
829 (2003)
- 830 5. Baptista, M. A. And Miranda, J. M., Revision of the Portuguese catalog of tsunamis. *Natural Hazards and*  
831 *Earth System Sciences*, 9(1), 25-42 (2009)
- 832 6. Baptista, M. A., Miranda, J. M., Batlló, J., Lisboa, F., Luis, J., and Macia?, R., New study on the 1941  
833 Gloria Fault earthquake and tsunami. *Natural Hazards and Earth System Sciences*, 16(8), 1967-1977 (2016)
- 834 7. Baptista, M.A., 2020, Tsunamis Along the Azores Gibraltar Plate Boundary. *Pure and Applied Geo-*  
835 *physics*, 177, 1713-1724 (2020)
- 836 8. Barkan, R., ten Brick, U.S. and Lin, J., Far field tsunami simulations of the 1755 Lisbon earthquake:  
837 Implication for tsunami hazard to the U.S. East Coast and the Caribbean, *Marine Geology*, 264, 109-122  
838 (2009)
- 839 9. Benford, B., DeMets, C., Calais, E. GPS estimates of microplate motions, northern Caribbean: evidence  
840 for a Hispaniola microplate and implications for earthquake hazard. *Geophys. J. Intl.*, 191(2), 481-490,  
841 doi:10.1111/j.1365-246X.2012.05662.x (2012)

- 842 10. Boschetti L., Ioualalen M., Nemati F., Grilli S.T., Dessa J.-X., and C. Larroque, Tsunami intensity scale  
843 based on wave amplitude and current applied to the French Riviera: the case study of local seismicity. *Nat.*  
844 *Hazards*, 102, 219-248, doi: 10.1007/s11069-020-03921-0 (2020)
- 845 11. Calais, E. And Mercier de Lepinay. B. Strike-slip tectonic processes in the northern Caribbean between  
846 Cuba and Hispaniola (Windward Passage). *Mar. Geophys. Res.*, 17(1), 63-95 (1995)
- 847 12. Calais, E., Freed, A., Mattioli, G., Amelung, F., Jónsson, S., Jansma, P., Hong, S-H., Dixon, T., Prépetit,  
848 C. and Momplaisir, R. Transpressional rupture of an unmapped fault during the 2010 Haiti earthquake. *Nat.*  
849 *Geoscience*, 3(11), 749-799, doi:10.1038/NGEO992 (2010)
- 850 13. Chaytor J.D., ten Brink U.S., Solow A.R., and B.D. Andrews, Size distribution of submarine landslides  
851 along the U.S. Atlantic margin. *Marine Geology*, 264(1-2):16-27 (2009)
- 852 14. Dawicki, S., Major Caribbean Earthquakes and Tsunamis a Real Risk: Events rare, but scientists call  
853 for public awareness, warning system, Media Relations, Woods Hole Oceanographic Institute, available at:  
854 <http://www.whoi.edu/page.do?pid=12460&tid=282&cid=2430> (last access: 13 December 2008 (2005)
- 855 15. DeMets, C., Earthquake slip vectors and estimates of present-day plate motions. *J. Geophys. Res.*, 98,  
856 6703-6714 (1993).
- 857 16. Gailler, A., Calais, E., Hébert, H., Roy, C., Okal, E. Tsunami scenarios and hazard assessment along the  
858 northern coast of Haiti. *Geophys. J. Intl.*, 203(3), 2287-2302, doi:10.1093/gji/ggv428 (2015)
- 859 17. Gica, E., M. C. Spillane, V. V. Titov, C. D. Chamberlin, and J. Newman, Development of the forecast  
860 propagation database for NOAA's Short-Term Inundation Forecast for Tsunamis, NOAA Tech. Memo.,  
861 OAR PMEL-139 (2008)
- 862 18. Glimsdal S., Pedersen G.K., Harbitz C.B., and F. Løvholt, Dispersion of tsunamis: does it really matter  
863 ?, *Nat. Hazards Earth Syst. Sci.*, 13, 1507-1526, doi:10.5194/nhess-13-1507-2013 (2013)
- 864 19. Grilli A.R. and S.T. Grilli, Modeling of tsunami generation, propagation and regional impact along  
865 the U.S. East Coast from the Azores Convergence Zone, Research Report no. CACR-13-04, 20 pps.,  
866 <http://personal.egr.uri.edu/grilli/grilli-grilli-cacr-13-04> (2013a)
- 867 20. Grilli A.R. and S.T. Grilli, Modeling of tsunami generation, propagation and regional impact along  
868 the upper U.S East coast from the Puerto Rico trench, Research Report no. CACR-13-02, 18 pps.,  
869 <http://personal.egr.uri.edu/grilli/grilli-grilli-cacr-13-02> (2013b)
- 870 21. Grilli, S.T., Grilli A.R., David, E. and C. Coulet, Tsunami Hazard Assessment along the North  
871 Shore of Hispaniola from far- and near-field Atlantic sources. *Natural Hazards*, 82(2), 777-810, doi:  
872 10.1007/s11069-016-2218-z (2016)
- 873 22. Grilli S.T., Ioualalen M., Asavanant J., Shi F., Kirby J.T., and P. Watts, Source constraints and model  
874 simulation of the December 26, 2004 Indian Ocean tsunami, *Journal of Waterway, Port, Coastal, and*  
875 *Ocean Engineering*, 33, 414-428 (2007)
- 876 23. Grilli S.T., Dubosq S., Pophet N., Pérignon Y., Kirby J.T., and F. Shi, Numerical simulation and first-  
877 order hazard analysis of large coseismic tsunamis generated in the Puerto Rico thrench: near-field impact  
878 on the North shore of Puerto Rico and far-field impact on the US East Coast, *Natural Hazards and Earth*  
879 *System Sciences*, 10, 2109-2125, doi:10.5194/nhess-2109-2010 (2010)
- 880 24. Grilli, S.T., J.C. Harris, T. Tajalibakhsh, T.L. Masterlark, C. Kyriakopoulos, J.T., Kirby and F. Shi Numerical  
881 simulation of the 2011 Tohoku tsunami based on a new transient FEM coseismic source: Comparison  
882 to far- and near-field observations, *Pure Appl. Geophys.*, 170, 1333-1359, doi:10.1007/s00024-012-0528-y  
883 (2013c)
- 884 25. Grilli S.T., O'Reilly C., Harris J.C., Tajalli-Bakhsh T., Tehranirad B., Banihashemi S., Kirby J.T., Baxter  
885 C.D.P., Eggeling T., Ma G. and F. Shi, Modeling of SMF tsunami hazard along the upper US East Coast:  
886 Detailed impact around Ocean City, MD, *Natural Hazards*, 76(2), 705-746, doi: 10.1007/s11069-014-  
887 1522-8 (2015)

- 888 26. Grilli S.T., D.R. Tappin, S. Carey, S.F.L. Watt, S.N. Ward, A.R. Grilli, S.L. Engwell, C. Zhang, J.T. Kirby,  
889 L. Schambach and M. Muin, Modelling of the tsunami from the December 22, 2018 lateral collapse of Anak  
890 Krakatau volcano in the Sunda Straits, Indonesia, *Scientific Reports*, 9, 11946, doi:10.1038/s41598-019-  
891 48327-6 (2019)
- 892 27. Grilli, S.T., Shelby, M., Kimmoun, O., Dupont, G., Nicolsky, D., Ma, G., Kirby, J. and F. Shi, Modeling  
893 coastal tsunami hazard from submarine mass failures: effect of slide rheology, experimental validation,  
894 and case studies off the US East coast, *Natural Hazards*, 86(1), 353-391, doi:10.1007/s11069-016-2692-3  
895 (2017)
- 896 28. Harbitz, C.B., Glimsdal S., Bazin S., Zamora N., Løvholt F., Bungum H., Smebye H., Gauer P., and Kjek-  
897 stad O., Tsunami hazard in the Caribbean: Regional exposure derived from credible worst case scenarios,  
898 *Continental Shelf Res.*, 8, 1-23, doi:10.1016/j.csr.2012.02.006 (2012)
- 899 29. Horrillo J., Grilli S.T., Nicolsky D., Roeber V., and J. Zhang, Performance bench-  
900 marking tsunami models for NTHMP's inundation mapping activities, *Pure and Applied Geophysics*, 172(3-4), 869-884  
901 (2015)
- 902 30. Ioualalen M., Asavanant J., Kaewbanjak N., Grilli S.T., Kirby J.T. and P. Watts, Modeling the 26th  
903 December 2004 Indian Ocean tsunami: Case study of impact in Thailand, *J. Geophys. Res.*, 112, C07024,  
904 doi:10.1029/2006JC003850 (2007)
- 905 31. Kirby J.T., Shi F., Tehranirad B., Harris J.C. and S.T. Grilli, Dispersive tsunami waves in the  
906 ocean: Model equations and sensitivity to dispersion and Coriolis effects, *Ocean Modell.*, 62, 39-55,  
907 doi:10.1016/j.ocemod.2012.11.009 (2013)
- 908 32. Knight, B., Model predictions of Gulf and Atlantic Coast tsunami impacts from a distribution of sources,  
909 *Science of Tsunami Hazard*, 24(5), 304-312 (2006)
- 910 33. Lander, J.F., Caribbean Tsunamis: an initial history, *Nat. Haz.*, 3, 1-18 (1997)
- 911 34. Lockridge, P.A., Whiteside, L.S. And J.F. Lander, Tsunamis and tsunami-like waves of the eastern United  
912 States, *Science of Tsunami Hazards*, 20(3), 120-157 (2002).
- 913 35. López-Venegas, A.M., Horrillo, J., Pampell-Manis, A., Huérfano, V., Mercado, A. Advanced tsunami  
914 numerical simulations and energy considerations by use of 3D-2D coupled models: the October 11, 1918  
915 Mona passage tsunami. *Pure Appl. Geophys.*, 172(6), 1679-1698, doi:10.1007/s00024-014-0988-3 (2015).
- 916 36. Løvholt, F., Pedersen, G. And G. Gisler, Oceanic propagation of a potential tsunami from the La Palma  
917 Island, *Journal of Geophysical Research: Oceans*, 113(C9) (2008)
- 918 37. Løvholt, F., Schulten, I., Mosher, D., Harbitz, C. And S. Krastel, Modelling the 1929 Grand  
919 Banks slump and landslide tsunami, *Geological Society, London, Special Publications*, 477(1), 315-331,  
920 <https://doi.org/10.1144/SP477.28> (2019)
- 921 38. Lynett, P., and 37 alii, Inter-Model Analysis of Tsunami-Induced Coastal Currents, *Ocean Modell.*, 114,  
922 14-32, doi:10.1016/j.ocemod.2017.04.003 (2017)
- 923 39. Madsen P.A., D.R. Fuhrman and H. A. Schaffer, On the solitary wave paradigm for tsunamis. *J.*  
924 *Geophys. Res.*, 113, C12012 (2008)
- 925 40. Mercado, A. And W. McCann, Numerical simulation of the 1918 Puerto Rico tsunami, *Natural Hazards*,  
926 18(1), 57-76 (1998)
- 927 41. Muir-Wood, R. And A. Mignan, A phenomenological reconstruction of the Mw9 November 1st 1755  
928 earthquake source, In *The 1755 Lisbon Earthquake: Revisited*, pp. 121-146, Springer, Dordrecht, (2009)
- 929 42. Nematì F., Grilli S.T., Ioualalen M., Boschetti L., Larroque L. and J. Trevisan, High-resolution coastal  
930 hazard assessment along the French Riviera from coseismic tsunamis generated in the Ligurian fault sys-  
931 tem. *Nat. Hazards*, 96(2), 553-586, doi:10.1007/s11069-018-3555-x (2019)
- 932 43. Okada, Y., Surface deformation due to shear and tensile faults in a half space, *Bull. Seismol. Soc.*  
933 *America*, 75(4), 1135-1154 (1985)

- 934 44. Omira, R., Baptista, M. A., Matias, L., Miranda, J. M., Catita, C., Carrilho, F., et al., Design of a sea-  
935 level tsunami detection network for the Gulf of Cadiz. *Natural Hazards and Earth System Sciences*, 9(4),  
936 1327-1338 (2009)
- 937 45. Schambach L., Grilli S.T., Kirby J.T. and F. Shi Landslide tsunami hazard along the upper US East  
938 Coast: effects of slide rheology, bottom friction, and frequency dispersion, *Pure Appl. Geophys.*, 176(7),  
939 3,059-3,098, doi:10.1007/s00024-018-1978-7 (2019)
- 940 46. Schambach L., Grilli S.T., Tappin D.R., Gangemi M.D., and G. Barbaro, New simulations and under-  
941 standing of the 1908 Messina tsunami for a dual seismic and deep submarine mass failure source, *Marine*  
942 *Geology*, 421, 106093, doi: 10.1016/j.margeo.2019.106093 (2020)
- 943 47. Schambach L., Grilli S.T., Tappin D.R., New high-resolution modeling of the 2018 Palu tsunami, based  
944 on supershear earthquake mechanisms and mapped coastal landslides, supports a dual source, *Frontiers in*  
945 *Earth Sciences*, 8, 627, doi:0.3389/feart.2020.598839 (2020)
- 946 48. Schambach, L., Grilli, S.T. and A.R. Grilli. Simulation of Global Tsunami Hazard along the U.S.  
947 East Coast. Research Report no. CACR-20-02. NTHMP Award, #NA18NWS4670073, National Weather  
948 Service Program Office, 93 pps., [http://personal.egr.uri.edu/grilli/EC\\_hazard\\_report\\_NTHMP\\_CACRo.pdf](http://personal.egr.uri.edu/grilli/EC_hazard_report_NTHMP_CACRo.pdf)  
949 (2020).
- 950 49. Schnyder J.S., Eberli G. P., Kirby J.T., Shi F., Tehranirad B., Mulder T., Ducassou E., Hebbeln D., and  
951 Wintersteller P., Tsunamis caused by submarine slope failures along western Great Bahama Bank. *Scientific*  
952 *Reports*, 6, 35925 (2016)
- 953 50. Shi F., Kirby J.T., Harris J.C., Geiman J.D., and S.T. Grilli, A high-order adaptive time-stepping TVD  
954 solver for Boussinesq modeling of breaking waves and coastal inundation, *Ocean Modell.*, 43-44, 36-51,  
955 doi:10.1016/j.ocemod.2011.12.004 (2012)
- 956 51. Tappin D.R., Watts P. and S.T. Grilli, The Papua New Guinea tsunami of 1998: anatomy of a catastrophic  
957 event, *Natural Hazards and Earth System Sciences*, 8, 243-266 (2008)
- 958 52. Tappin D.R., Grilli S.T., Harris J.C., Geller R.J., Masterlark T., Kirby J.T., F. Shi, G. Ma, K.K.S. Thing-  
959 baijang, and P.M. Maig (2014) Did a submarine landslide contribute to the 2011 Tohoku tsunami ? *Marine*  
960 *Geology*, 357:344-361 doi: 10.1016/j.margeo.2014.09.043
- 961 53. Tehranirad B., Shi F., Kirby, J.T., Harris J.C. and S.T. Grilli, Tsunami benchmark results for fully  
962 nonlinear Boussinesq wave model FUNWAVE-TVD, Version 1.0, Technical report, No. CACR-11-02,  
963 Center for Applied Coastal Research, University of Delaware (2011)
- 964 54. Tehranirad B., Harris J.C., Grilli A.R., Grilli S.T., Abadie S., Kirby J.T. and F. Shi, Far-field tsunami  
965 hazard in the north Atlantic basin from large scale flank collapses of the Cumbre Vieja volcano, La Palma,  
966 *Pure Appl. Geophys.*, 172(12), 3,589-3,616, doi:10.1007/s00024-015-1135-5 (2015)
- 967 55. ten Brink, U., Twichell D., Geist E., Chaytor J., Locat J., Lee H., Buczkowski B., Barkan R., Solow  
968 A., Andrews B., Parsons T., Lynett P., Lin J., and M. Sansoucy, Evaluation of tsunami sources with the  
969 potential to impact the U.S. Atlantic and Gulf coasts, USGS Administrative report to the U.S. Nuclear  
970 Regulatory Commission, 300 pp (2008)
- 971 56. ten Brink, U.S., Bakun W.H. and Flores C.H., Historical perspective on seismic hazard to Hispaniola  
972 and the northeast Caribbean region, *J. Geophys. Res. (Solid Earth)*, 106(B12) (2011)
- 973 57. ten Brink, U.S., Chaytor, J.D., Geist, E.L., Brothers, D.S. and B.D. Andrews, Assessment of tsunami  
974 hazard to the US Atlantic margin, *Marine Geology*, 353, 31-54 (2014)
- 975 58. Torres M.J., Hashemi, M.R., Hayward S., Spaulding M.L., Ginis I. and S.T. Grilli. Role of hurricane  
976 wind models in accurate simulation of storm surge and waves. *J. Waterways, Port, Coastal Engng.*, 145(1),  
977 04018039 (2019)
- 978 59. Udias, A., Large Earthquakes and Tsunamis at Saint Vincent Cape before the Lisbon 1755 Earthquake:  
979 A Historical Review. *Pure and Applied Geophysics*, 177, 1739-1745 (2020)

- 
- 980 60. Watts P., Grilli S.T., Kirby J.T., Fryer G.J. and D.R. Tappin, Landslide tsunami case studies using a  
981 Boussinesq model and a fully nonlinear tsunami generation model, *Natural Hazards and Earth System*  
982 *Sciences*, 3, 391-402 (2003)
- 983 61. Wei G., Kirby J.T., Grilli S.T. and R. Subramanya, A fully nonlinear Boussinesq model for free surface  
984 waves. Part I: Highly nonlinear unsteady waves, *Journal of Fluid Mechanics*, 294, 71-92 (1995)
- 985 62. Zahibo, N. and Pelinovsky, E. N., Evaluation of tsunami risk in the Lesser Antilles, *Nat. Hazards Earth*  
986 *Syst. Sci.*, 1, 221-231, doi:10.5194/nhess-1-221-2001 (2001)

# Figures

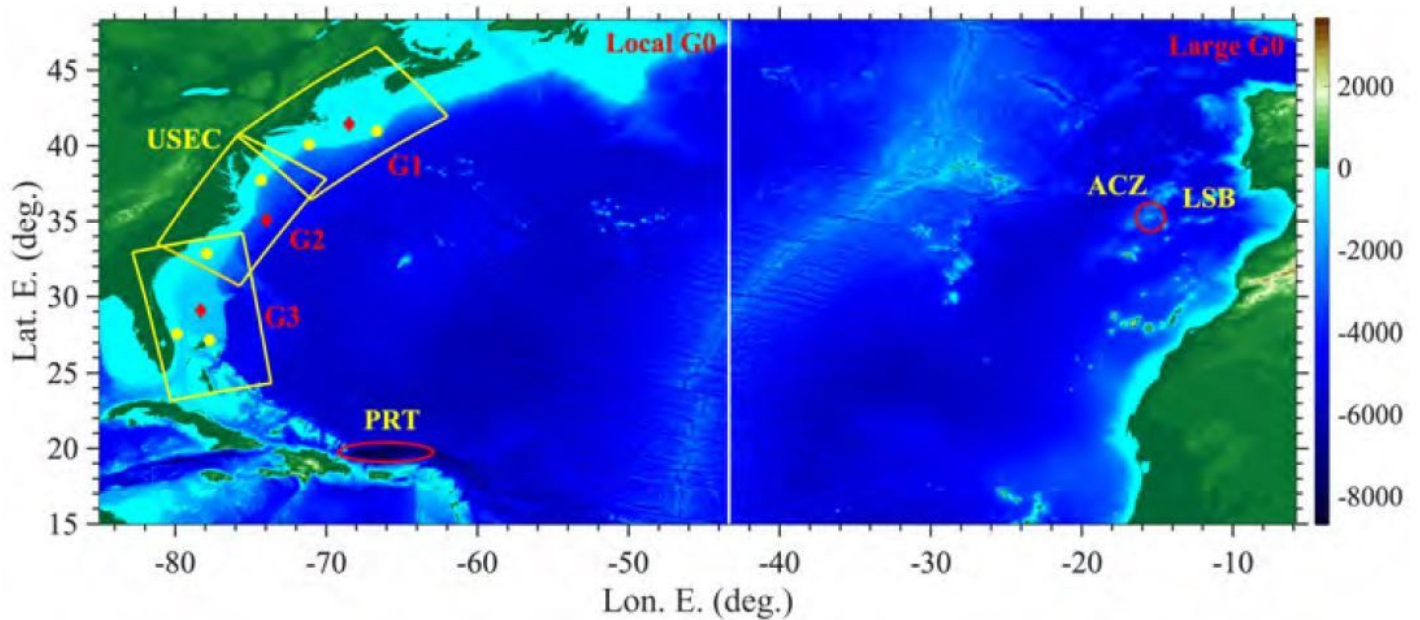


**Figure 1**

Footprint and ETOPO1 bathymetry/topography (color scale in meter shows  $\langle \rangle$  0) of FUNWAVE's 1 arc-min resolution grids in North Atlantic Ocean basin (Local/Large G0), with footprints of 3 regional 450 m nested shore-parallel Cartesian grids (G1, G2, G3; Table 4). Location are marked for the two areas of historical/hypothetical tsunami coseismic sources (red oval) considered, near the Ac,ores Convergence Zone (ACZ), including Lisbon 1755 (LSB), and near and around the Puerto Rico Trench (PRT). The Madeira Torre Rise (MTR) is the shallower ridge located on the north of the ACZ circled area and the Horseshoe Plain is to the East of the ACZ and MTR. Yellow/red symbols within the regional grids mark locations of numerical wave gauge stations where time series of surface elevation are calculated in simulations for validating the one-way grid coupling (Table 2). Note: The designations employed and the presentation of the material on this map do not imply the expression of any opinion whatsoever on the part of Research Square concerning the legal status of any country, territory, city or area or of its authorities, or concerning the delimitation of its frontiers or boundaries. This map has been provided by the authors.

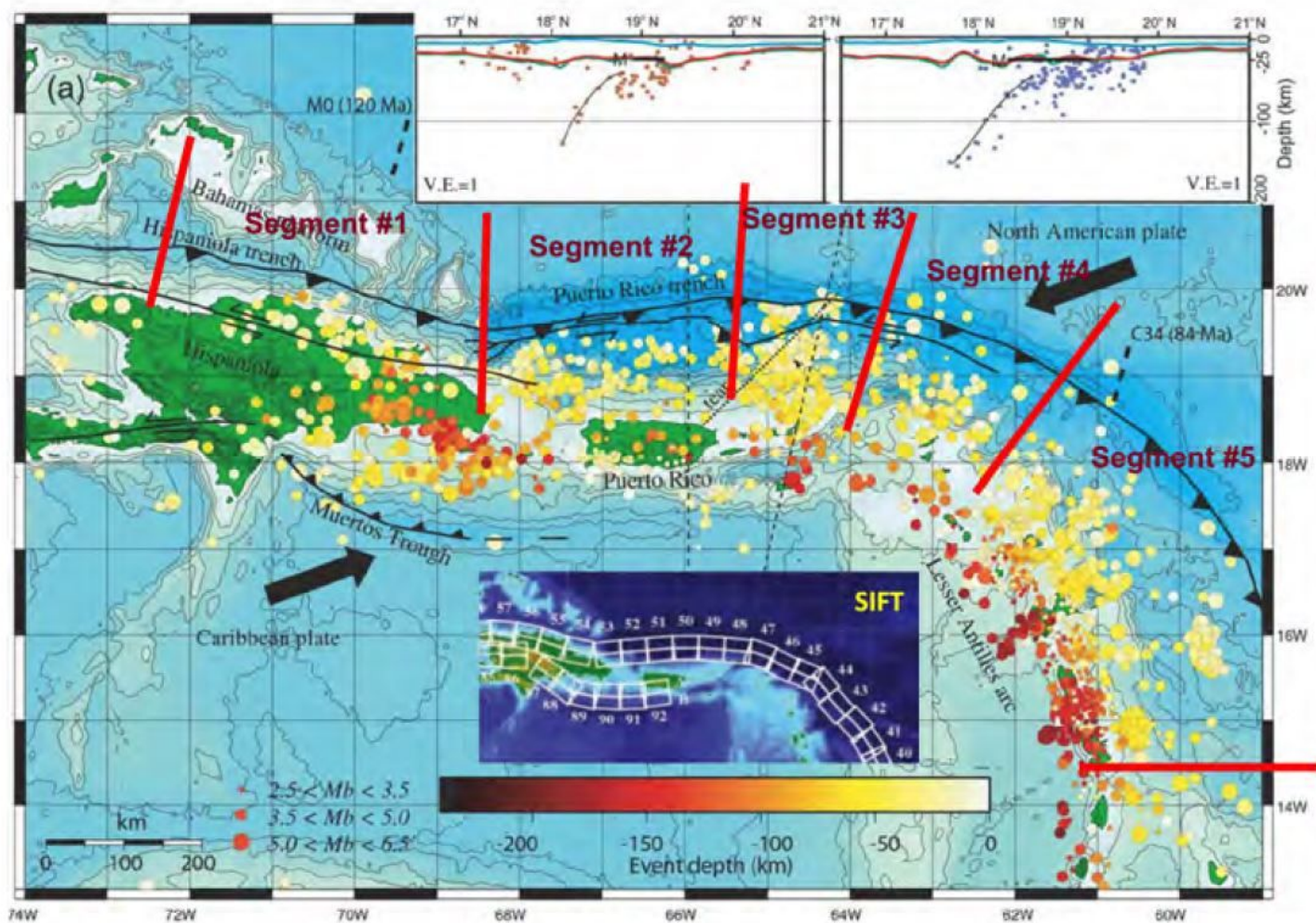


**Figure 2**

Likeliest segmentation in 5 segments of the PRT/Caribbean arc, from west of Hispaniola to Guadeloupe in the eastern part, established at the May 2019 workshop of experts at the USGS Powell Center (see Fig. 1 for location). Insert shows footprints of SIFT subfaults [17] in the considered area (see Table 2 for parameter values). Large black arrows show the nearly E-W relative plate motion of the North America Plate subducting under the Caribbean Plate. Note: The designations employed and the presentation of the material on this map do not imply the expression of any opinion whatsoever on the part of Research Square concerning the legal status of any country, territory, city or area or of its authorities, or concerning the delimitation of its frontiers or boundaries. This map has been provided by the authors.

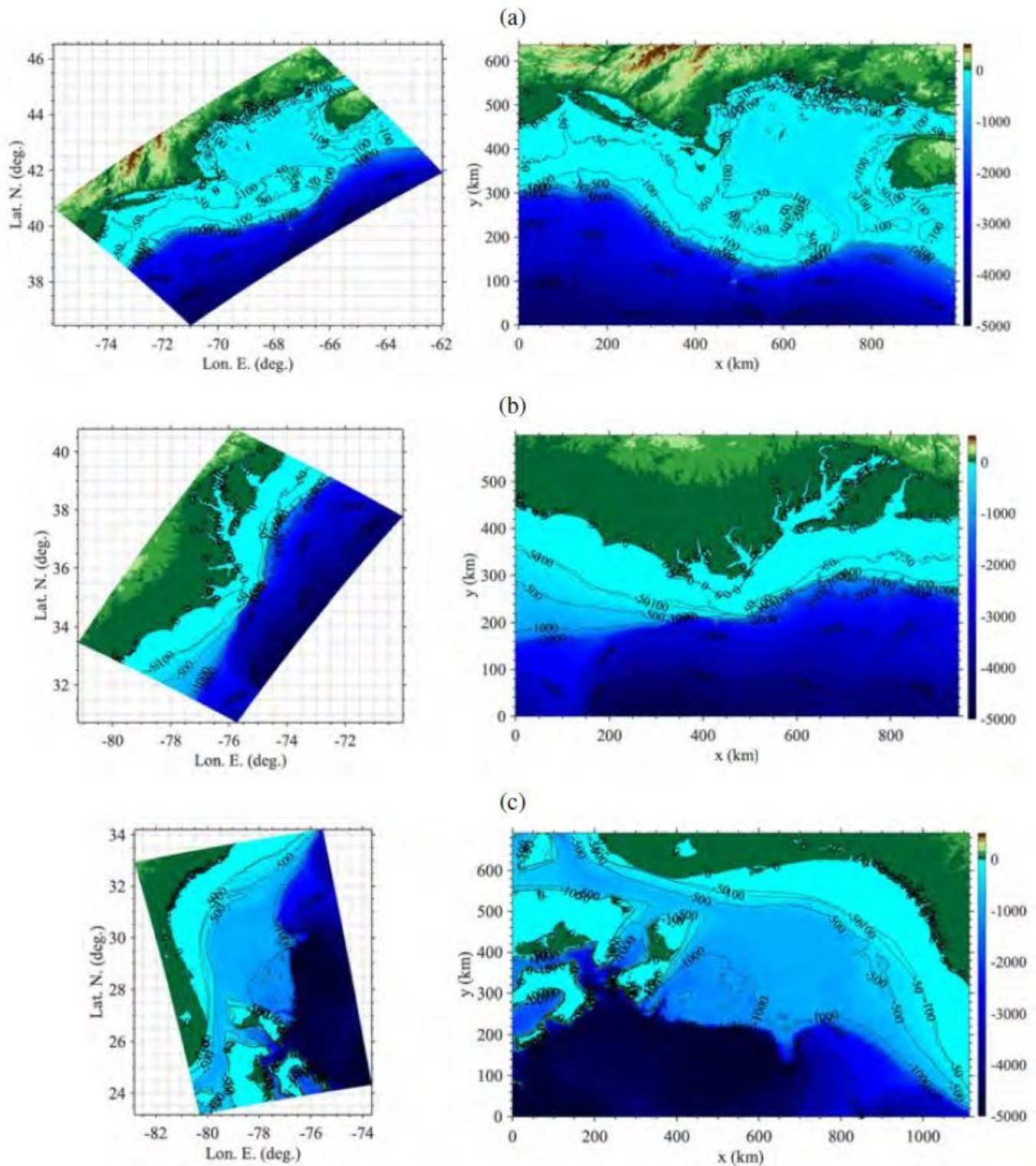


**Figure 3**

Footprints of 450 m resolution grids used in FUNWAVE, in spherical (left) and Cartesian (right) coordinates (Table 4, Fig. 1): (a) G1, (b) G2, (c) G3; color scales and contours are bathymetry/topography in meter. Note: The designations employed and the presentation of the material on this map do not imply the expression of any opinion whatsoever on the part of Research Square concerning the legal status of

any country, territory, city or area or of its authorities, or concerning the delimitation of its frontiers or boundaries. This map has been provided by the authors.

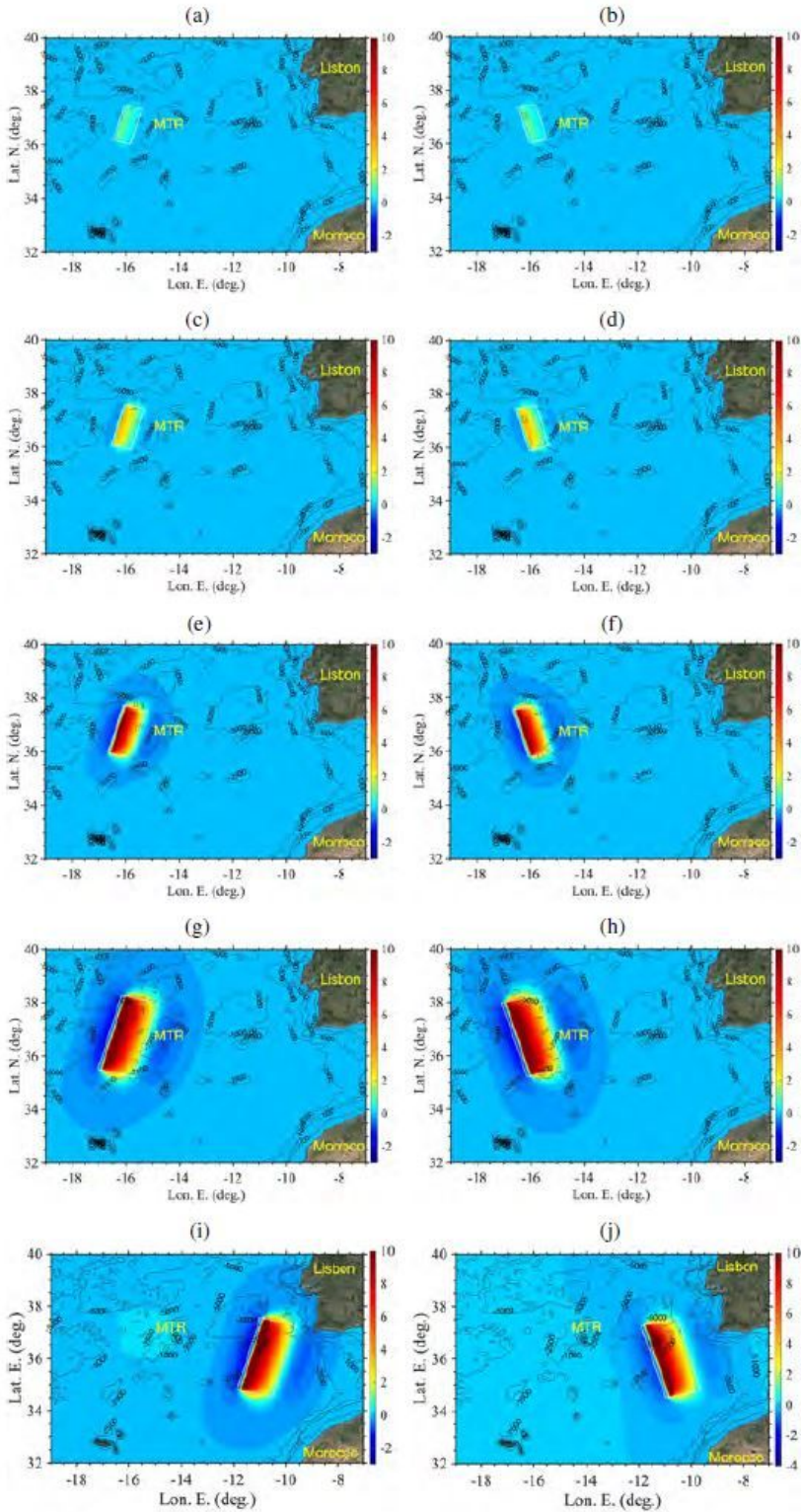


**Figure 4**

Initial surface elevations computed with Okada's [43] method (color scale in meter) for coseismic tsunami sources in the ACZ/LSB area (Fig. 1; Table 1) : (a) M8.0-MTR1; (b) M8.0-MTR2; (c) M8.3-MTR1; (d) M8.3-MTR2; (e) M8.7-MTR1; (f) M8.7-MTR2; (g) M9.0-MTR1; (h) M9.0-MTR2; (i) M9.0-HSP1; (j) M9.0-HSP2.

Each source has a single fault plane with footprint marked by white solid lines. Note, the M9.0 sources represent Lisbon 1755 proxies, located in either the ACZ, west of the MTR ("MTR"), or Horseshoe Plain ("HSP") areas (Fig. 1.)

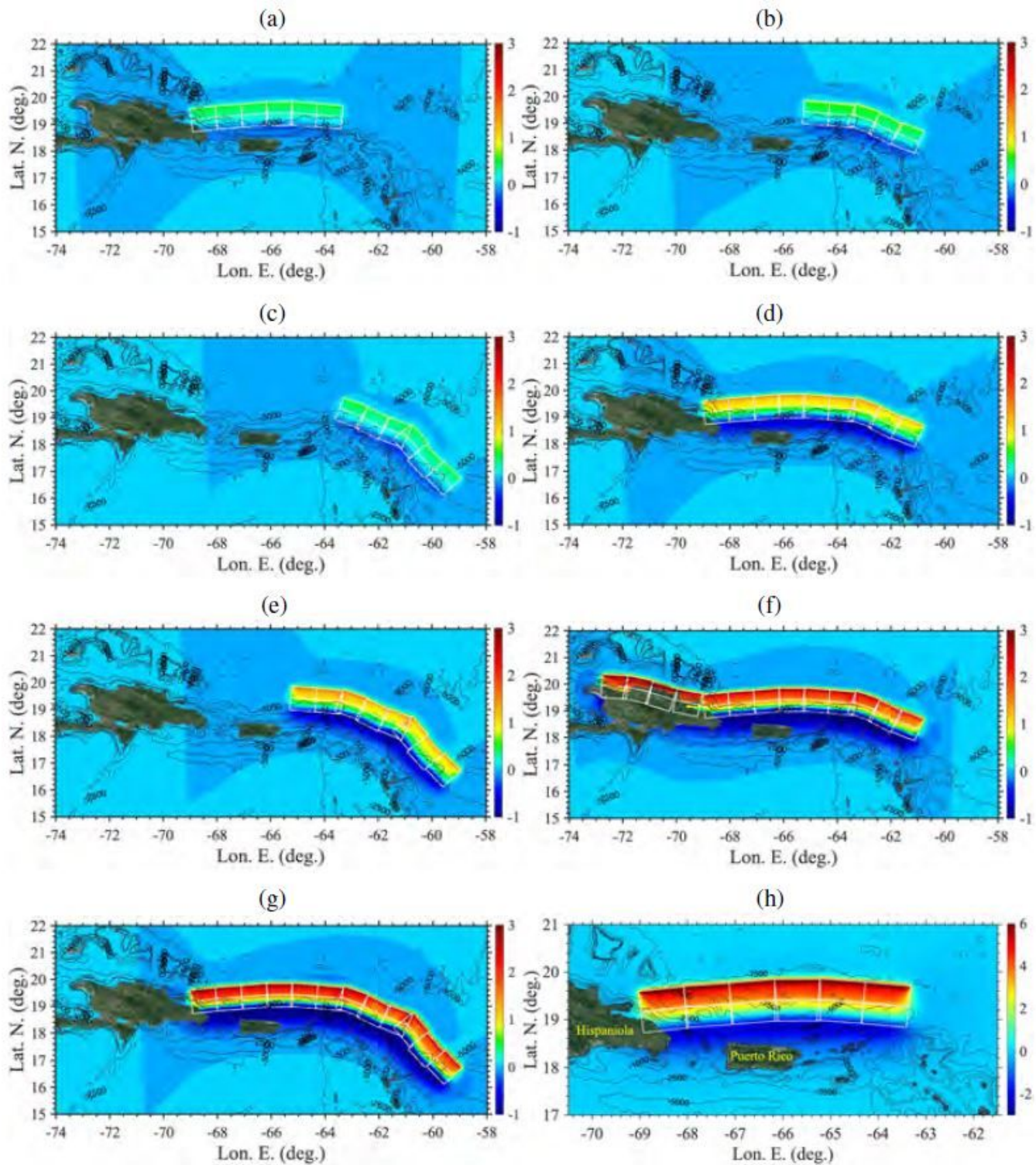


**Figure 5**

Initial surface elevations computed with Okada's [43] method for the modeled PRT/Caribbean arc tsunami sources (Fig. 1; Table 3): (a) M8.3-PRT1; (b) M8.3-PRT2; (c) M8.3-PRT3; (d) M8.7-PRT1; (e) M8.7-

PRT2; (f) M9.0-PRT1; (g) M9.0-PRT2; and (h) M9.0-PRT3. All source parameters are given Tables 2 and 3. Color scale (in meter), with same scale is used in plots (b-h), for comparison. Note: The designations employed and the presentation of the material on this map do not imply the expression of any opinion whatsoever on the part of Research Square concerning the legal status of any country, territory, city or area or of its authorities, or concerning the delimitation of its frontiers or boundaries. This map has been provided by the authors.

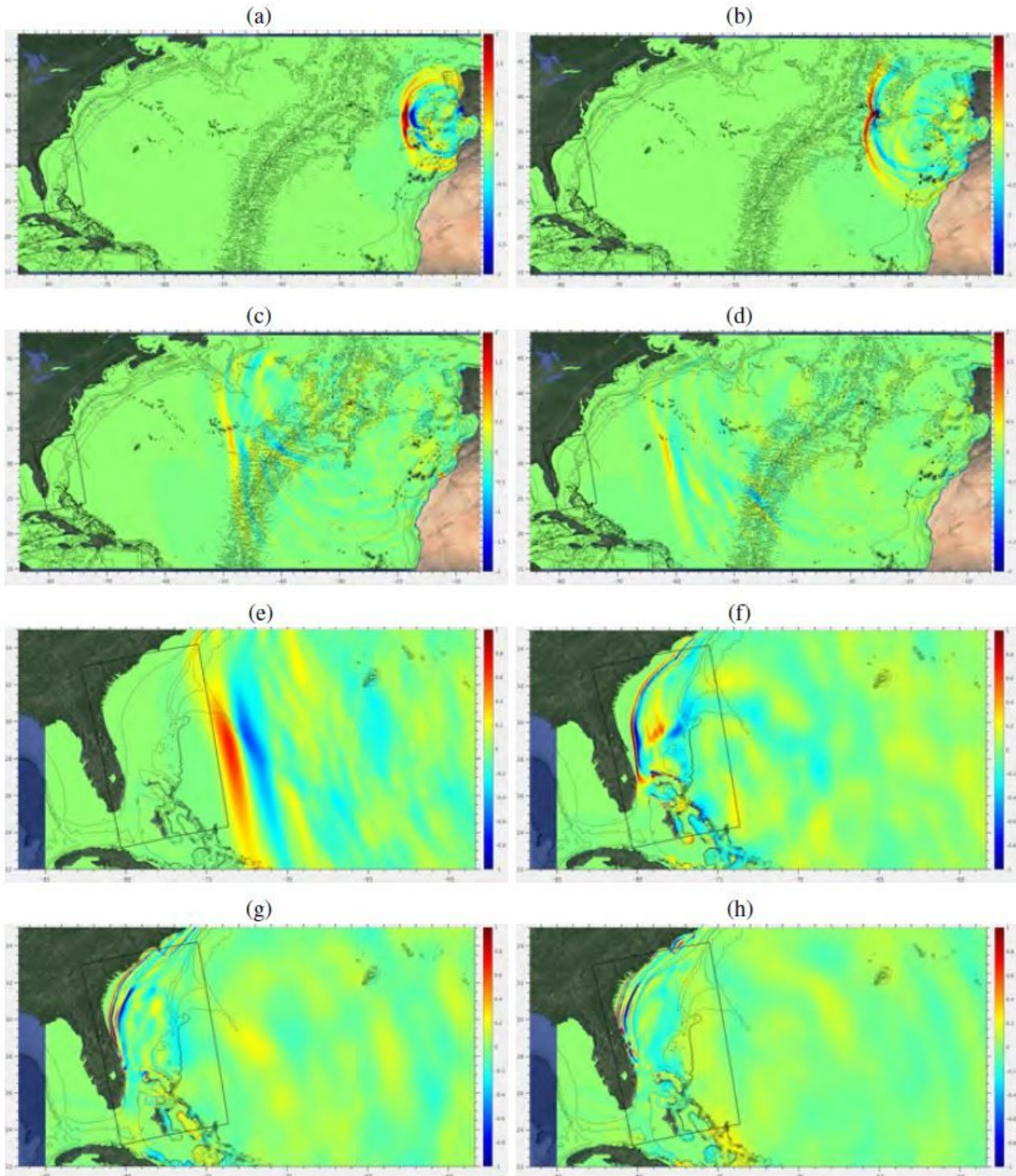


Figure 6

Snapshots of surface elevations (color scale in meter) computed for the Lisbon 1755 proxy source M9-HSP1 (Fig. 4i; Table 1), at  $t =$  (a) 1, (b) 2, (c) 5, (d) 6.5, (e) 8, (f) 9.5, (g) 10.5, and (h) 11 h. Some isobaths are plotted for reference, but without labels to simplify the figures. Higher resolutions results are used wherever available. Note: The designations employed and the presentation of the material on this map do not imply the expression of any opinion whatsoever on the part of Research Square concerning the legal status of any country, territory, city or area or of its authorities, or concerning the delimitation of its frontiers or boundaries. This map has been provided by the authors.

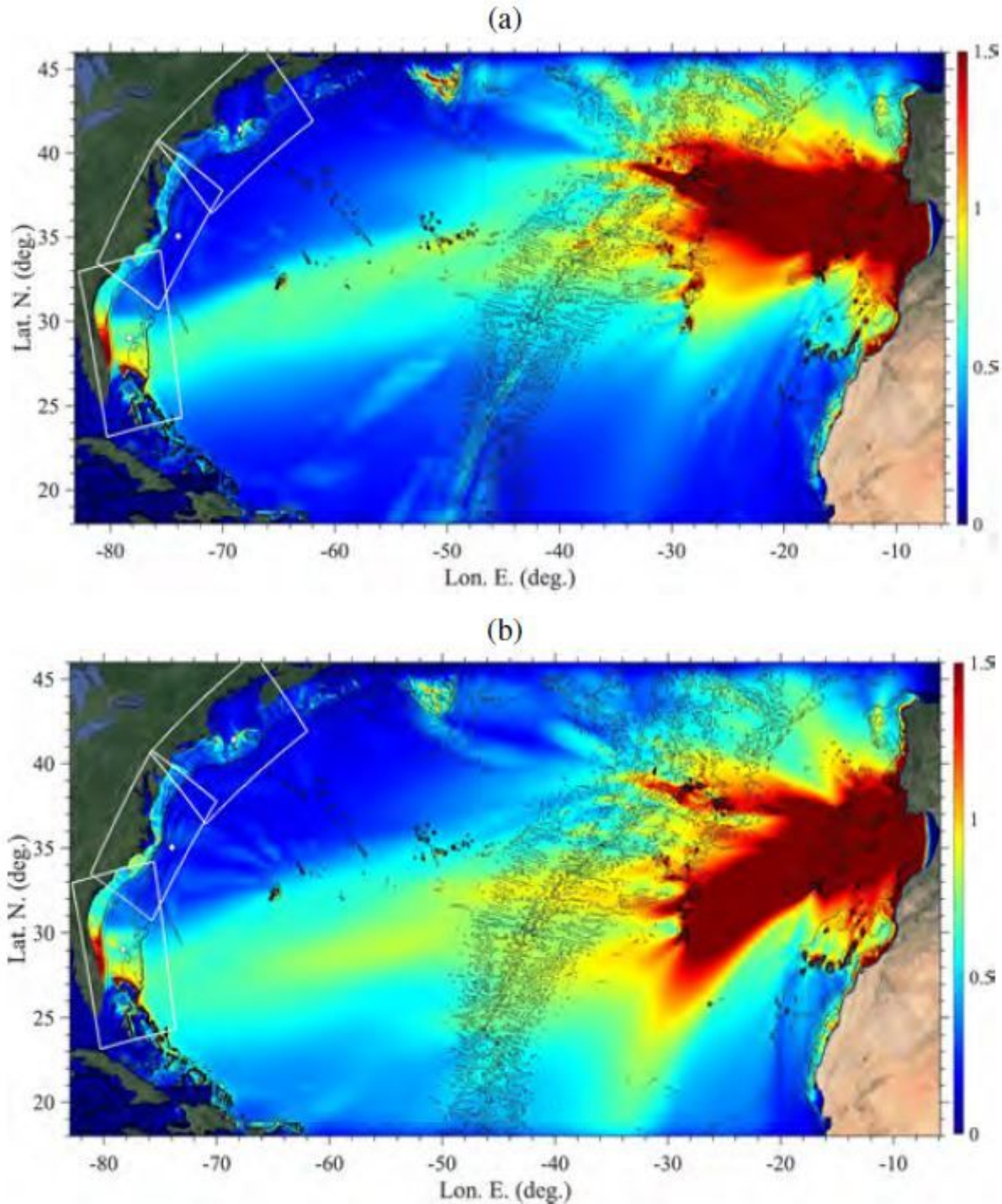


Figure 7

Envelope of maximum surface elevation computed with FUNWAVE during 24h of simulations in grid Large G0 (Table 4; Fig. 1) for the: (a) M9-HSP1, and (b) M9-HSP2, historical Lisbon 1755 coseismic sources (with parameters listed in Table 1 and initial surface elevations in Figs. 4i,j). Color scales are surface elevation in meter.

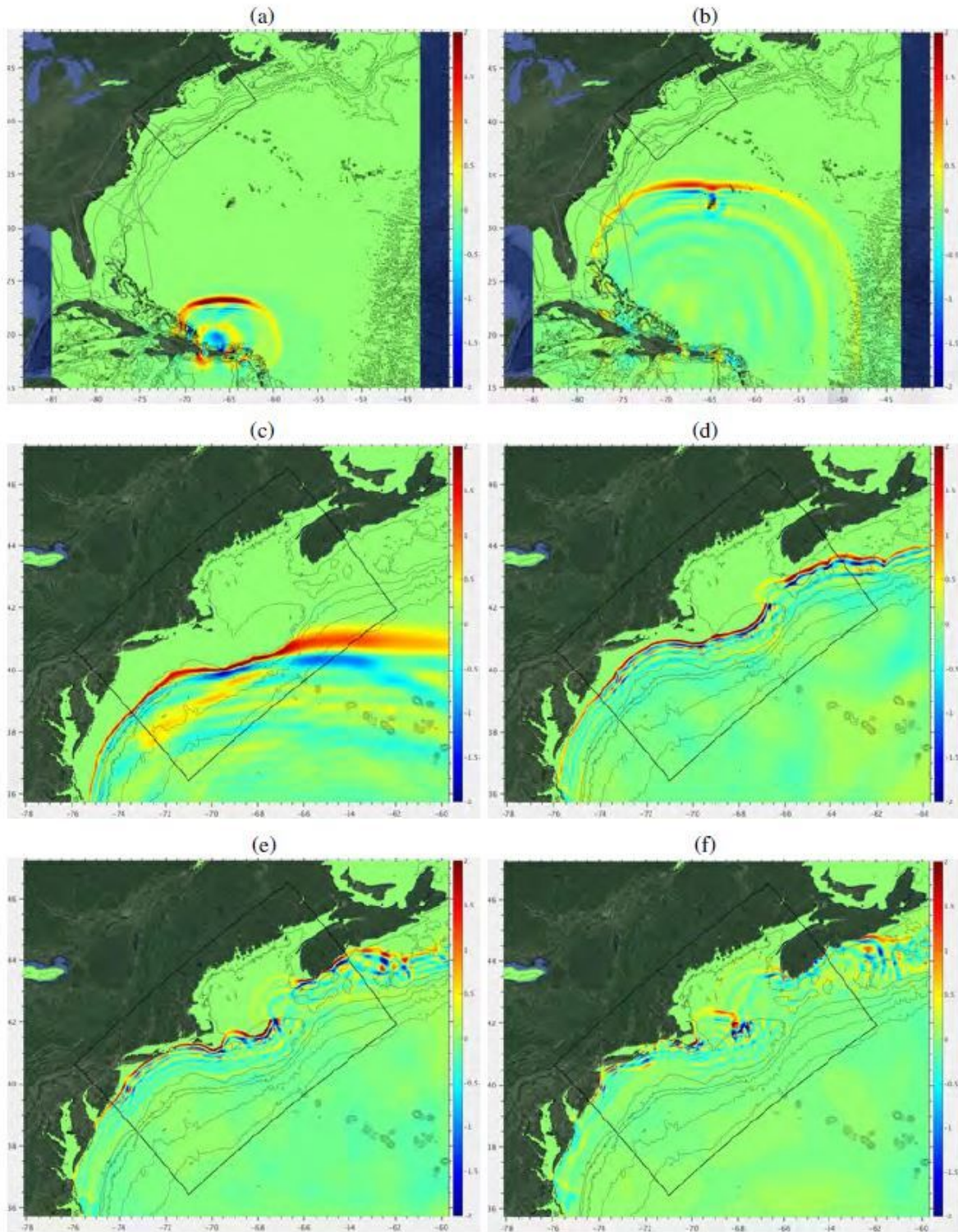
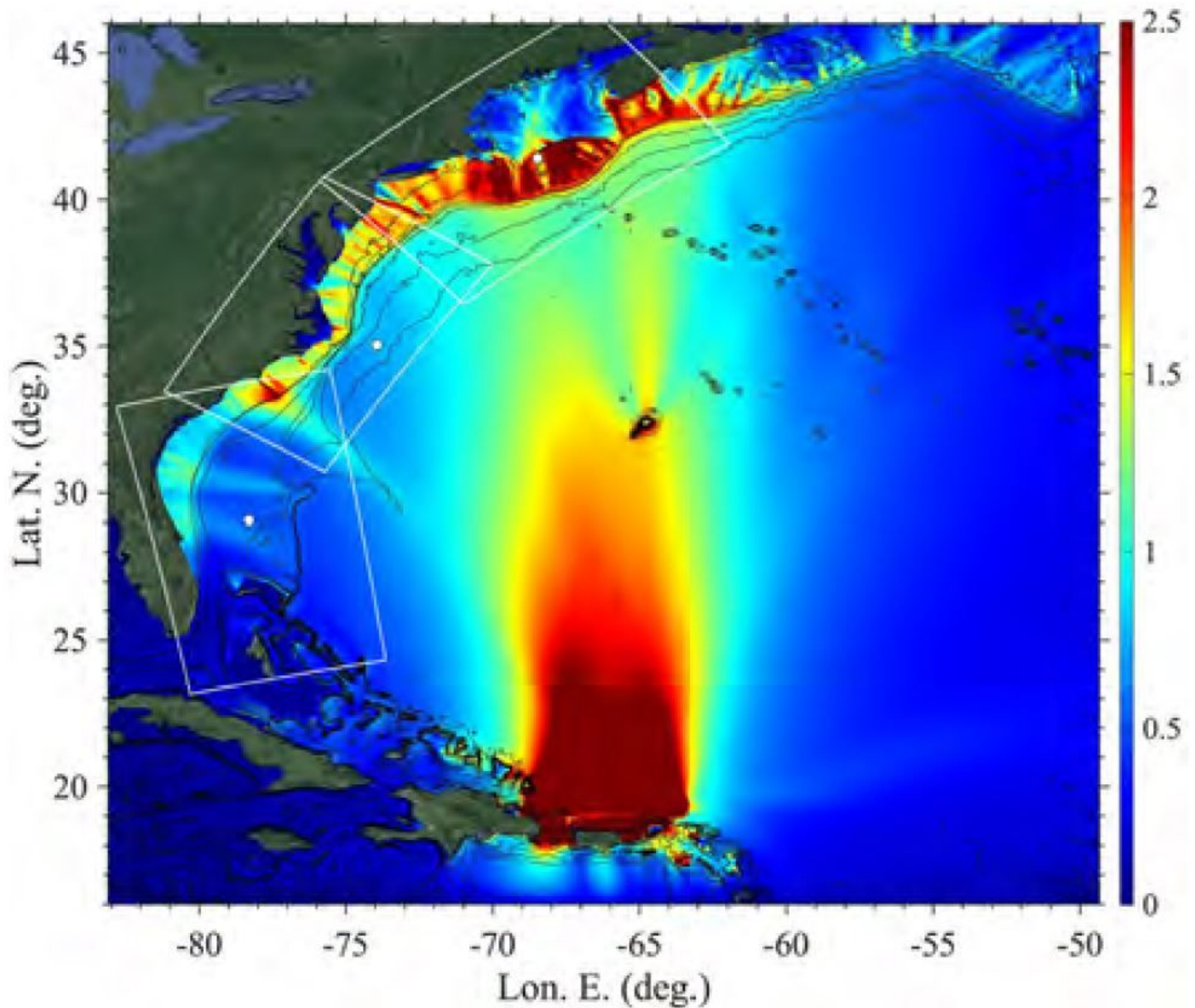


Figure 8

Snapshots of surface elevations (color scale in meter) for the PRT/Caribbean arc source M9-PRT3 (Table 3; Fig. 5h), at  $t =$  (a) 0.5, (b) 2, (c) 3, (d) 4, (e) 4.5, and (f) 5 h. Some isobaths are plotted for reference, but without labels to simplify the figures. Higher resolutions results are used wherever available. Note: The designations employed and the presentation of the material on this map do not imply the expression of any opinion whatsoever on the part of Research Square concerning the legal status of any country, territory, city or area or of its authorities, or concerning the delimitation of its frontiers or boundaries. This map has been provided by the authors.



**Figure 9**

Envelope of maximum surface elevation computed with FUNWAVE during 24h of simulations in grid Local G0 (Table 4; Fig. 1) for the M9-PRT3 coseismic source (with parameters listed in Table 3 and initial surface elevations in Figs. 5h). Color scales are surface elevation in meter. Note: The designations employed and the presentation of the material on this map do not imply the expression of any opinion whatsoever on the part of Research Square concerning the legal status of any country, territory, city or

area or of its authorities, or concerning the delimitation of its frontiers or boundaries. This map has been provided by the authors.

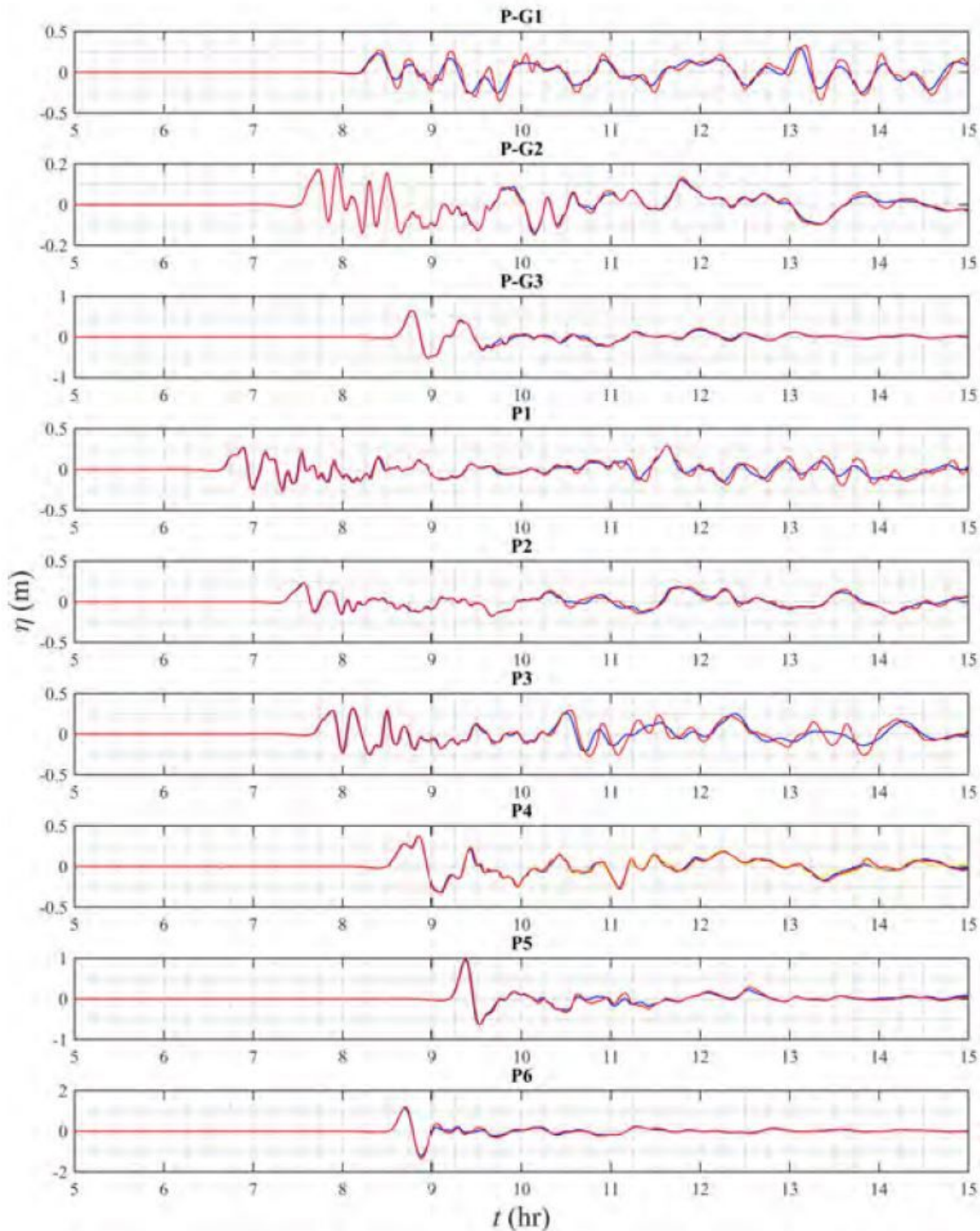


**Figure 10**

Time series of surface elevations computed for the M9-HSP1 source (Table 1), at the 9 save points defined in Table 5 (shown in Figs. 1): (blue lines) in grid Large G0; (red lines) in nested grids G1-G3. For

point P4, yellow indicates surface elevation computed in G2, red indicates surface elevation computed in G3.

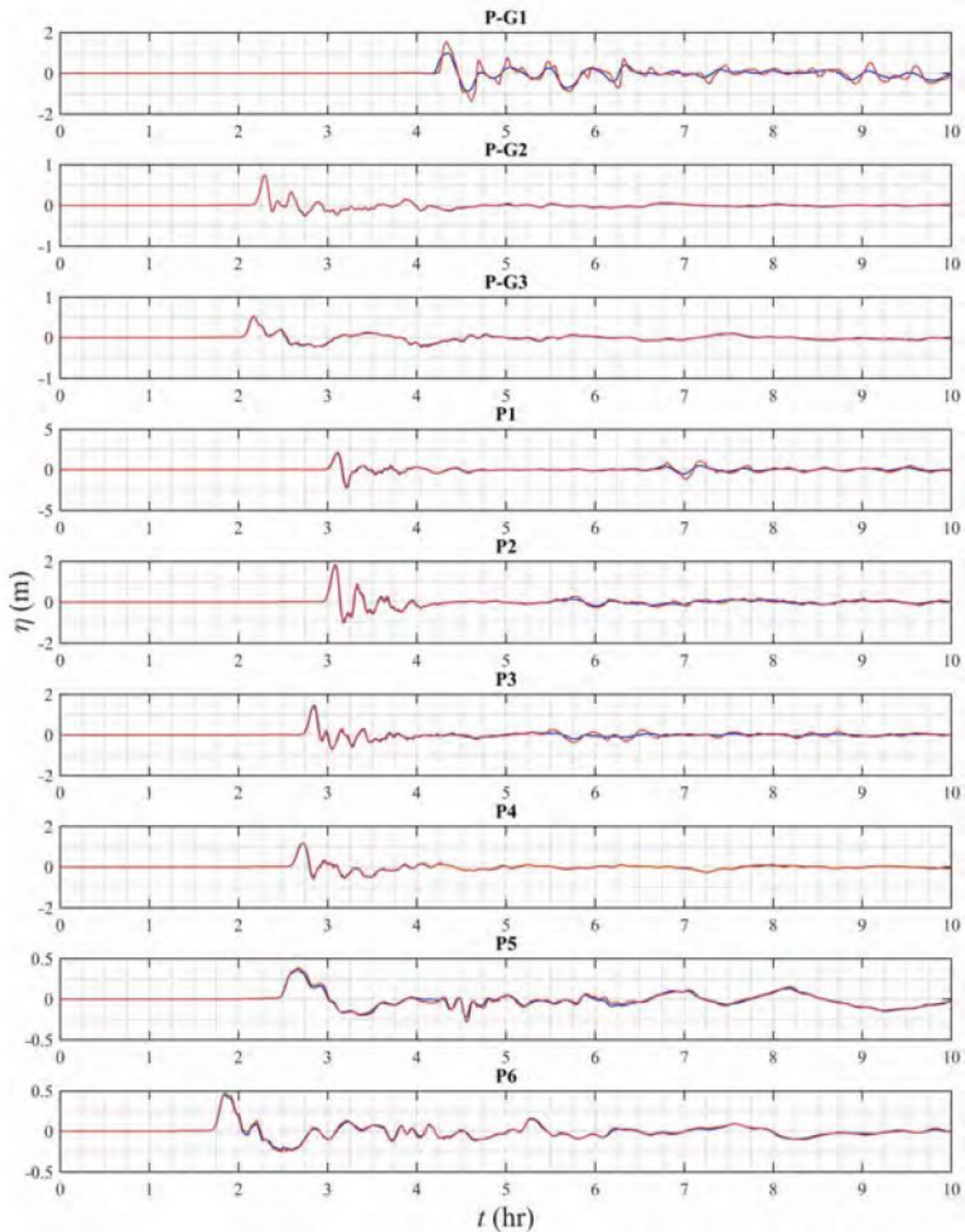


**Figure 11**

Time series of surface elevations computed for the M9-PRT3 source (Table 3), at the 9 save points defined in Table 5 (shown in Figs. 1): (blue lines) in grid Local G0; (red lines) in nested grids G1-G3. For

point P4, black indicates surface elevation computed in G2, red indicates surface elevation computed in G3.

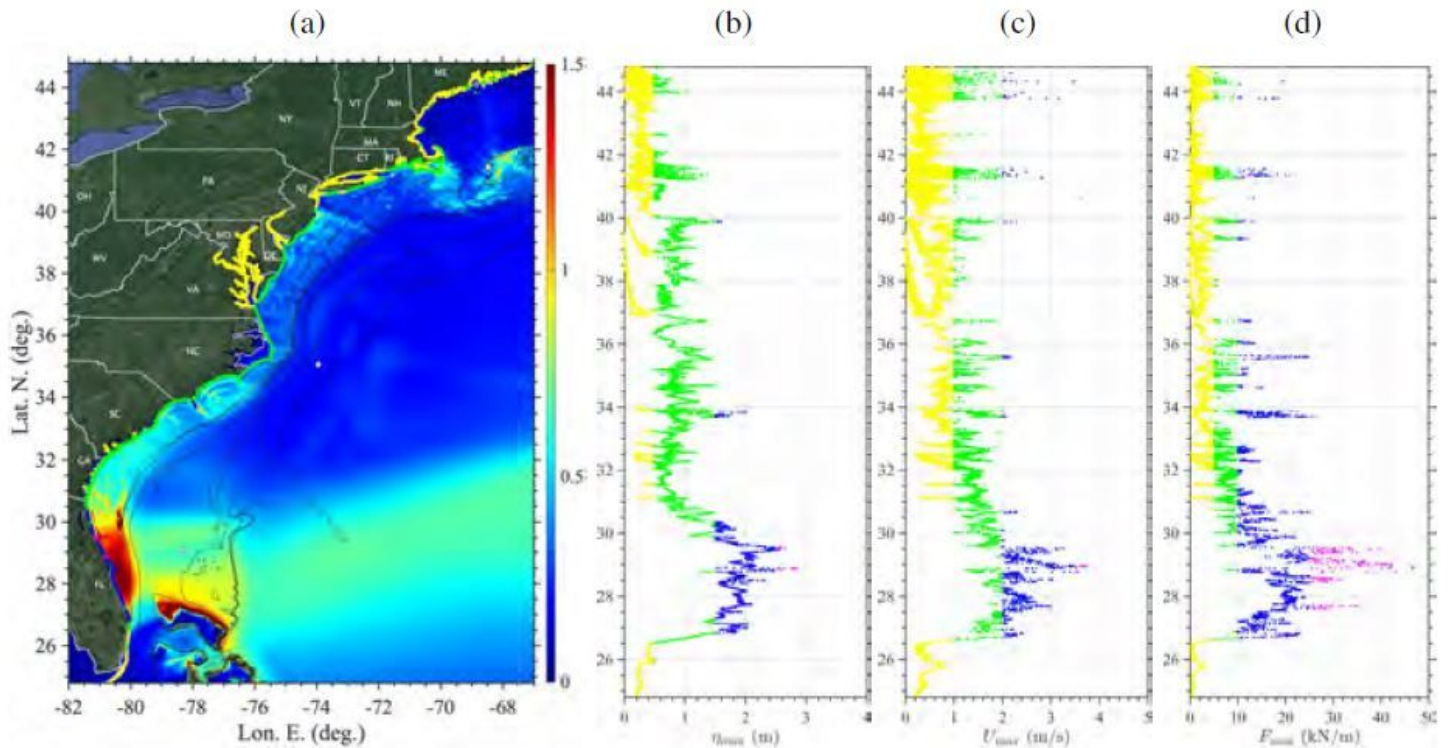


**Figure 12**

Hazard metrics along the USEC for the M9.0-HSP1 coseismic source (Table 1; Fig. 4i): (a) envelope of maximum surface elevations  $\xi_{max}$  over grids G1,G2,G3 (color scale in meter; colored dots along the coast correspond to hazard intensity  $C1_k$  from (b)); (b,c,d) color coded hazard intensity classes  $C_{ik}$  ( $k = 1; \dots; 5$ ; yellow, green, blue, magenta and red; Table 6) with corresponding values of: ( $i = 1$ )  $\xi_{max}$ , ( $i = 2$ )  $U_{max}$ , and ( $i = 3$ )  $F_{max}$ , respectively, in the same grids;  $J = 28$ ; 401 save points are defined along the 5 m isobath, here including large bays. Note: The designations employed and the presentation of the material on this map do not imply the expression of any opinion whatsoever on the part of Research Square concerning the legal status of any country, territory, city or area or of its authorities, or concerning the delimitation of its frontiers or boundaries. This map has been provided by the authors.

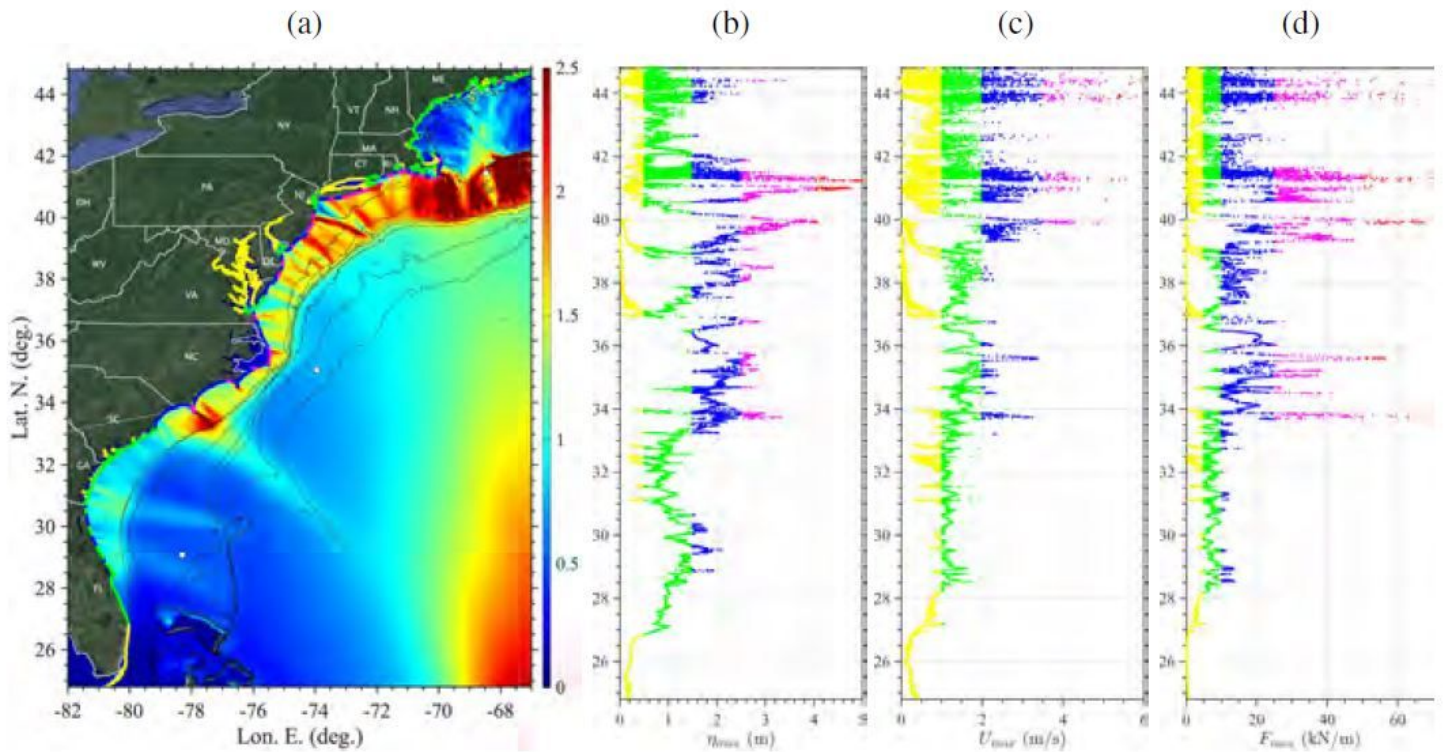


**Figure 13**

Same results as in Fig. 12, for the M9.0-PRT3 coseismic source (Table 3; Fig. 5h). Note: The designations employed and the presentation of the material on this map do not imply the expression of any opinion whatsoever on the part of Research Square concerning the legal status of any country, territory, city or area or of its authorities, or concerning the delimitation of its frontiers or boundaries. This map has been provided by the authors.

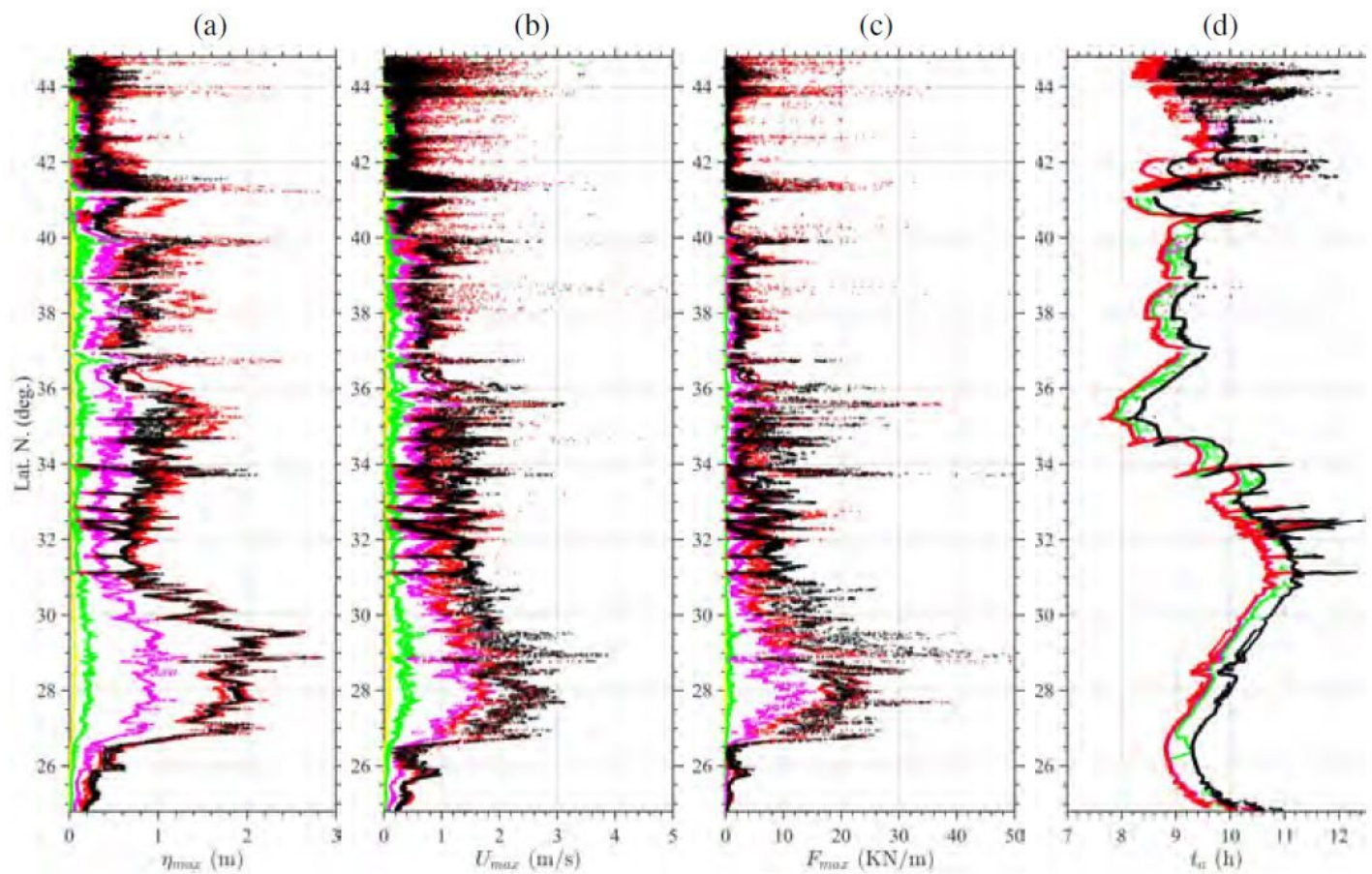


**Figure 14**

Envelope at the 5 m isobath ( $J = 18$ ; 201 save points excluding large bays) of maximum tsunami: (a) elevation; (b) current; (c) momentum force; and (d) arrival time, computed in grids G1,G2,G3, for the ten ACZ/LSB sources (Table 1; Fig. 4): (green) M8.0-MTR1, M8.0-MTR2; (yellow) M8.3-MTR1, M8.3-MTR2; (magenta) M8.7-MTR1, M8.7-MTR2; (red) M9.0-MTR1, M9.0-MTR2; and (black) M9.0-HSP1, M9.0-HSP2. Note, arrival times for the latter two sources, which are slightly longer, are not shown for clarity.

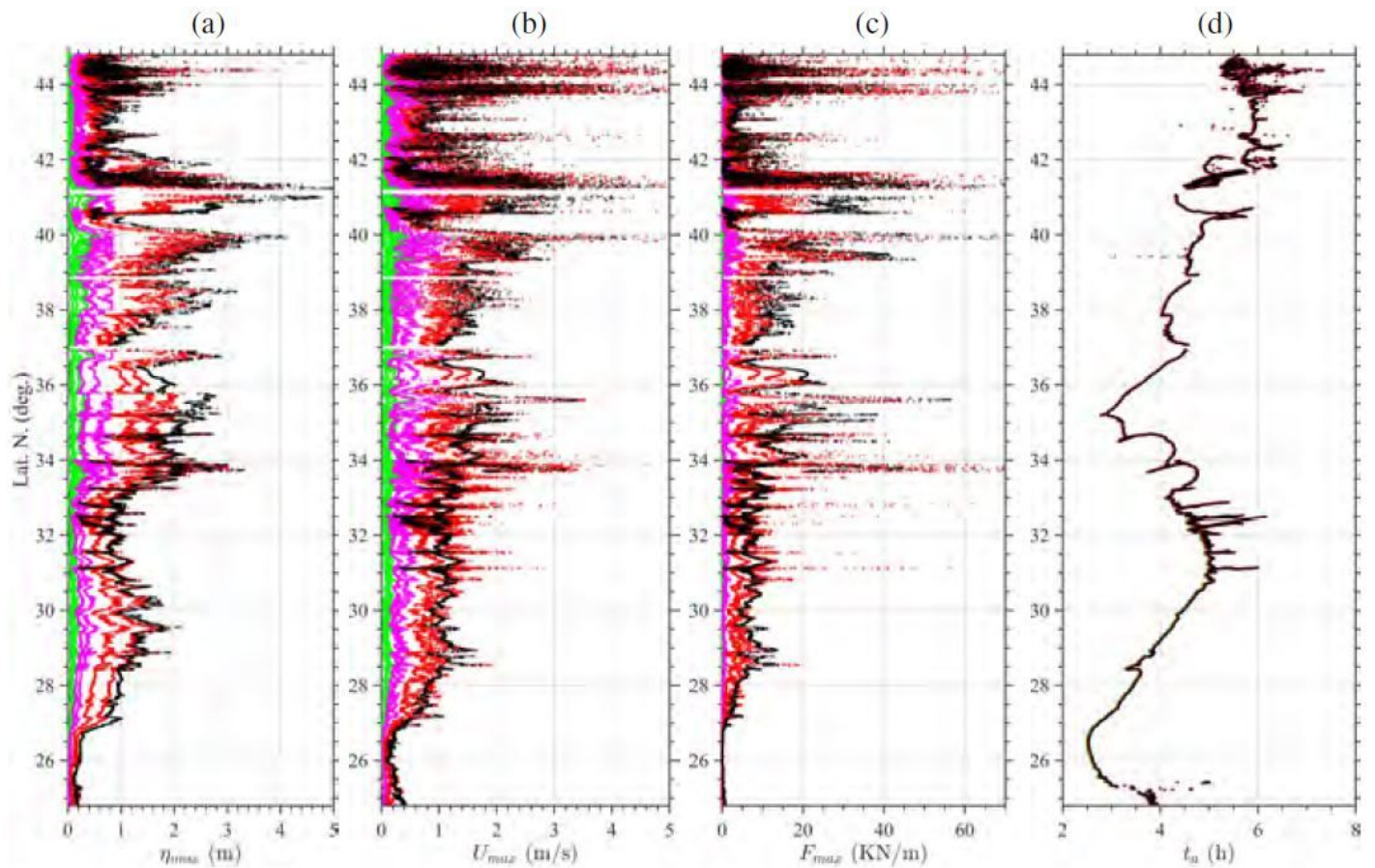


**Figure 15**

Envelope at the 5 m isobath ( $J = 18$ ; 201 save points excluding large bays) of maximum tsunami: (a) elevation; (b) current; (c) momentum force; and (d) arrival time, computed in grids G1,G2,G3, for the eight PRT/Caribbean arc sources (Table 2.2; Fig. 5): (green) M8.3-PRT1, M8.3-PRT2, M8.3-PRT3; (magenta) M8.7-PRT1, M8.7-PRT2; (red) M9.0-PRT2, M9.0-PRT2; and (black) M9.0-PRT3. Note, arrival times for the latter source, which is similar, is not shown for clarity.

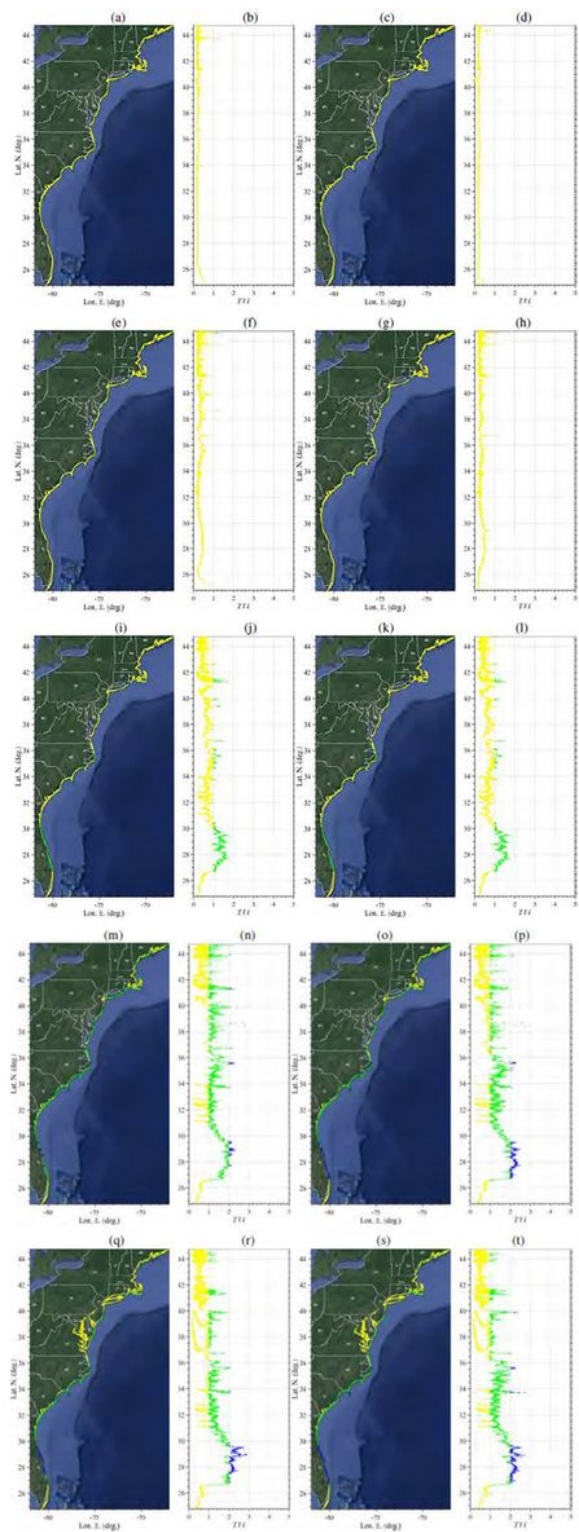


**Figure 16**

Tsunami intensity index computed for ten LSB/ACZ sources (Table 1; Fig. 4), based on results of the 4 hazard metrics in Fig. 14: (a,b) M8.0-MTR1; (c,d) M8.0-MTR2; (e,f) M8.3-MTR1; (g,h) M8.3-MTR2; (i,j) M8.7-MTR1; (k,l) M8.7-MTR2; (m,n) M9.0-MTR1; (o,p) M9.0-MTR2; (q,r) M9.0-HSP1; (s,t) M9.0-HSP2. TII metric weights are  $w_i = [0.40, 0.30, 0.15, 0.15]$ , and color coded hazard intensity classes are: (yellow) low; (green) medium low; (blue) medium (magenta) medium high, (red) high, and (black) extreme. Note, for

the last 2 sources, the TII is also provided within the large bays. Note: The designations employed and the presentation of the material on this map do not imply the expression of any opinion whatsoever on the part of Research Square concerning the legal status of any country, territory, city or area or of its authorities, or concerning the delimitation of its frontiers or boundaries. This map has been provided by the authors.

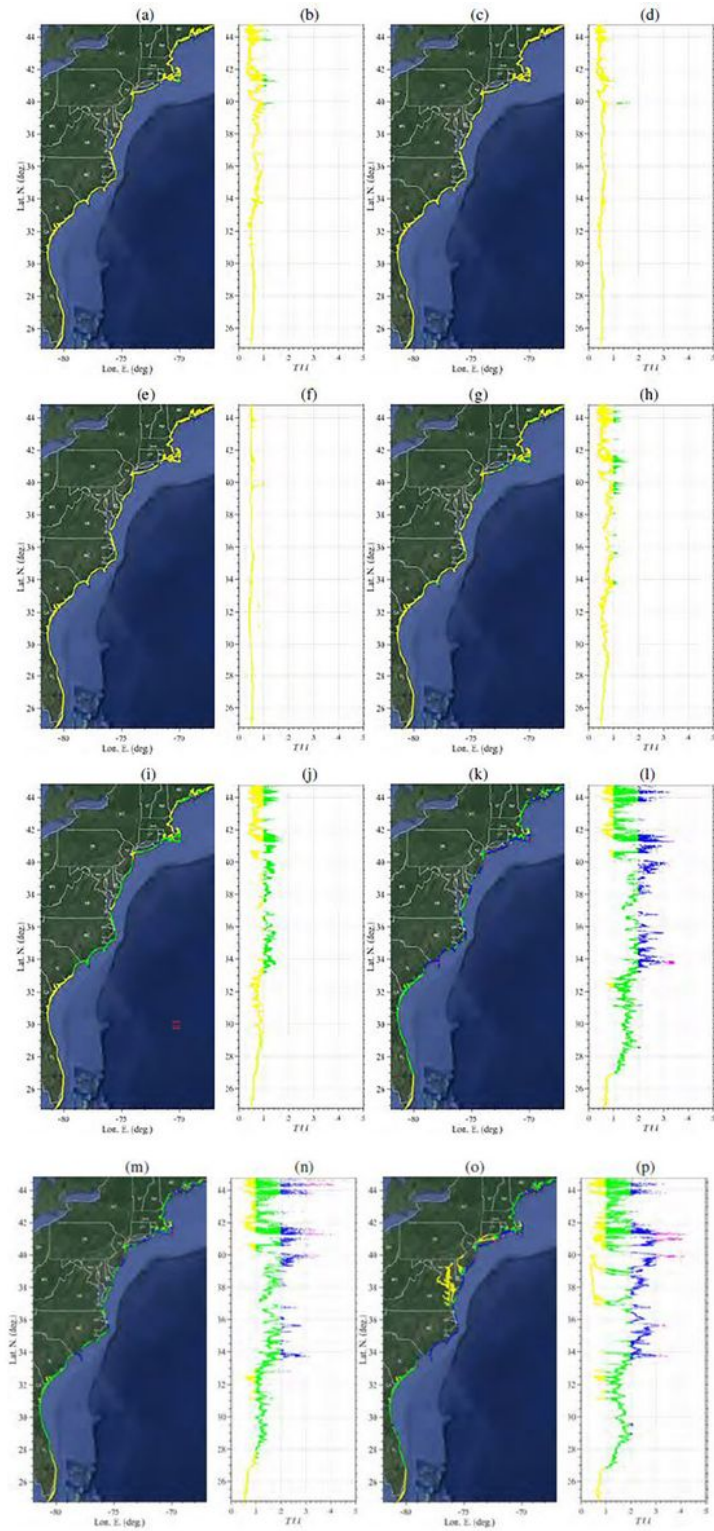


Figure 17

Tsunami intensity index computed for eight PRT/Caribbean arc sources (Table 3; Fig. 5), based on results of the 4 hazard metrics in Fig. 15: (a,b) M8.3-PRT1; (c,d) M8.3-PRT2; (e,f) M8.3-PRT3; (g,h) M8.7- PRT1; (i,j) M8.7-PRT2; (k,l) M9.0-PRT1; (m,n) M9.0-PRT2; (o,p) M9.0-PRT3. TII metric weights are  $w_i = [0.40, 0.30, 0.15, 0.15]$ , and color coded hazard intensity classes are: (yellow) low; (green) medium low; (blue) medium (magenta) medium high, (red) heigh, and (black) extreme. Note, for the last source, the TII is also provided within the large bays. Note: The designations employed and the presentation of the material on this map do not imply the expression of any opinion whatsoever on the part of Research Square concerning the legal status of any country, territory, city or area or of its authorities, or concerning the delimitation of its frontiers or boundaries. This map has been provided by the authors.

## Supplementary Files

This is a list of supplementary files associated with this preprint. Click to download.

- [HSP1.mp4](#)
- [PRT3.mp4](#)